

UNIVERSITY OF TWENTE.

Computational modelling of  
turbulence induced particle mixing  
in a stenosed channel using the  
Lattice Boltzmann method.

Cornelis Martinus Roorda

M.Sc. Thesis

15 July 2024

---

Supervisor: Dr. Kartik Jain  
Faculty of Engineering Technology  
Engineering Fluid Dynamics Group  
Document number: 451  
University of Twente  
The Netherlands

---



# Abstract

The process of radioembolization would work efficiently if the particles have mixed with the blood stream before entering the vessels that feed the tumor. Currently, the exact reasons and mechanisms of this mixing are unknown. Despite low Reynolds and Womersley numbers, the flow in hepatic artery is expected to depart from a laminar regime because of the presence of irregular diameters causing stenosis and expansion in the artery.

It is hypothesized that the non-laminar flow in the hepatic artery will cause the particles that emanate from the catheter to mix with the blood. To test this hypothesis and understand the fluid dynamics of the underlying process, an eccentric stenosis is constructed where flow has been shown to exhibit turbulent characteristics in a number of studies. An artificial catheter is then inserted in the stenosis and injected microspheres from it at various time instances of a sinusoidal cardiac cycle.

Subsequent investigations revealed that at extremely low Reynolds numbers (200), when the flow in the stenosis does not depart from laminar regime, the particles are not well mixed and are confined towards the center of the stenosis throat. Upon an increase in the stenosis Reynolds numbers (700) within physiologic ranges, as soon as the post stenotic jet breaks down to impart vorticity, the injected particles start mixing with the flow in the lumen. The location of mixing coincides with the location of the jet breakdown, and the particles mix fully with the blood within two diameters of downstream of the jet breakdown location. A subsequent relaminarization of the flow does not affect the particle mixing as the extent of turbulent activity appears sufficient to well mix the particles with the blood.

**Keywords:** Lattice Boltzmann Method; Computational Fluid Dynamics; Musubi; Right Hepatic Artery; Radioembolization; Stenosis; Onset of Turbulence; Microsphere Injection; Mixing behaviour; Particle Distribution

# Acknowledgements

When I started this assignment last year, I had little experience with computational modelling and the world of biophysical fluid dynamics. And even though both fields are so extensive, and still possess so many unknowns to me, I feel like I've learned a lot in the past months. This has not been a solo-journey and fortunately I received support from a lot of people.

First of all, I want to thank my daily supervisor dr. Kartik Jain for his advice, patience and guidance throughout this work. From the start, your broad knowledge about fluid mechanics, as well as the more specific topics helped me a lot to outline the thesis. I really enjoyed our meetings in which there was room to discuss thesis related and unrelated matters. You have the ability to calmly and quickly explain the essence of a problem or issue in simple language, something I admire. But first and foremost, your friendly attitude has kept me encouraged to bring this work to a good end.

I also want to thank Tristan Vlogman for assisting me with Musubi, the particle code and the workflow on Snellius. There have been numerous times that I have dropped by your office unannounced to ask you for a quick insight. But you always found time to patiently explain the issues in very clear wording. On the same note, I want to thank Jan van der Hoek for introducing me to the physical aspects of radioembolization.

Lastly, I want to thank my family for being there for me. My parents with their positive words and unconditional support through my entire academic career. And my two little brothers for the unconditional distractions, both voluntarily and involuntarily. I also want to thank my friends for their interest and support throughout this period. I really enjoyed our gym sessions after a day of studying and the trips abroad amongst other things.

# Nomenclature

## Physical Parameters

|        |                     |                      |
|--------|---------------------|----------------------|
| $\mu$  | Dynamic viscosity   | $[kg/m \cdot s]$     |
| $\nu$  | Kinematic viscosity | $[m^2/s]$            |
| $\rho$ | Density             | $[kg/m^3]$           |
| $T$    | Temperature         | $[K]$                |
| $P$    | Pressure            | $[kg/m \cdot s^2]$   |
| $\tau$ | Relaxation time     | $[1/s]$              |
| $F$    | Force               | $[kg \cdot m/s^2]$   |
| $m$    | Mass                | $[kg]$               |
| $t$    | Time                | $[s]$                |
| $E$    | Energy              | $[kg \cdot m^2/s^2]$ |
| $\xi$  | Velocity            | $[m/s]$              |

## Abbreviations

|       |                                      |
|-------|--------------------------------------|
| LBM   | Lattice Boltzmann Method             |
| CFD   | Computational Fluid Dynamics         |
| SIRT  | Selective Internal Radiation Therapy |
| TARE  | Transarterial Radioembolization      |
| HCC   | Hepatocellular Carcinoma             |
| HAS   | Hepatic Artery Stenosis              |
| FEM   | Finite Element Method                |
| FVM   | Finite Volume Method                 |
| NSE   | Navier Stokes Equations              |
| MDM   | Molecular Dynamics Methods           |
| BTE   | Boltzmann Transport Equation         |
| LGA   | Lattice Gas Automata                 |
| BC(s) | Boundary Condition(s)                |

BPM Beats Per Minute  
C.o.G. Center of Gravity  
CoV Coefficient of Variation  
TKE Turbulent Kinetic Energy  
CFV Centerline Flow Velocity  
PSD Power Spectral Density

Re Reynolds number  
Wo Womersley number  
Kn Knudsen number  
Ma Mach number  
Kn Stokes number  
Sr Strouhal number

# List of Figures

|      |  |    |
|------|--|----|
| 2.1  | Supine position of the patient for treatment; A) Incision location for the catheter; B) Arterial structure; C) Location of hepatic artery [1]. . . . .   | 15 |
| 2.2  | Radiation emission for $^{90}\text{Y}$ and $^{166}\text{Ho}$ [2]. . . . .  | 16 |
| 2.3  | Liver vasculature, right hepatic artery in red [3]. . . . .  | 17 |
| 2.4  | The cardiac cycle expressed in several measures 1) Pressure; 2) Volume flow rate; 3) Electrocardiogram; 4) Sound [4]. . . . .  | 17 |
| 3.1  | Simple particle collision model in 3D. . . . .   | 22 |
| 3.2  | Maxwell-Boltzmann distribution for oxygen and hydrogen at different temperatures. . . . .  | 24 |
| 3.3  | Three common lattice types for 1D, 2D and 3D. . . . .  | 28 |
| 3.4  | D2Q9 stencil with distribution functions. . . . .  | 28 |
| 3.5  | Streaming step for D2Q9 configuration. . . . .   | 31 |
| 3.6  | Four steps of the Bounceback Boundary Condition for D2Q9 configuration. . . . .  | 32 |
| 3.7  | Dirichlet Boundary Condition for D2Q9 configuration. . . . .   | 33 |
| 3.8  | Overview continuum models as function of Knudsen number. . . . .   | 37 |
| 4.1  | APES Simulation Framework [5]. . . . .   | 38 |
| 4.2  | Octree procedure [6]. . . . .  | 39 |
| 4.3  | Range of values for $\omega$ . . . . .   | 42 |
| 5.1  | 3D images of the model; A) Full model; B) Radial view; C) Catheter closeup. . . . .  | 47 |
| 5.2  | Schematic overview of the stenosis in a lengthwise cross-section and an area cross-section. The bold line represents the axisymmetric boundaries of the vessel, the dashed straight line the vessel centerline and the dashed curved lines the eccentric case. . . . . | 47 |
| 5.3  | Progreat <sup>TM</sup> [7]. . . . .  | 48 |
| 5.4  | Centerline probes pre-stenosis at various locations. . . . .   | 49 |
| 5.5  | Comparison of cross-sections of the model regarding the mesh convergence study. . . . .  | 50 |
| 5.6  | Input pulse for the flow. . . . .  | 51 |
| 5.7  | Gaussian vs Uniform particle distribution in 3D. . . . .   | 54 |
| 5.8  | Gaussian vs Uniform particle distribution in 2D. . . . .   | 54 |
| 5.9  | Initial particle distribution. . . . .   | 55 |
| 5.10 | 2D Longitudinal cross-section plots of velocity field for class I. . . . .   | 57 |
| 5.11 | 2D Longitudinal cross-section plots of flow direction for class I at $t = 1.250 \text{ s}$  . . . . .   | 57 |
| 5.12 | 2D Longitudinal cross-section plots of vorticity for class I at $t = 1.250 \text{ s}$  . . . . .  | 57 |
| 5.13 | Flow-profile for class I at $t = 1.250 \text{ s}$  . . . . .  | 58 |
| 5.14 | 2D Longitudinal cross-section plots of velocity field for class II. . . . .  | 58 |
| 5.15 | 2D Longitudinal cross-section plots of flow direction for class II at $t = 1.250 \text{ s}$  . . . . .  | 58 |
| 5.16 | 2D Longitudinal cross-section plots of vorticity for class II at $t = 1.20 \text{ 5s}$  . . . . .   | 59 |

|      |   |    |
|------|---|----|
| 5.17 | Flow-profile for class II at $t = 1.250$ s   | 59 |
| 5.18 | 2D Longitudinal cross-section plots of velocity field for class III. . . . .  | 60 |
| 5.19 | 2D Longitudinal cross-section plots of flow direction for class III at $t = 1.250$ s   | 60 |
| 5.20 | 2D Longitudinal cross-section plots of vorticity for class III at $t = 1.250$ s    | 60 |
| 5.21 | Flow-profile for class III at $t = 1.250$ s    | 61 |
| 5.23 | I-B: Mean and Standard deviation. . . . .   | 64 |
| 5.25 | I-C: Mean and Standard deviation. . . . .   | 65 |
| 5.27 | I-D: Mean and Standard deviation. . . . .   | 66 |
| 5.28 | Flowclass II, 2D cross-sectional particle distribution. . . . .   | 67 |
| 5.29 | Flowclass II, 3D particle trajectories. . . . .   | 67 |
| 5.30 | II-C: Mean and Standard deviation. . . . .  | 68 |
| 5.31 | III-B: Simulation results. . . . .  | 69 |
| 5.32 | III-B: Sectional density. . . . .   | 70 |
| 5.33 | III-B: Snapshots in time. . . . .   | 70 |
| 5.34 | III-B: Mean and Standard deviation. . . . .   | 71 |
| 5.35 | III-C: Simulation results. . . . .  | 72 |
| 5.36 | III-C: Sectional density. . . . .   | 73 |
| 5.37 | III-C: Snapshots in time. . . . .   | 73 |
| 5.38 | III-C: Mean and Standard deviation. . . . .   | 73 |
| 5.39 | III-D: Simulation results. . . . .  | 75 |
| 5.40 | III-D: Sectional density. . . . .   | 76 |
| 5.41 | III-D: Snapshots in time. . . . .   | 76 |
| 5.42 | III-D: Mean and Standard deviation. . . . .   | 77 |
| 6.1  | III-B, normal density: Pre ( $t=1.125$ s  ) and Post ( $t=1.250$ s  ) . . . . . | 79 |
| 6.2  | III-B, high-density: Pre ( $t=1.125$ s  ) and Post ( $t=1.250$ s  ) . . . . .   | 79 |
| 6.3  | III-C, normal density: Pre ( $t=1.250$ s  ) and Post ( $t=1.375$ s  ) . . . . . | 79 |
| 6.4  | III-C, high-density: Pre ( $t=1.250$ s  ) and Post ( $t=1.375$ s  ) . . . . .   | 80 |
| 6.5  | III-D, normal density: Pre ( $t=1.375$ s  ) and Post ( $t=1.500$ s  ) . . . . . | 80 |
| 6.6  | III-D, high-density: Pre ( $t=1.375$ s  ) and Post ( $t=1.500$ s  ) . . . . .   | 80 |
| 6.7  | III-B 2D post-stenosis particle trajectory comparison. . . . .  | 81 |
| 6.8  | III-B snapshots of trajectories at similar time-steps. . . . .  | 81 |
| 6.9  | III-B Statistical comparison. . . . .   | 82 |
| 6.10 | III-C 2D post-stenosis particle trajectory comparison. . . . .  | 83 |
| 6.11 | III-C snapshots of trajectories at similar time-steps. . . . .  | 83 |
| 6.12 | III-C Statistical comparison. . . . .   | 84 |
| 6.13 | III-D 2D post-stenosis particle trajectory comparison. . . . .  | 85 |
| 6.14 | III-D snapshots of trajectories at similar time-steps. . . . .  | 85 |
| 6.15 | III-D Statistical comparison. . . . .   | 86 |
| 7.1  | III-B Centerline velocity probes at interval locations. . . . .   | 88 |
| 7.2  | III-B Combined $y$ - and $z$ -velocity deviations, initial positions of deflection marked by red dots. . . . .  | 88 |
| 7.3  | III-C Centerline velocity probes at interval locations. . . . .   | 90 |
| 7.4  | III-C Combined $y$ - and $z$ -velocity deviations, initial positions of deflection marked by red dots. . . . .  | 90 |
| 7.5  | III-D Centerline velocity probes at interval locations. . . . .   | 91 |
| 7.6  | III-D Combined $y$ - and $z$ -velocity deviations, initial positions of deflection marked by red dots. . . . .  | 91 |

|      |  |     |
|------|--|-----|
| 7.7  | II-B Centerline velocity probes at interval locations. . . . .   | 92  |
| 7.8  | Boundary layer flow on a flat plate, developing from laminar- via transitional- to turbulent flow. Parameter $\gamma$ is the intermittent factor; $\gamma = 0$ indicates the onset of spike generation, $\gamma = 1$ indicates the completion of turbulent transition [8]. . . . . | 93  |
| 7.9  | Energy spectrum $E(k)$ as a function of the Wave number $k = \frac{2\pi f}{c}$ . Note the log-log plot layout. . . . .   | 94  |
| 7.10 | PSD plots for different locations post-stenosis. . . . .   | 96  |
| 7.11 | Guide for reading the final simulation overviews. . . . .  | 97  |
| 7.12 | Combined overview average centerline distance for II-B, III-B, III-C and III-D. . . . .  | 101 |

# Contents

|   |           |
|---|-----------|
| <b>List of Figures</b>                                      | <b>7</b>  |
| <b>1 Introduction</b>                                       | <b>12</b> |
| 1.1 Problem statement . . . . .                             | 12        |
| 1.2 Goal/Objectives . . . . .                               | 12        |
| 1.3 Research question . . . . .                             | 12        |
| 1.4 Scope . . . . .   | 13        |
| 1.5 Outline . . . . .                                       | 13        |
| <b>2 Radioembolization: Procedure and State of research</b> | <b>14</b> |
| 2.1 Radioembolization . . . . .                             | 14        |
| 2.2 Arterial flow dynamics & Cardiac cycle . . . . .        | 16        |
| 2.3 Current state of research . . . . .                     | 18        |
| <b>3 Theory: Lattice Boltzmann Method</b>                   | <b>21</b> |
| 3.1 Kinetic Theory of gases . . . . .                       | 22        |
| 3.2 Maxwell-Boltzmann distribution . . . . .                | 23        |
| 3.3 Boltzmann Transport Equation . . . . .                  | 24        |
| 3.4 BGK approximation . . . . .                             | 26        |
| 3.5 Discretization . . . . .                                | 27        |
| 3.6 LBM Procedure . . . . .                                 | 30        |
| 3.7 Boundary conditions . . . . .                           | 32        |
| 3.7.1 Bounceback . . . . .                                  | 32        |
| 3.7.2 Dirichlet . . . . .                                   | 32        |
| 3.8 Chapman-Enskog expansion . . . . .                      | 34        |
| 3.9 Applications . . . . .                                  | 36        |
| <b>4 Software: APES Simulation Framework</b>                | <b>38</b> |
| 4.1 Mesh generator: Seeder . . . . .                        | 39        |
| 4.2 LBM Solver: Musubi . . . . .                            | 40        |
| 4.2.1 Particles . . . . .                                   | 43        |
| 4.3 High performance computing: Snellius . . . . .          | 44        |
| <b>5 Analysis of turbulence induced particle mixing</b>     | <b>46</b> |
| 5.1 Simulation Set-up . . . . .                             | 46        |
| 5.1.1 Geometry set-up . . . . .                             | 46        |
| 5.1.2 Mesh . . . . .  | 48        |
| 5.1.3 Flow conditions . . . . .                             | 51        |
| 5.1.4 Particles . . . . .                                   | 53        |

|  |            |
|--|------------|
| <i>CONTENTS</i>  | 11         |
| 5.2 Analysis of flow . . . . .                                     | 56         |
| 5.3 Analysis of particle mixing . . . . .                          | 62         |
| 5.3.1 Preliminary simulation analysis . . . . .                    | 63         |
| <b>6 Comparison mixing behaviour with higher density particles</b> | <b>78</b>  |
| 6.1 High-density particle simulations . . . . .                    | 78         |
| 6.1.1 Flow . . . . .   | 79         |
| 6.1.2 Particles . . . . .  | 80         |
| <b>7 Implications of turbulence induced particle mixing</b>        | <b>87</b>  |
| 7.1 Fluid mechanical analysis . . . . .                            | 87         |
| 7.2 Power Spectral Density . . . . .                               | 93         |
| 7.3 Final overview . . . . .                                       | 97         |
| <b>8 Discussion, Conclusions and Recommendations</b>               | <b>102</b> |
| 8.1 Discussion . . . . .   | 102        |
| 8.2 Conclusions . . . . .  | 105        |
| 8.3 Recommendations . . . . .                                      | 106        |
| <b>Bibliography</b>  | <b>107</b> |

# Chapter 1

## Introduction

### 1.1 Problem statement

Radioembolization is a procedure in which microspheres are injected via a catheter into the bloodstream through the right hepatic artery. These particles travel with the blood flow through the liver vasculature to the cancerous cells, driven by pulsatile flow. At this point, the flow experiences relatively low Reynolds numbers, depending on the subject and travelled distance. During this period, the flow could exhibit (transition to) turbulent behaviour, or at least possess non-laminar flow characteristics, as it enters the hepatic artery due to tortuous vessels and changes in diameters. The procedure of radioembolization works in clinical practice. However, the exact mechanisms leading to the working of the procedure remain unknown. In a scenario of radioembolization, the particles should mix well before the first bifurcation. In order to test this, it is hypothesized that the flow in the artery could become turbulent. To model and study this, flow in a stenosed pipe is investigated, where the stenosis acts as an onset for turbulence in the model.

### 1.2 Goal/Objectives

As derived from the problem statement, the main goal of this thesis is to investigate the mixing behaviour of microspheres before the first bifurcation in the right hepatic artery for a stenosed pipe flow configuration for varying Reynolds numbers. The surrounding blood flow is modelled after physical pulsating flow, and the core parameter, injection time-instant, is varied and investigated across a range of Reynolds numbers. An additional objective is to quantify the mixing performance of each simulation for comparison. The final goal is to conclusively relate the assessed turbulence to particle mixing, providing insight into the implications for radioembolization treatment procedures.

### 1.3 Research question

The goal of the research translates into the following main research question:

**How can the possibility of turbulence in the lumen of the hepatic artery explain mixing of microspheres with the blood and consequent efficacy of the procedure?**

Several sub-questions are addressed to aid in answering the main research question:

1. **Can flow leave laminar regime in the hepatic artery?** Mapping the range of flow conditions based on literature values and implementing them into the computational model provides the basis for the flow of the simulations.
2. **Does this non-laminar regime result in better mixing?**  
By the introduction of particles in the simulation, the subsequent trajectories and mixing behaviour

of the ejected particles can be determined and assessed based on statistical criteria.

### 3. **How does the injection timing influence the mixing, if at all?**

By prescribing temporal variations in flow, a model heartbeat is established. Several distinct particle release-instances are evaluated based on their final microsphere distribution.

## 1.4 Scope

All outcomes in this thesis are results of simulations of the Lattice Boltzmann solver Musubi, part of the APES package. Utilization of this approach, given its suitability for the fluid-mechanical problem at hand, is justified. Musubi has been used in previous research and its validity has been established through numerous in-vitro experiments, strengthening the confidence in its applicability. However, LBM has its limitations and is, at all times, a model to capture the essence of complex real-life flow phenomena. The inherent limitations of Musubi are elaborated upon when appropriate. Simulation results solely be applicable to the geometry of a stenosed pipe configuration, which has been extensively studied and broadly accepted as models for turbulence onset in arteries.

## 1.5 Outline

The research is structured in eight chapters, which roughly follows the standard headings of a scientific paper, namely: introduction, literature review, methodology, results, discussion and conclusion. Chapter 1 identifies the problem constructs the research questions and provides the research outline. Chapter 2 provides the necessary background information regarding the treatment procedure of radioembolization, the current state of research regarding microsphere distributions and arterial particle mixing and the connection with this research and simulations. Chapter 3 elaborates on the theory behind the Lattice Boltzmann Method. This aims to provide sufficient background knowledge about the working principles and implementation of the LB solver package APES in Chapter 4. The modelling basis to outline the simulation, accompanied by a mesh convergence study is presented in the first part of Chapter 5, where the first two sub-questions are addressed. Additionally, an overview of the initial results of the simulation cases is given. In Chapter 6 the influence of an increased particle density is investigated and compared to previous results. Chapter 7 further elaborates on the flow characteristics and aims to link the onset of turbulence to particle mixing. Here, the third sub-question is answered. The final chapter, Chapter 8, contextualizes the findings, draws conclusions, and provides recommendations for future research directions. To recapitulate, an answer to the main research question is presented as well.

## Chapter 2

# Radioembolization: Procedure and State of research

The following sections provide the necessary background information regarding the research objective. In order to better understand modelling simulations and interpret results, a basis of knowledge about radioembolization is required. Additionally a concise background of the system in terms of liver vasculature and cardiac cycle is provided. In this chapter, the connection between the treatment of radioembolization and the procedure of modelling is discussed, paired with a study highlighting the current state of research.

### 2.1 Radioembolization

Selective Internal Radiation Therapy (SIRT) or transarterial radioembolization (TARE) is a clinical procedure which is primarily used to treat liver cancer. The medical operation applies to hepatocellular carcinoma (HCC), the most common type of primary liver cancer and metastatic liver tumours, where cancerous cells have spread from the original sites. These two conditions are characterized by their inoperability and inability to be treated with chemotherapy, leaving radioembolization as a last resort option for patients. It is typically employed as a method to enhance the quality of life or extend the life of a patient rather than curing them completely. Additionally, secondary goals are to slow the progression of the spread of the disease and to control and alleviate symptoms. Due to the complex nature and the patient-specifics, every procedure is individually accessed and tailored for each patient. Pre-treatment, the imaging technique angiography is regularly used. It utilizes the deposition of injected dye into the bloodstream, which is then visualized by taking X-ray images. This can help map the arterial structure and aid the medical professionals in their insight. Post-treatment, imaging can again validate in-vivo simulations and delivery can be adjusted for follow-up treatment.

The procedure, see Figure 2.1, consists of the injection of radioactive microspheres via a catheter into the hepatic artery supplying the tumour cells in the liver. The blood flow in the artery transports the microspheres to the hepatic arterioles, the branches of the liver vasculature. The objective of the procedure is to direct the microspheres to the correct location, in the vicinity of the malicious tumour cells. Over time, the particles form a cluster and build up at the site, where they emit ionizing radiation. The crucial principle which allows radioembolization to be feasible is the fact that (hepatic) tumour cells are predominantly supplied with blood delivered by the hepatic artery. Blood for healthy liver tissue is accounted for via the portal vein, hence reducing the risk of destruction of healthy tissue.

The operational principles of radiation can be outlined as follows: Beta radiation is emitted from the isotopes, which carry ionizing radiation. These are high-energy electrons that penetrate tissue up to a

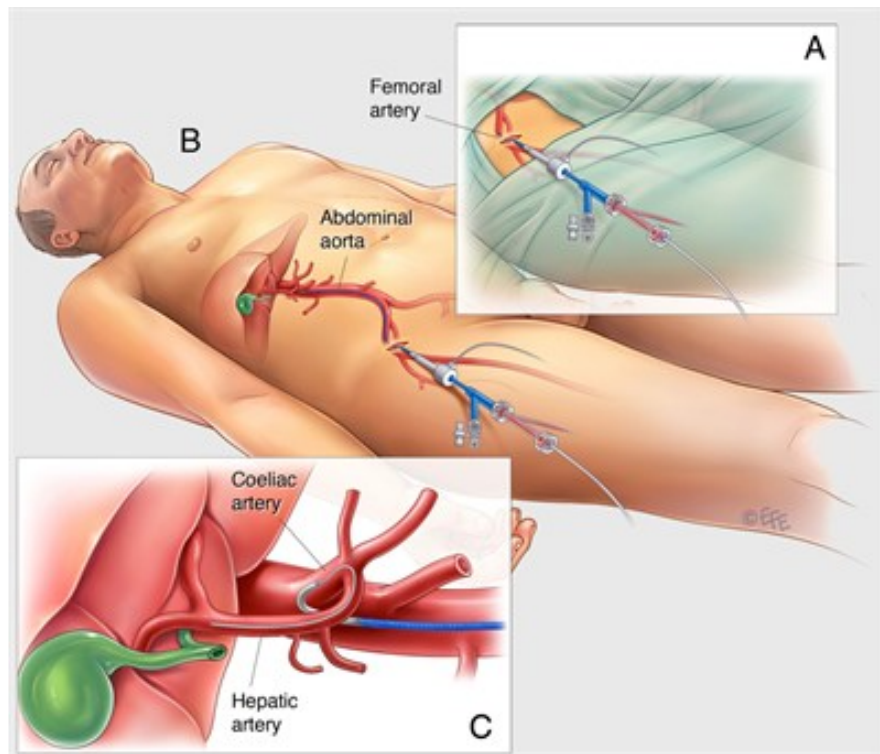


Figure 2.1: Supine position of the patient for treatment; A) Incision location for the catheter; B) Arterial structure; C) Location of hepatic artery [1].

small depth. While travelling, the particles continuously emit radiation which damages the structure of the cell DNA. It utilizes two processes, directly breaking the chemical bonds within the DNA strands or by formation of reactive oxygen components which indirectly damages the DNA. As stated previously, the radiation does not distinguish between malicious or healthy cells, so targeting the dose is of high importance.

These microspheres are very small ( $D \sim 40\mu m$ ) solid beads which carry a radioactive isotope, either embedded within or coated onto a microsphere particle. The particles themselves are solid, manufactured from bio-compatible resin of glass. The material acts as a stable matrix to contain the isotope. The exact type and dimensions of these microspheres are subject to the patient's needs and differ occasionally. The most commonly used isotope for this procedure in the medical world is Yttrium-90 ( $^{90}Y$ ). Its half-life is 64.1 hours, supporting a thorough and slow process in which the tumour can be addressed for a prolonged period. Patients can experience symptoms and side effects of the operation for up to two weeks. The beta-emitter isotope has been used quite extensively for radioembolization, resulting in a large body of clinical data and experience in operating procedures. The first studies with  $^{90}Y$  date back to the 1960s, in which its usage and applicability for human operations were analysed [9]. In 1999, the US FDA approved the usage of  $^{90}Y$  for unresectable HCC [10].

An alternative is Holmium-166 ( $^{166}Ho$ ), which has been studied for its therapeutic properties in recent years. Smits et al. [11] determined its maximum tolerable radiation dose. Radosa et al. [12] showed its clinical feasibility, technical success and exclusion of significant hepatotoxicity. Van Roekel et al. [13] found a same-day treatment procedure feasible. Stella et al. [14] explored future perspectives, including the possibility of a dual isotope.  $^{166}Ho$  possesses a significantly shorter half-life, 26.8 hours, allowing for a quicker reduction of the radiation and a shorter recovery period for the patient. Besides beta radiation,  $^{166}Ho$  also emits gamma radiation, which can be used in imaging techniques (especially scintigraphy)

and consequently aid in dosimetry. This double capacity is called dual-action, see Figure 2.2. Certain disadvantages of  $^{166}\text{Ho}$  over  $^{90}\text{Y}$  is its penetration range, which does not allow for reaching more deeply seated tumours. Secondly, from a logistic angle,  $^{166}\text{Ho}$  is less available and more expensive than  $^{90}\text{Y}$ . Finally, the accumulated experience, lengthy and rigorous admission criteria for new medical procedures and norm of usage of  $^{90}\text{Y}$ , hinder the widespread introduction of  $^{166}\text{Ho}$  for radioembolization. Nevertheless, development of  $^{166}\text{Ho}$  microspheres is ongoing and this thesis also utilizes these particles in this research.

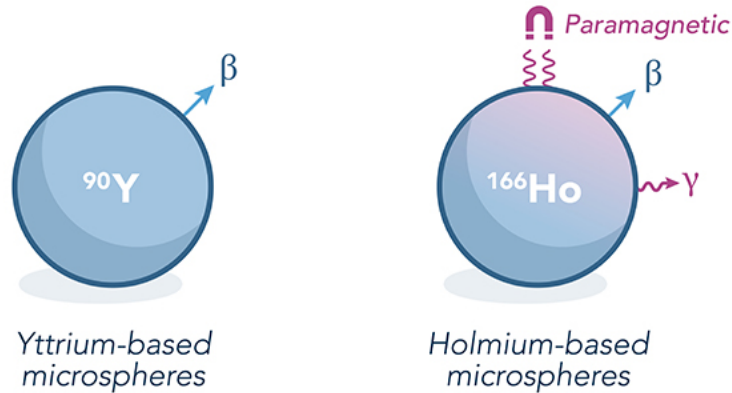


Figure 2.2: Radiation emission for  $^{90}\text{Y}$  and  $^{166}\text{Ho}$  [2].

For HCC, a prognosis of untreated patients ( $n = 600$ ) was found to be heterogeneous with a median survival rate of 9 months [15]. For colorectal hepatic metastases, with even shorter estimated median survival rates (4-5 months),  $^{90}\text{Y}$  radioembolization treatment ( $n = 531$ ) was found to prolong the median survival rate to 10.6 months [16]. Large-scale clinical trials (phase II or III) involving  $^{166}\text{Ho}$  radioembolization have not been performed. A recent study of colorectal metastases ( $n = 40$ ) found a median survival rate of 10.7 months for treatment with  $^{166}\text{H}$  while emphasizing the importance of personalized dosimetry [17].

Even though radioembolization is usually an option in advanced or terminal stages of liver cancer, its application is not restricted. In some recorded cases, radioembolization is part of a multimodal treatment approach, pairing it with other procedures like chemotherapy or surgical intervention. From a clinical point of view, earlier stages of liver cancer can also benefit and be treated with radioembolization. In clinical practice however this is unconventional, given the curative intent of early-stage liver cancer treatment and the accompanying incompatibility of radioembolization. Furthermore, risk-benefit assessment most likely discourages its usage. At last, standard protocols combined with the current limited clinical evidence don't favour early employment but rather exhaust known treatment options first. Nonetheless, ongoing research on radioembolization might spark discussion for alternative implementation and comprehension of the procedure, which aids in prolonging the median survival time of patients, albeit with its own set of challenges.

## 2.2 Arterial flow dynamics & Cardiac cycle

Figure 2.3 displays the anatomy of the liver vasculature. The artery utilized in TARE is the right hepatic artery, which supplies oxygenated blood to the right lobe of the liver. The total blood supply to the liver is supplemented by the contribution of the portal vein, which supplies a large proportion of the blood flow to the liver. The portal vein mainly feeds healthy tissue, while the right hepatic artery usually feeds the tumorous cells. The blood entering the right hepatic artery originates from the common hepatic artery, which is connected via the celiac trunk to the abdominal aorta. The right hepatic artery branches into segments through bifurcations, which reduce the vessel's diameter and flowrate, a relation consistent up to the capillaries. The initial bifurcation separates the flow into the anterior- and posterior segmental branches. The right hepatic artery is typically 3-5 mm in diameter and 40-60 mm in length.

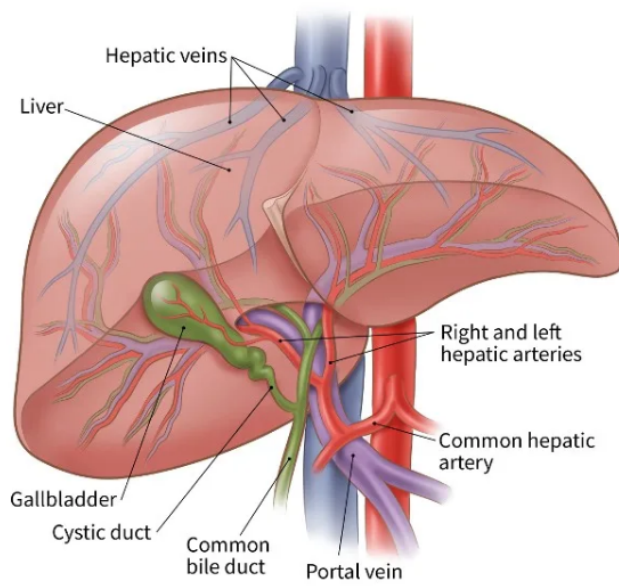


Figure 2.3: Liver vasculature, right hepatic artery in red [3].

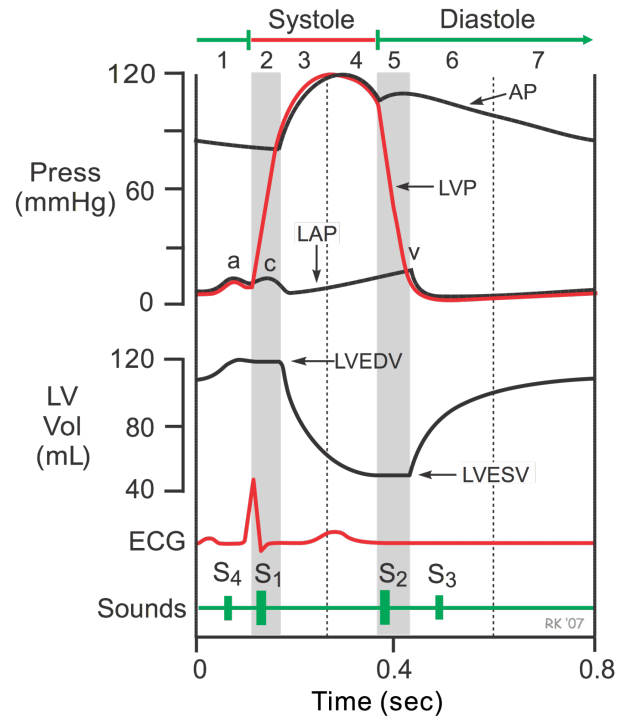


Figure 2.4: The cardiac cycle expressed in several measures 1) Pressure; 2) Volume flow rate; 3) Electrocardiogram; 4) Sound [4].

Characteristics of blood flow into the right hepatic artery result from the interplay between anatomical features and physiological factors. A cylindrical shape of the vessel can be distinguished. The inner layer surrounding the lumen is composed of endothelial cells, part of the Tunica Intima, which influence surface roughness. The diameter might exhibit fluctuations itself, due to health issues such as plaque formation or inflammation. Moreover, the pressure inside the vessel is dependent on the vessel's compliance (elasticity and distensibility). Physiologically, the blood originating from the heart is inherently pulsatile in nature, a result of the rhythmic contraction and relaxation of the heart muscles. An overview of the cardiac cycle can be seen in Figure 2.4.

Of particular interest are two basic phases: the diastole (relaxation of muscles, inflow of blood in chambers) and the systole (contraction of the muscles, ejection of blood from the ventricles). During diastole, the flow velocity and pressure are low. Both quantities increase to a maximum value at peak systole. In Figure 2.4, the "LV vol" represents the left ventricular volume, which is emptied during systole. A periodic nature can be extracted from the out-flowing blood volume curve. Arteries will accommodate the in-flowing blood by expanding or retracting, however, not all variations can be promptly accounted for. These fluctuations propagate through the vasculature, affecting shear stress on walls, arterial pressure and fluid velocity through the vessel.

The intensity of the pulsatility of the flow can be examined by using the Womersley number ( $Wo$ , or  $\alpha$ ):

$$Wo = \alpha = L \left( \frac{\omega}{\nu} \right)^{\frac{1}{2}} \quad (2.1)$$

Where  $L$  is the characteristic length scale [m],  $\omega$  the angular frequency [ $\frac{1}{s}$ ] and  $\nu$  the kinematic viscosity

$[\frac{m^2}{s}]$  of the blood. It is a ratio of the transient inertial forces over the viscous forces in the flow. It indicates the extent to which laminar flow deviates from quasi-steadiness. Two classes are distinguished:

- High  $Wo$  ( $Wo \gg 1$ ): Applicable in arteries with high pulsatile flowrates, e.g. the aorta. The flow rapidly responds to acceleration and deceleration induced by the cardiac cycle, hence exhibiting temporal variations. It is characterized by flow separation, re-circulation and turbulence.
- Low  $Wo$  ( $Wo \ll 1$ ): Typical for small arteries, where viscous effects dominate, more laminar and steady flow, thus less temporal variations.

Typical values for  $Wo$  in the right hepatic artery are in the range of 1 – 4 indicating the significance of temporal variations.

Another relevant factor to consider, which is grouped as one, is the hematological properties of blood itself. Hemodynamics in the cardiovascular system significantly depends on these factors, namely:

- Blood viscosity; resistance against shear forces and dictates flow resistance, primarily dependent on flow composition and temperature.
- Hematocrit; the total percentage of red blood cells compared to white blood cells, platelets and plasma.
- Plasma proteins; composition may affect blood rheology.
- Oxygen saturation; in-direct alters metabolic demands and tissue perfusion.

Additional factors such as blood pH, coagulation factors, electrolyte levels and remaining blood composition may all influence viscosity to some extent.

Now that the very basics of the vasculature system and its physiology are briefly discussed, an approach to modelling the system's geometry and flow conditions can be initiated, which is elaborated upon in Section 5.1.1.

## 2.3 Current state of research

As discussed in the previous section, the hepatic artery is an intricate blood vessel with a range of blood flow conditions, making the prediction of particles complex. As stated in Section 2.1, gaining insight into the distribution of these microsphere particles is crucial for delivering the dose to the tumour location. The challenges of a suitable procedure lie with the injection strategy, position of the catheter, particle concentration, timing of the dose, composition of blood and layout of the patient's arterial structure, among other factors. However, despite the influence of these parameters, it is important to focus on the research objective of this thesis and stick to the timing of the particle release and the subsequent mixing behaviour. Therefore, this section aims to map the existing research regarding particle transport and mixing, stenosed pipe flow, (onset of) turbulence and the application to LBM.

Regarding stenosed pipe flow and the onset of turbulence, Samuelsson et al. [18] investigated flow through a sinuous stenosis at varying  $Re$  and non-axisymmetric shapes using direct numerical simulation (DNS) and global linear stability analysis. It finds that at low  $Re$ , the flow remains steady and symmetric, but as the  $Re$  increases, it bifurcates into a symmetric steady state and an eccentric, non-axisymmetric steady state, with the latter becoming dominant at higher  $Re$ , while introducing an offset of the stenosis throat affects the bifurcation  $Re$  significantly. Additionally, Jain [19] investigated the impact of stenosis severity and configuration on the transition from laminar to turbulent flow under oscillatory conditions in arterial flows. It found that higher stenosis severity and eccentricity lead to earlier turbulence onset, while higher oscillation frequencies amplify hydrodynamic instability, particularly in milder stenosis cases. Moreover, using Doppler sonography, Lafortune et al. [20] found that the flow in the right hepatic artery can become partially turbulent, albeit not specifying a Reynolds regime. Finally, a prevalence of 3.5 % for

Hepatic Artery Stenosis (HAS) after liver transplantations in patients ( $n = 253$ ) was found by Da Silva et al. [21].

Concerning the flow regime in the right hepatic artery, a number of sources exist which calculate, predict or measure the Reynolds number of the flow inside the vessel. Amili et al. [22] chose to investigate two flows for a similar study to predict how particles travel through successively bifurcating vessels. These include  $Re = 470$  and  $Re = 930$ . In order to establish boundary conditions for physiological outflows Aramburu et al. [23] used  $Re = 722$ .

In relation to particle transport in turbulent flows, Reeks [24] discussed methods for simulating the transport, mixing, and agglomeration of small particles in turbulent gas flows. It introduces a PDF approach to represent particle behaviour, focusing on large-scale dispersion in homogeneous turbulence and turbulent boundary layers, as well as small-scale transport, highlighting the role of particle inertia and collision processes in enhancing agglomeration.

For studies on particle behaviour in flows, Liu et al. [25] analysed inertial particle migration effects using LBM and found two cases where the migration effects could be observed: Low particle concentration ( $< 5\%$ ) at low  $Re$  ( $< 20$ ) and high particle concentration ( $> 20\%$ ) and at moderate  $Re$  ( $> 20$ ). Secondly, Matas et al. [26] studied the inertial particle migration effect in Poiseuille flow at increasing  $Re$  and found discrepancies regarding established theory on the distribution of particles. When  $Re$  increases, particle migration effects cause the particles to group together at the inner annulus of the circular cross-section at a longitudinal distance of  $L = 310D$ .

Finally, regarding studies on particle implementation in LBM, Khalili et al. [27] demonstrated the efficiency and accuracy of a GPU-based implementation of the Lattice Boltzmann Method coupled with the Smoothed Profile Method (SPM) for simulating three-dimensional particulate flow. Results show good agreement with previous studies, indicating the potential of this approach for efficient and accurate particulate flow simulations.

At the University of Twente (UT), several different groups are collaborating to further investigate the procedure of Transarterial Radioembolization. The latest review [28] examined factors influencing microsphere distribution during TARE for liver cancer treatment. It encompasses in-vivo, ex-vivo, in-vitro, and in-silico studies to identify intra-procedural parameters affecting microsphere distribution. The analysis of 42 studies reveals that flow distribution is not a perfect predictor of microsphere distribution, while increasing injection velocity may enhance the similarity between them. Notably, microsphere distribution is highly sensitive to catheter position, particularly radially and axially. Promising parameters for future research and clinical application include microsphere injection velocity and axial catheter position, with emphasis on translating findings to patient-specific scenarios for enhanced treatment efficacy.

The foundation of a computational model of the liver vasculature, regarding research at the UT, has been laid by van de Hoek [29] with his Master's thesis, who acquired insights into the velocity field inside the hepatic artery and found LBM a suitable CFD technique to analyse a physical simplified model.

Meanwhile, ongoing PhD work by Vlogman [30] [31], aims to add a particle solver module to the existing LBM solver Musubi. This enables for intricate analysis of particle kinematics, facilitating the investigation of particle mixing behaviour through the module he has constructed. A more elaborate explanation is found in Subsection 4.2.1.

**Research Gap** *For certain types of radioembolization treatments, the process works efficiently if the microsphere particles have mixed with the bloodstream, the exact mechanisms of this mixing are unclear.*

*Prior research has shown that flow in the right hepatic artery is likely to depart from the laminar regime, because of the presence of irregularities of the lumen, dynamics of the artery and pulsatile inflow conditions.*

*A stenosis is a naturally occurring phenomenon in the right hepatic artery and can act as a small onset for turbulent flow.*

*It is hypothesized that the particles ejected from the catheter will mix with the non-laminar flow in the hepatic artery due to the stenosis onset.*

To summarize this section, a brief overview of the procedure of radioembolization is presented, combined with the anatomy and physiology of the right hepatic artery. Additionally, the basis in terms of literature review is established. This underscores the research gap that this research aims to fill. The next section addresses the theory behind the lattice Boltzmann method.

## Chapter 3

# Theory: Lattice Boltzmann Method

The Lattice Boltzmann Method (LBM) is a powerful numerical technique for simulating fluid dynamics, which has emerged over the past decades as a viable alternative to conventional Computational Fluid Dynamics (CFD) methods such as the more traditional Finite Element Method (FEM) and Finite Volume Method (FVM). The main advantages of LBM compared to FEM or FVM lie in its inherent simplistic foundation and its subsequent level of parallelization, making it suitable for high-performance computing. Even though the amount of computations is generally higher in LBM, due to the simplistic essence of the algorithm, computations are less time-intensive and hence faster. In addition, LBM allows for the division of the domain into multiple sections which can be solved separately and simultaneously by combining a collective of CPUs. To understand the difference in working principle between LBM and conventional CFD methods, the starting point of both approaches are briefly elaborated upon.

In FEM or FVM, a continuous approach is taken for the analysis of fluids, which implies that a to-be-investigated 'blob' of fluid is seen as one homogeneous section, disregarding individual particles and their interactions. Given this assumption, the conservation equations of mass, momentum and energy are solved on a control volume, leading to a set of differential equations. The resulting continuity equation in combination with the momentum equation, also known as the Navier-Stokes equations (NSE) can describe any velocity field of any fluid, albeit an extensive equation. Analytical solutions exist for simple applications but for more complex cases, numerical solutions are required and FEM or FVM have to solve the NSE for numerous control volumes. This approach is suitable given that the continuous assumption is still valid, which generally holds for macroscopic applications. However, in the microscopic range, this assumption no longer applies when intra-molecular forces obtain a more dominant role.

Now consider an alternative approach of a collection of separate particles randomly moving through space. The position and velocity of every particle in the system are known at each time-instant and thus, the mass and momentum conservation balances can be solved for collisions between the particles. Macroscopic quantities can be derived from the kinetic energy of the system. The Molecular Dynamics Methods (MDM) as simulations which utilize these principles, allow for a more detailed analysis, given that particle interactions are considered. The main drawback here is the amount of data required to describe a system using MDM, reducing its applicability to very tiny length scales, beyond engineering applications. For macroscopic applications, MDM is simply not feasible due to the computation-intensity of solving for the position and velocity of all particles for every time step in the system.

The introduction of statistical mechanics to the transport equations is one of the possible solutions for the length-scale problem. Significant reduction of computations while conserving accuracy allows for solving macroscopic problems with microscopic dynamics. The first person to come up with this train of thought was Ludwig Boltzmann in 1872 when he devised the so-called Boltzmann transport equation, which would later on form the basis of LBM.

In the following chapter, the foundation of theory regarding LBM is provided. Note that the terms atoms, molecules and particles are used interchangeably in the following chapter. The structure of this section is written after A.A.Mohammad's Lattice Boltzmann Method - Fundamentals and Engineering Applications with Computer Codes [32].

### 3.1 Kinetic Theory of gases

All matter in the observable universe, including all fluids, consist of atoms, which can be modelled as solid spheres or 'particles'. Consider a system of particles randomly moving through space while obeying Newton's second law, linear momentum conservation, see Equation 3.1.

$$\mathbf{F} = m \frac{d\boldsymbol{\xi}}{dt} = m \frac{d^2\mathbf{r}}{dt^2} \quad (3.1)$$

Assuming constant mass and neglecting rotational contributions; Here,  $\mathbf{F}$  is the force vector,  $m$  the particle's mass,  $\boldsymbol{\xi}$  the velocity vector and  $\mathbf{r}$  the position vector. In Figure 3.1, it can be seen that an externally applied force  $\mathbf{F}$ , due to a collision, alters a particle's velocity and position.

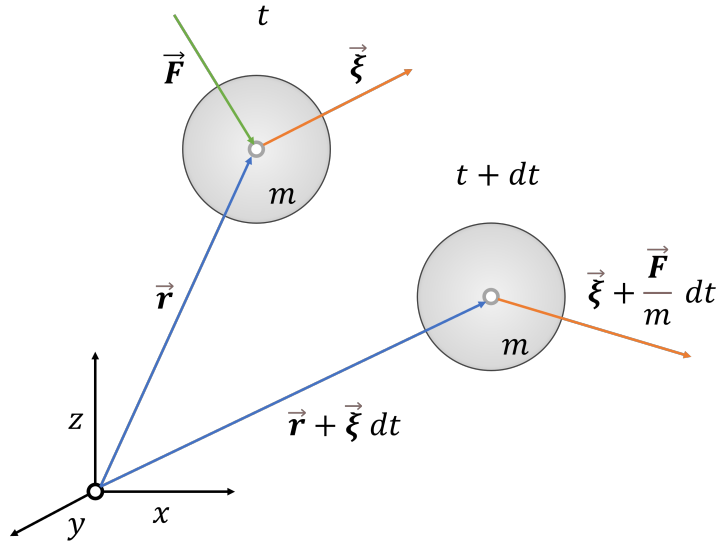


Figure 3.1: Simple particle collision model in 3D.

In Molecular Dynamics MD, this is the basis for molecular interactions and knowledge of the positions and velocities of particles can describe macroscopic quantities of a system. This is called the phase-space, in which the trajectory of a particles is its evolution in time.

$$P = \frac{2}{3} \tilde{n} E_k = \frac{1}{3} \tilde{n} m \xi^2 \quad (3.2)$$

The macroscopic property pressure is equivalent to force of the particles ramming the walls of the container per unit area. In Equation 3.2, the pressure is related to the kinetic energy of a system. Here,  $\tilde{n}$  is the number of particles per unit volume.

$$T = \frac{2}{3k_b} E_k = \frac{1}{3k_b} m \xi^2 \quad (3.3)$$

Similarly, the temperature of a system can also be rewritten as a function of the kinetic energy, see Equation 3.3. Here,  $k_B$  is Boltzmann's constant. The resemblance of these two properties is striking, and

unsurprisingly the ideal gas law ( $P = \tilde{n}k_B T$ ) connects them. It is important to note that the presented model is a simplification and only holds in certain conditions and for systems with particle dominant collisions. However, given its simplicity, it is fairly accurate for e.g. room temperature gas.

For truly microscopic configurations, where the amount of particles is sufficiently small, the above mentioned approach is suitable. It goes without saying that for reasonable real-world systems it is impossible to track each and every particles positions and velocity at every infinitesimal time-step. Luckily, a statistical approach offers a feasible method to capture the essence of the particle model whilst reducing computations. The next section elaborates on this translation, via a distribution function.

### 3.2 Maxwell-Boltzmann distribution

In 1859, Scottish physicist James Clerk Maxwell tackled the above mentioned problem by means of a distribution function. He recognized that the velocity can solely describe the state of a uniform gas in a container, which is the velocity distribution function. In this container, similar molecules are non-interacting and colliding, during which momentum is conserved. The initial positions and velocities of these particles are initially random and the average distance between particles is much larger than the particle diameter. This function characterizes the travelling molecules by 'bins' of velocity values, each with width  $dx$ . For a gas consisting of  $N$  molecules, the amount of molecules in  $x$ -direction with velocities between  $\xi_x$  and  $\xi_x + d\xi_x$  is equal to  $f(\xi_x)d\xi_x N$ . Noting the similarity for  $y$ - and  $z$ -directions, integrating over all possible velocities leads to Equation 3.4.

$$\int \int \int f(\xi_x)f(\xi_y)f(\xi_z)d\xi_x d\xi_y d\xi_z = N \quad (3.4)$$

Observing that directions are arbitrary and that only the speed of the molecules suffices, e.g.  $\xi = |\boldsymbol{\xi}| = \sqrt{\xi_x^2 + \xi_y^2 + \xi_z^2}$ , Equation 3.4 can be rewritten as follows

$$f(\xi_x)f(\xi_y)f(\xi_z) = \Phi(\xi_x^2 + \xi_y^2 + \xi_z^2) \quad (3.5)$$

Here,  $\Phi$  is a function to be determined. It can be shown that, considering the position of particles in a shell on a spherical surface, now only the speed  $\xi$  suffices to describe the number of particles in an interval. The full derivation of this function is left out. For a thermodynamic equilibrium system with a large number of identical, classical particles, the fraction of particles within an infinitesimal range of velocities in 3D phase space is given as

$$f(c) = 4\pi\xi^2 \left( \frac{m}{2\pi k_b T} \right) \exp\left( -\frac{m\xi^2}{2k_b T} \right) \quad (3.6)$$

Where  $\xi$  the particle's speed [ $\frac{m}{s}$ ],  $m$  is the particle's mass [ $kg$ ],  $k_B$  the Boltzmann constant [ $\frac{m^2 kg}{s^2 K}$ ] and  $T$  the temperature [ $K$ ]. It is important to note that the probability of finding a particle with an exact speed  $\xi$  is zero, but the probability is non-zero for finding particles in velocity ranges. In Figure 3.2, the distributions for  $x$  and  $x$  are given at different temperature.

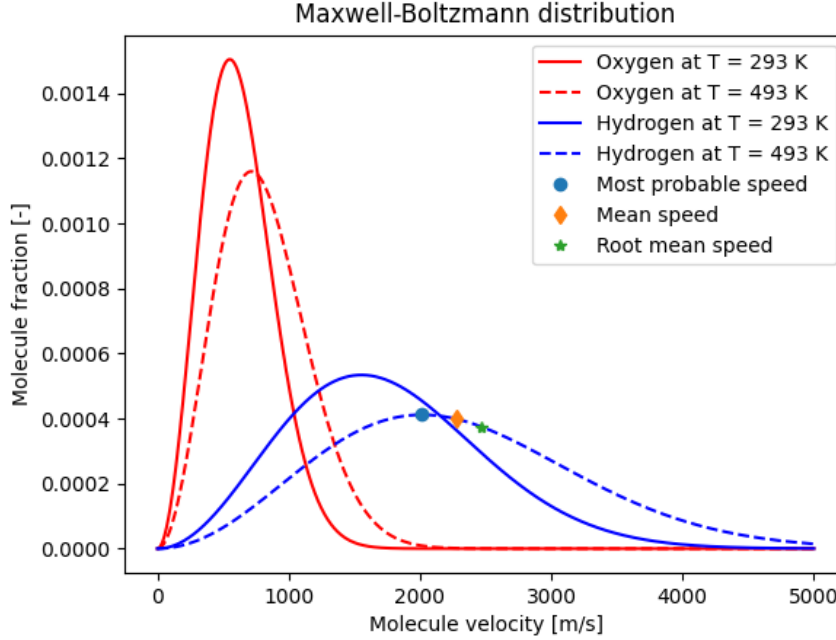


Figure 3.2: Maxwell-Boltzmann distribution for oxygen and hydrogen at different temperatures.

Note that the function is normalized and that the total area under each curve is equal to 1, conserving the total amount of particles  $N$ .

Ludwig Boltzmann was the first to establish a connection between the possible number of micro-states a systems can adopt ( $\Omega$ ) and the thermodynamic property of entropy ( $S$ ), via the equation  $S = k_B \log(\Omega)$ . “An increase in entropy is a change in macroscopic variables to those values corresponding to the largest possible number of microscopic arrangements [32].” Boltzmann was able to find the probability of a system in thermal equilibrium being in a particular state with energy  $E$  as:

$$f(E) \propto \exp\left(\frac{-E}{k_B T}\right) \quad (3.7)$$

After several computations, this proportionality can be shown to be equal to

$$f(\xi_x)f(\xi_y)f(\xi_z) = f(\xi) = \left(\frac{m}{2\pi k_B T}\right)^{\frac{3}{2}} \exp\left(-\frac{m\xi^2}{2k_B T}\right) \quad (3.8)$$

Which, multiplied by a factor of  $4\pi\xi^2$  (the surface area of a sphere in phase space), results in the Maxwell speed distribution as given in Equation 3.6. Recall that this distribution function holds for ideal gases in equilibrium, which is a crucial condition. Maxwell did not specify how this equilibrium is met. Boltzmann on the other hand, introduced a method to capture this movement toward equilibrium in his transport equation, which is the topic of the next section.

### 3.3 Boltzmann Transport Equation

Continuing on the distribution function, consider a system of particles again as depicted in Figure 3.1. If zero collisions would take place, the total number of particles  $f(r, \xi, t)$  will remain the same as the number

of particles after a hypothetical disturbance  $f(\mathbf{r} + \boldsymbol{\xi}dt, \boldsymbol{\xi} + \mathbf{F}dt, t + dt)$ , leading to a conservation equation, which, integrated over phase space leads to:

$$f(\mathbf{x} + \boldsymbol{\xi}dt, \boldsymbol{\xi} + \mathbf{F}dt, t + dt)d\mathbf{x}d\boldsymbol{\xi} - f(\mathbf{x}, \boldsymbol{\xi}, t)d\mathbf{x}d\boldsymbol{\xi} = 0 \quad (3.9)$$

Here, it is clear that the number of particles  $f$  in an arbitrary velocity interval always remains constant, there are after all no external or internal forces which might accelerate or decelerate particles. In reality, particles do collide and numerous collisions occur every fraction of a second. Hence, this alters the conservation relation as in Equation 3.9, since it no longer conserves the number of particles in the interval  $d\mathbf{r}d\boldsymbol{\xi}$ . The net rate of change between the distribution function, before and after a collision is the collision operator  $\Omega$ , see Equation 3.10.

$$f(\mathbf{r} + \boldsymbol{\xi}dt, \boldsymbol{\xi} + \mathbf{F}dt, t + dt)d\mathbf{r}d\boldsymbol{\xi} - f(\mathbf{r}, \boldsymbol{\xi}, t)d\mathbf{r}d\boldsymbol{\xi} = \Omega(f)d\mathbf{r}d\boldsymbol{\xi}dt \quad (3.10)$$

Dividing Equation 3.10 by the interval  $d\mathbf{r}d\boldsymbol{\xi}dt$ , taking the limit as  $dt$  approaches 0, and expanding the total time derivative by the parameters in the phase space  $t, \mathbf{r}, \boldsymbol{\xi}$  yields

$$\frac{df}{dt} = \frac{\partial f}{\partial t} + \frac{\partial f}{\partial \mathbf{r}} \frac{d\mathbf{r}}{dt} + \frac{\partial f}{\partial \boldsymbol{\xi}} \frac{d\boldsymbol{\xi}}{dt} = \Omega(f) \quad (3.11)$$

Observing that  $\frac{d\mathbf{r}}{dt}$  is simply the velocity  $\boldsymbol{\xi}$  and similarly that  $\frac{d\boldsymbol{\xi}}{dt}$  is simply the acceleration, which, by Newton's second law ( $F = ma$ ), is equal to  $\frac{\mathbf{F}}{m}$ , the collision operator can be rewritten as

$$\frac{\partial f}{\partial t} + \boldsymbol{\xi} \cdot \frac{\partial f}{\partial \mathbf{r}} + \frac{\mathbf{F}}{m} \cdot \frac{\partial f}{\partial \boldsymbol{\xi}} = \Omega(f) \quad (3.12)$$

Considering the case without any externally applied force  $\mathbf{F}$ , the equation reduces to (vector notation) the Boltzmann Transport Equation, which is the central equation and building block of LBM.

$$\frac{\partial f}{\partial t} + \boldsymbol{\xi} \cdot \nabla f = \Omega(f) \quad (3.13)$$

This is basically an advection equation with source term ( $\Omega$ ), which relates a known collision operator  $\Omega$  to the distribution function  $f$ . However,  $\Omega$  is an intricate function, depending on  $f$  itself, which makes it difficult to solve. The next section provides a solution to this problem.

The relation of the distribution function  $f$  to macroscopic quantities like density  $\rho(\mathbf{r}, t)$ , velocity  $\boldsymbol{\xi}(\mathbf{r}, t)$  and energy  $e(\mathbf{r}, t)$  are given in Equations 3.14, 3.15 and 3.16, which are the conservation laws of mass, momentum and energy.

$$\rho(\mathbf{r}, t) = \int_V m f(\mathbf{r}, \boldsymbol{\xi}, t) d\mathbf{r} \quad (3.14)$$

$$\rho(\mathbf{r}, t) \mathbf{u}(\mathbf{r}, t) = \int_V m f(\mathbf{r}, \boldsymbol{\xi}, t) \boldsymbol{\xi} d\mathbf{r} \quad (3.15)$$

$$\rho(\mathbf{r}, t) e(\mathbf{r}, t) = \frac{1}{2} \int_V m f(\mathbf{r}, \boldsymbol{\xi}, t) (\boldsymbol{\xi} - \mathbf{u})^2 d\mathbf{r} \quad (3.16)$$

Note that these quantities can solely be obtained if an analytical solution of Equation 3.13 exists, which depends on the solving capabilities of the integro-differential function  $\Omega$ . For the current application, there is no need to dive into the world of mathematics and provide analytical solutions [33] [34]. From a practical point of view, it is much more interesting to look at the discretized version of Equation 3.13, in which the collision operator  $\Omega$  is approximated.

### 3.4 BGK approximation

As mentioned in Section 3.3, the collision operator is difficult to solve and makes the BTE impractical to use. However, in 1954, Bhatnagar, Gross and Krook (BGK) devised a simplified model to replace the collision operator without an additional significant error term [35]. This was later proven to be an acceptable substitution given that “the outcome of two body collisions is not likely to influence significantly the values of many measured quantities” [36]. The approximation is abbreviated after its three authors, and known in LBM theory as the BGK approximation and replaces  $\Omega$  by

$$\Omega(f) = \frac{1}{\tau} (f^{eq} - f) = \omega (f^{eq} - f) \quad (3.17)$$

Where  $\tau$  is the relaxation factor,  $f^{eq}$  is the local equilibrium distribution function and  $\omega$  the relaxation frequency ( $\omega = \frac{1}{\tau}$ ). If the difference between the two distributions is large, the number of collisions is high and vice versa. This difference is then multiplied by the relaxation frequency  $\omega$ , which is analogous to the viscosity. It dictates how fast this equilibrium between the two distributions is reached; a high value for  $\omega$  leads to a more rapid relaxation towards equilibrium and vice versa. The choice for  $\omega$  and its implications are further elaborated upon in Chapter 4. Substitution for  $\Omega$  in Equation 3.13 yields

$$\frac{\partial f}{\partial t} + \boldsymbol{\xi} \cdot \nabla f = \frac{1}{\tau} (f^{eq} - f) \quad (3.18)$$

The local equilibrium distribution function  $f^{eq}$  corresponds to the previously derived Maxwell-Boltzmann distribution function, see Equation 3.6. For a 3D system of particles travelling in a flow with macroscopic velocity  $\mathbf{u}$ , the Maxwell-Boltzmann distribution can be rewritten in terms of  $\boldsymbol{\xi}$ ,  $\mathbf{u}$ ,  $\rho$  and  $R = \frac{k_B}{m}$  and expanded as

$$f^{eq} = \frac{\rho}{(2\pi RT)^{\frac{3}{2}}} \exp\left(-\frac{(\boldsymbol{\xi} - \mathbf{u})^2}{2RT}\right) = \frac{\rho}{(2\pi RT)^{\frac{3}{2}}} \exp\left(-\frac{\boldsymbol{\xi} \cdot \boldsymbol{\xi}}{2RT}\right) \exp\left(-\frac{-2\boldsymbol{\xi} \cdot \mathbf{u} + \mathbf{u} \cdot \mathbf{u}}{2RT}\right) \quad (3.19)$$

Which results in a lengthy exponential function. The second exponential term can be linearized and expanded by means of a Taylor series expansion:  $\exp(x) = 1 + x + \frac{x^2}{2!} + \frac{x^3}{3!} + \dots$

$$f^{eq} = \frac{\rho}{(2\pi RT)^{\frac{3}{2}}} \exp\left(-\frac{\boldsymbol{\xi} \cdot \boldsymbol{\xi}}{2RT}\right) \left[1 - \frac{-2\boldsymbol{\xi} \cdot \mathbf{u} + \mathbf{u} \cdot \mathbf{u}}{2RT} + \frac{(-2\boldsymbol{\xi} \cdot \mathbf{u} + \mathbf{u} \cdot \mathbf{u})^2}{4R^2T^2} + \mathcal{O}(u^3)\right] \quad (3.20)$$

Up till the second-order, since higher order terms ( $\mathcal{O}(u^3)$ ) don't contribute significantly in this case and can be disregarded. Finally, two substitutions are performed to rewrite  $f^{eq}$  in terms of lattice parameters  $c_s$  and  $W(\boldsymbol{\xi})$ , namely

$$RT = c_s^2 \quad (3.21)$$

$$W(\boldsymbol{\xi}) = \exp\left(-\frac{\boldsymbol{\xi} \cdot \boldsymbol{\xi}}{2RT}\right) (2\pi RT)^{-\frac{3}{2}} \quad (3.22)$$

These definitions allow for the expression for the second-order accurate equilibrium distribution, see Equation 3.23

$$f^{eq} = \rho W(\boldsymbol{\xi}) \left[ 1 + \frac{2\boldsymbol{\xi} \cdot \mathbf{u} - \mathbf{u} \cdot \mathbf{u}}{2c_s^2} + \frac{(\boldsymbol{\xi} \cdot \mathbf{u})^2}{2c_s^4} \right] \quad (3.23)$$

The expression for the equilibrium distribution function in known parameters allows for discretization of the entire BTE. This is necessary to convert a continuous partial differential equation into a computationally feasible form, allowing the simulation of fluid dynamics on a discrete lattice grid. This lattice grid is the topic of next section, where discretization of the equations is performed, together with the structure of a lattice and choices regarding lattice type.

### 3.5 Discretization

The Boltzmann Transport Equation as given in Equation 3.18 is in continuous form, and must be converted to a discrete version in order to be applicable for numerical calculations. This process is called discretization and is required for all translations to the finite domain for computing analysis. Several options exist for numerical approaches including nodes, elements, control volumes or lattices. The discrete version of the BTE is given as

$$\frac{\partial f_i}{\partial t} + \boldsymbol{\xi}_i \cdot \nabla f_i = \frac{1}{\tau} (f_i^{eq} - f_i) \quad (3.24)$$

Where  $i$  denotes a finite integer step. In LBM, the selection is made for lattice elements, which are the 'building blocks' on a discrete grid. It divides a line, area or volume in an evenly spaced grid containing nodes.

Their origin dates back to cellular automaton and specifically lattice gas automata (LGA), the predecessor of LBM. LGA can be seen as a more simple (boolean) variant on a hexagonal lattice grid, with a simpler collision model compared to LBM. Its fundamentals have been extensively described by Schuster et al. [37] and are not discussed in more detail due to their exclusive historical relevance here.

Back to lattice elements. In LBM, it represents a specific velocity vector and accompanying distribution functions of finding a particle with different velocities at the node location. So it employs a probabilistic approach in order to determine the evolution of the velocity vector.

There exists a range of different lattice types based on the number of dimensions. Conventional notation is in the form  $DnQm$ , with  $n$  denoting the number of dimensions and  $m$  the number of flow directions. The most common 1D, 2D and 3D stencils are given in Figure 3.3. Other conventional 3D lattices include D3Q13, D3Q15 and D3Q27.

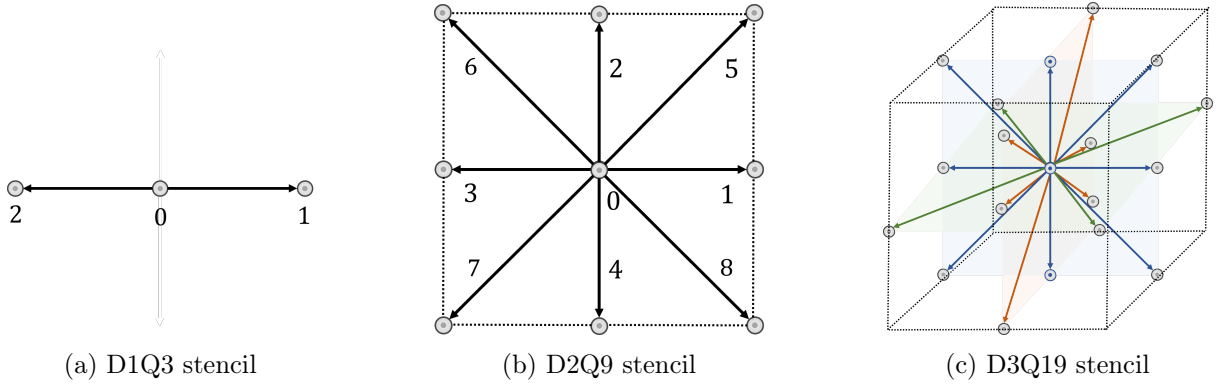


Figure 3.3: Three common lattice types for 1D, 2D and 3D.

The D3Q19 stencil, as displayed in Figure 3.3c is selected for all simulations in this thesis. It is found to possess the best accuracy to computational time ratio out of the 3D lattice options for this research. However, for the sake of simplicity, the D2Q9 lattice as displayed in Figure 3.3b is used in the remainder of the analysis of this section. In Figure 3.4, the distribution functions of an arbitrary time instant are given for visualization purposes.

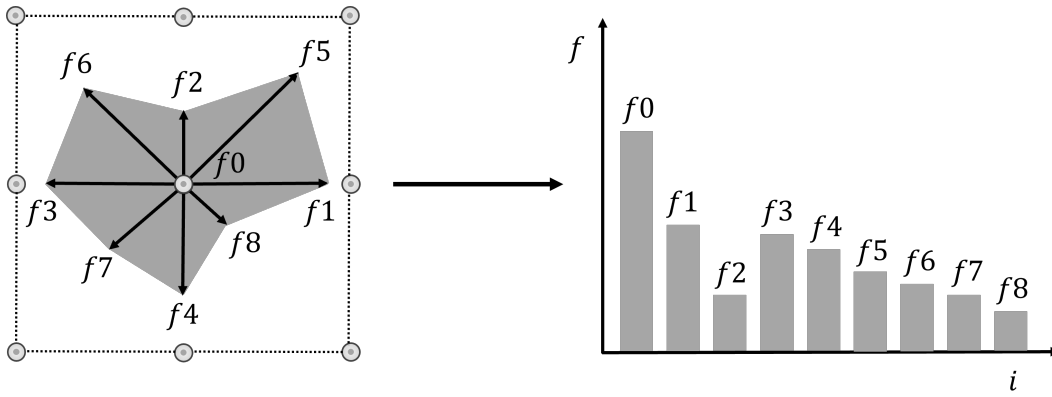


Figure 3.4: D2Q9 stencil with distribution functions.

As can be seen, a total of 8 streaming directions can be distinguished plus an additional slot for a particle at rest ( $f_0$ ). A single direction  $f_i$  can be seen as a direction-specific density. Each of these directions coincides with a certain velocity vector  $\mathbf{c}_{i\alpha}$ , with subscript  $i$  identifying the particle and  $\alpha$  the velocity components. Furthermore, isotropy of the lattice must be conserved. This is guaranteed by weighting factors  $w_i$ . For a particle residing at its location, a large weight is assigned. For a particle travelling a long distance, a small weight is assigned. For particles travelling the same distance, the same weight is applied, regardless of direction. The weighting factors for the D2Q9 stencil are given in Equation 3.25.

$$w_i = \begin{cases} \frac{4}{9} & i = 0 \\ \frac{1}{9} & i = 1, 2, 3, 4 \\ \frac{1}{36} & i = 5, 6, 7, 8 \end{cases} \quad (3.25)$$

The weighting factors obey certain conditions like conservation of the total density, conservation of symmetry and isotropy. This is mathematically expressed in Equation 3.26, which is the standard equation for moments of probability distributions.

$$M_n = \sum_{i=0}^m (w_i \cdot c_{i,1}^n \cdot \dots \cdot c_{i,d}^n) \quad (3.26)$$

Here,  $n$  is the order of the moment,  $m$  is the number of streaming directions,  $i$  is the discrete velocity vector index and  $d$  is the dimension of the lattice. For the D2Q9 lattice under consideration, the equation reduces to

$$M_n = \sum_{i=0}^8 (w_i \cdot (c_{i,1})^n \cdot (c_{i,2})^n) \quad (3.27)$$

Consider the first three moments for sake of understanding. The first moment is simply the summation of all weighting factors, which should equal 1 to conserve the total density

$$M_0 = \sum w_i = 1 \quad (3.28)$$

The first moment represents the conservation of symmetry, which should be independent of the rotation of the lattice

$$M_1 = \sum w_i \mathbf{c}_{i,1} = 0 \quad (3.29)$$

The second moments and onwards are the result of isotropy conditions. A lattice element should give the same outcome when rotated  $90^\circ$  in any arbitrary direction around its axis.

$$M_2 = \sum w_i \cdot (\mathbf{c}_{i,1})^2 + (\mathbf{c}_{i,2})^2 \quad (3.30)$$

Isotropy can not always be conserved, depending on the lattice structure. It is, however, favourable to possess isotropy up to a certain order. The D3Q19 lattice exhibits isotropy up to the 4<sup>th</sup> order, which suffices [38].

Now that the grid on which the BTE is discretized is discussed, recall the discretized BTE, as given in Equation 3.24. This equation also contains the equilibrium distribution  $f_{eq}$ , but now discretized. Therefore, Equation 3.23 is discretized over a standard lattice speed, which yields

$$f_i^{eq} = \rho \omega_i \left[ 1 + \frac{2\xi_i \cdot \mathbf{u} - \mathbf{u} \cdot \mathbf{u}}{2c_s^2} + \frac{(\xi_i \cdot \mathbf{u})^2}{2c_s^4} \right] + \mathcal{O}(u^2) \quad (3.31)$$

This equation is second-order accurate and the lattice speed of sound  $c_s^2$  for both D2Q9 and D3Q19 configurations is  $\frac{1}{3}$ . Substitution into  $f_i^{eq}$  yields

$$f_i^{eq} = \rho \omega_i \left[ 1 + 3(\xi_i \cdot \mathbf{u}) - \frac{3}{2}(\mathbf{u} \cdot \mathbf{u}) + \frac{9}{2}(\xi_i \cdot \mathbf{u})^2 \right] + \mathcal{O}(u^2) \quad (3.32)$$

Note that for the flow being analysed in this research, namely incompressible flow, the density  $\rho$  is always constant and the flow field is divergence-free. However, due to the inherent nature of LBM, it can be challenging to constrain the density at all times. In 1997, He and Luo found a substitution for the density, which significantly improves the applicability of incompressible flow [39]. The density is split up

between a constant contribution  $\rho_o$  and a fluctuation term  $\delta\rho$ , which is second-order accurate. Applying the substitution  $\rho = \rho_o + \delta\rho$  gives

$$f_i^{eq} = \omega_i \left[ \rho + \rho_o \left( 3(\boldsymbol{\xi}_i \cdot \mathbf{u}) - \frac{3}{2}(\mathbf{u} \cdot \mathbf{u}) + \frac{9}{2}(\boldsymbol{\xi}_i \cdot \mathbf{u})^2 \right) \right] + \mathcal{O}(u^2) \quad (3.33)$$

This notation of  $f_i^{eq}$  can be substituted back into the discretized BTE. Note that for a flow velocity of zero ( $\mathbf{u}$ ), the equilibrium distribution function reduces to  $f_i^{eq} = \rho w_i$ , a constant value with the weights proportional to each velocity direction, multiplied by the density. This reflects the absence of any fluid motion. Therefore, all distribution functions of the lattice nodes are uniform.

This section introduced the fundamentals of the lattice model. What remains is to elaborate on the evolution of the procedure (LBM Procedure, Section 3.6) and the demarcation of the lattice (Boundary conditions, Section 3.7).

### 3.6 LBM Procedure

Let's recall the BTE as derived in Equation 3.24

$$\frac{\partial f_i}{\partial t} + \boldsymbol{\xi}_i \cdot \nabla f_i = \frac{1}{\tau} (f_i^{eq} - f_i) \quad (3.34)$$

From a technical stance, Equation 3.24 is a linear (no non-linear terms of  $f$  in r.h.s.) partial ( $f$  differentiated w.r.t spatial coordinates and velocity) differential equation. It also resembles an advection (transport by bulk motion) equation with the r.h.s. as source term. Discretization of Equation 3.24 yields

$$\underbrace{f_i(\mathbf{r} + \boldsymbol{\xi}_i \Delta t, t + \Delta t) - f_i(\mathbf{r}, t)}_{\text{Streaming}} = \frac{\Delta t}{\tau} \underbrace{(f_i^{eq}(\mathbf{r}, t) - f_i(\mathbf{r}, t))}_{\text{Collision}} \quad (3.35)$$

In which the l.h.s represents the 'streaming' step and the r.h.s the 'collision' step. In the first step, particles travel to neighbouring nodes and in the second step, upon arrival of these particles at the nodes, an exchange of momentum takes place which is appropriately named 'collision'. Note that these two processes are captured in a single equation but have to be separated when solid boundaries are present [40]. These two steps are the groundwork of LBM procedure and are explained in more detail.

The streaming process for a D2Q9 lattice is displayed in Figure 3.5

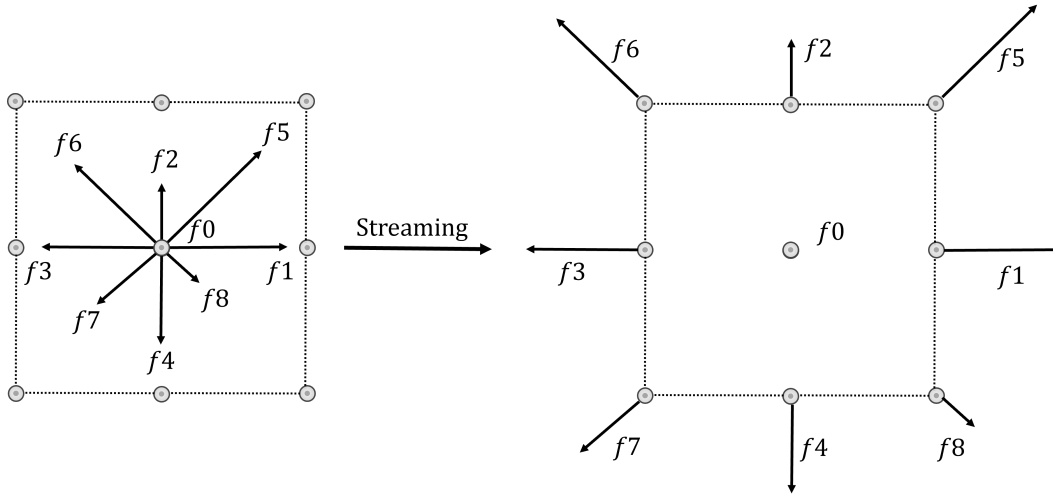


Figure 3.5: Streaming step for D2Q9 configuration.

As can be seen, the particle distributions have propagated through the lattice to the adjacent nodes during the time-step  $\Delta t$ . In this specific case, no collisions occur and the distributions simply translate to neighbouring nodes.

More commonly, however, collisions have to be included. The essence of this model lies within the locality of collisions; The particle-particle collisions take place within the distribution function and can solely be evaluated and processed with information at the node in question.

'During' the time-frame in-between the streaming- and collision-step, the particles are considered to be in an interstitial state, notated by the \*-superscript. The relation between the two steps is as follows

$$f_i = f_i^* - \omega(f_i^* - f_i^{eq}) \quad (3.36)$$

Note that numerical problems occur when  $\omega = 1$ , an issue which is addressed in Section 4.2. The general step-wise procedure is simplified in six steps:

1. Initialization of  $\rho$ ,  $\mathbf{u}$ ,  $f_i$  and  $f_i^{eq}$ . These follow from the initial prescribed conditions.
2. *Streaming*: Movement of the distribution functions in lattice directions ( $f_i \rightarrow f_i^*$ )
3. Compute new  $\rho$  and  $\mathbf{u}$  from the interstitial state using

$$\rho = \sum_{i=0}^N f_i \quad (3.37)$$

$$\mathbf{u} = \frac{1}{\rho} \sum_{i=0}^N \boldsymbol{\xi} f_i \quad (3.38)$$

4. Compute new  $f_i^{eq}$  using derived  $\rho$  and  $\mathbf{u}$
5. *Collision*: Calculate new distribution function  $f_i$  according to 3.36
6. Repeat steps 2-5 until clock is terminated.

Two different types of collision can be distinguished, due to walls or distribution functions from neighbouring lattice elements. The former is elaborated upon in Section 3.7, while the latter can be easily visualized; Imagine a lattice of D2Q9 configuration, as in Figure 3.5. Distribution function  $f_2$ , travelling north, will encounter a southwards travelling  $f_4$  from the neighbouring element, and collide at the node, where momentum is exchanged among other distribution functions.

### 3.7 Boundary conditions

If no external conditions are prescribed to a lattice, their nodes span infinitely, because every node has a neighbour in all directions. Thus, the lattice must be contained. The ingredients to spatially shape the LBM simulation are Boundary Conditions (BCs). They provide the required stability for numerical solutions. The imposed macroscopic boundaries on the fluid have to be analysed on their distribution function level. Several types of boundary conditions might be employed depending on the prescribed conditions. The two most important and relevant for this research are addressed here, namely the Bounceback- (wall) and the Dirichlet (pressure) BCs.

#### 3.7.1 Bounceback

The Bounceback condition, also known as the no-slip boundary condition is the most common and straightforward BC and is present at any interface between a fluid and a surface wall. A choice can be made to either use nodes directly in the wall for returning the incoming distribution functions or alternatively, generate an extra row of nodes as 'placeholders'. The difference between 'on-node' or 'mid-node' bounceback planes determines the order of error type. The mid-node bounceback plane exhibits second-order error terms, instead of first but is not always applicable where the on-node bounceback is.

The general procedure is displayed in Figure 3.6. The three coloured distribution functions travel to the solid nodes, invert and are reversed and mirrored at their original location pre-streaming. This happens all in the timespan of a single time-step.

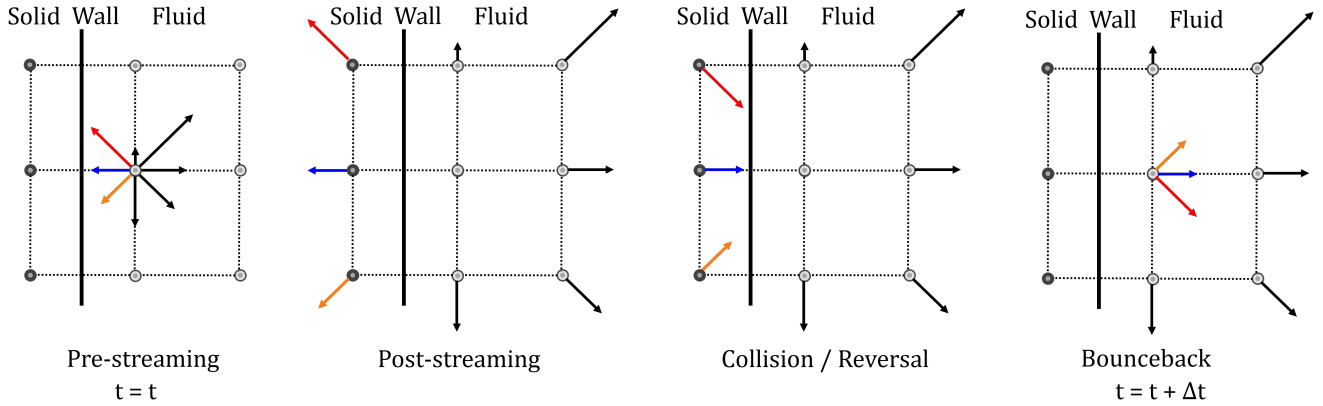


Figure 3.6: Four steps of the Bounceback Boundary Condition for D2Q9 configuration.

Even though the bounceback BC is tailored for fluid-wall interfaces, it can occasionally be used as a fluid inlet or outlet boundary. A periodic BC can also be used in cyclic systems, where the outlet of the domain serves as the input for the next repeating section.

#### 3.7.2 Dirichlet

The most common way to constrain the pressure at the inlet/outlet is by using a Dirichlet BC. This BC uses a key relation in LBM which relates the pressure to the density, which is given as

$$P = \rho c_s^2 \quad (3.39)$$

This allows for the evaluation of the pressure given a density at a node location. Equation 3.37 provides this local density value, which eliminates the need to evaluate the much more complex pressure Poisson equation in other CFD methods.

Again, consider a D2Q9 lattice grid as displayed in Figure 3.7. On the line between points A and B is a prescribed velocity  $\mathbf{u} = (u, v)$  flowing from west to east into the domain.

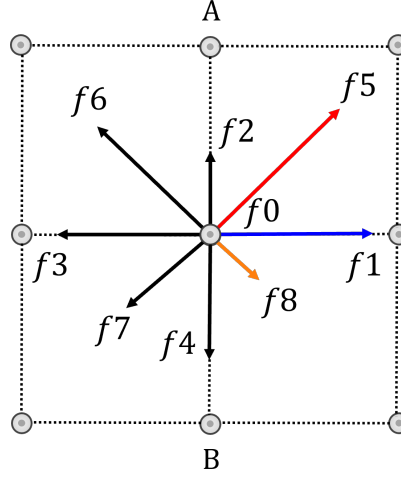


Figure 3.7: Dirichlet Boundary Condition for D2Q9 configuration.

Distributions  $f_0, f_2, f_6, f_3, f_7$  and  $f_4$  are known because of their origin from inside the domain, however  $f_8, f_1$  and  $f_5$  are unknown. In order to solve for these values, Equations 3.37 and 3.38 are expanded for this lattice arrangement, which yields

$$\rho = f_0 + f_1 + f_2 + f_3 + f_4 + f_5 + f_6 + f_7 + f_8 \quad (3.40)$$

for the density and

$$\rho u = f_1 + f_5 + f_8 - f_6 - f_3 - f_7 \quad (3.41)$$

$$\rho v = f_5 + f_2 + f_6 - f_8 - f_7 - f_4 \quad (3.42)$$

for the conservation of momentum in both spatial directions. Now,  $\rho$  is an additional unknown, but equilibrium of distribution functions over the velocity boundary presents the fourth equation. (The Bounceback rule still holds for the non-equilibrium part of the particle distribution function normal to the boundary. [40])

$$f_1 - f_1^{eq} = f_3 - f_3^{eq} \quad (3.43)$$

One might wonder why  $\rho$  is an unknown given the analysis of an incompressible fluid ( $\rho = \text{constant}$ ). This is due to the fact that the density is allowed to adjust in order to satisfy the prescribed velocity boundary condition.

The unknowns can be solved by rearranging the terms, which is excluded here. What remains are the relations for  $\rho, f_1, f_5$  and  $f_8$ .

$$\rho = \frac{1}{1-u} (f_0 + f_2 + f_4 + 2(f_3 + f_6 + f_7)) \quad (3.44)$$

$$f_1 = f_3 + \frac{2}{3}\rho u \quad (3.45)$$

$$f_5 = f_7 - \frac{1}{2}(f_2 - f_4) + \frac{1}{6}\rho u + \frac{1}{2}\rho v \quad (3.46)$$

$$f_8 = f_6 + \frac{1}{2}(f_2 - f_4) + \frac{1}{6}\rho u + \frac{1}{2}\rho v \quad (3.47)$$

All unknowns are accounted for. In the case of an outlet, an identical procedure can be performed for the westward-facing distribution functions, which yields the same result. Note that in the case of zero velocity inflow ( $u = v = 0$ ), the Dirichlet BC reduces to the velocity bounceback BC.

In the case of a prescribed pressure for an inlet or outlet, which is desired for this research, simply solve for the velocity instead by rearranging

$$u = 1 - \frac{1}{\rho}(f_0 + f_2 + f_4 + 2(f_3 + f_6 + f_7)) \quad (3.48)$$

which is applicable for a D2Q9 lattice ( $c_s^2 = 3$ ). The density is simply obtained from Equation 3.39.

Additionally, for known derivatives at boundaries (heat flux e.g.), a Von Neumann BC can be used in LBM. Further improvements and increases in accuracy can be achieved by Guo-Zheng-Shi [41] and Zou-He [42] BCs, however, are beyond the scope and/or not relevant to this research.

### 3.8 Chapman-Enskog expansion

Now that the theoretical groundwork for the LBM has been laid out, one might proceed directly to simulations. But one important question has not been addressed yet: How do the discrete particle dynamics, explained in the aforementioned sections lead to macroscopic fluid equations and fluid behaviour? I.e. are we really solving for a fluid? This section explores the proof that links the BTE to the NSE, known as the Chapman-Enskog expansion. These two physicists independently found the link between particle-based descriptions of a continuous hydro-dynamical model in 1916 [43] and 1917 [44]. This derivation is elaborated upon, in combination with the additional required tuning of the parameters in the results to obtain the NSE. The analysis closely follows the work of Li, *Appendix: Chapman-Enskog Expansion in the Lattice Boltzmann Method* [45]

The starting point of the derivation is Equation 3.35, which yields the discretized BTE, rewritten as

$$f_i(\mathbf{r} + \xi_i \Delta t, t + \Delta t) - f_i(\mathbf{r}, t) = \frac{1}{\tau}(f_i^{eq}(\mathbf{r}, t) - f_i(\mathbf{r}, t)) \quad (3.49)$$

The explicit updating algorithm is clearly a function of position ( $\mathbf{r}$ ) and time ( $t$ ). Introducing a Taylor expansion for the l.h.s. of Equation 3.49 yields

$$\sum_{n=1}^{\infty} \frac{\Delta t^n}{n!} D_t^n f_i(\mathbf{r}, t) = \frac{1}{\tau}(f_i^{eq}(\mathbf{r}, t) - f_i(\mathbf{r}, t)) \quad (3.50)$$

where  $D_t = \frac{\partial \phi}{\partial t} + \boldsymbol{\xi} \cdot \nabla \phi$ , also known as the material derivative, with  $\phi$  the property to be evaluated, in this case  $f_i(\mathbf{r}, t)$ . The material derivative can be seen as analysis of a property in a space-time-dependent

macroscopic velocity field. Introduction of the Chapman-Enskog expansion is now possible, in which  $f_i$  and  $\partial t$  are expanded into different 'orders', namely

$$f_i = f_i^{(0)} + \sum_{n=1}^{\infty} f_i^{(n)} = f_i^{eq} + \sum_{n=1}^{\infty} f_i^{(n)} \quad (3.51)$$

$$\partial_t = \sum_{n=0}^{\infty} \partial_{t_n} \quad (3.52)$$

With these mathematical definitions, it is possible to obtain the zeroth, first and second-order of magnitude of Equation 3.49, which is respectively given as

$$f_i^{(0)} = f_i^{eq} \quad (3.53)$$

$$\Delta t \frac{D}{Dt} f_i^{(0)} = -\frac{1}{\tau} f_i^{(1)} \quad (3.54)$$

$$\Delta t \frac{D}{Dt} f_i^{(1)} + \Delta t \frac{\partial}{\partial t_1} f_i^{(0)} + \frac{(\Delta t)^2}{2} \left( \frac{D}{Dt} \right)^2 f_i^{(0)} = -\frac{1}{\tau} f_i^{(2)} \quad (3.55)$$

Two assumptions are made in order to satisfy the conservation equations and to make each  $f_i^{(n)}$ -term solvable

$$\sum_i f_i^{(n)} = 0 \quad \forall n \neq 0 \quad (3.56)$$

$$\sum_i \xi_{i,j} f_i^{(n)} = 0 \quad \forall n \neq 0 \quad (3.57)$$

With the assumptions and the definition of Equation 3.53, Equation 3.54 can be rewritten in a suitable form (full derivation skipped), which yields the zeroth order moment

$$\frac{\partial \rho}{\partial t_0} + \frac{\partial(\rho u_j)}{\partial x_j} = 0 \quad (3.58)$$

And similar rewriting for Equation 3.55 yields

$$\frac{\partial \rho}{\partial t_1} = 0 \quad (3.59)$$

Now using the fact that  $\partial t \approx \partial t_0 + \partial t_1$ , the zeroth order moments in Equations 3.58 and 3.59 can be combined

$$\frac{\partial \rho}{\partial t} + \frac{\partial(\rho u_j)}{\partial x_j} \quad (3.60)$$

which resembles the conservation of mass equation in fluid mechanics. Similarly, expanding the first order moments of Equations 3.54 and 3.55 yields

$$\frac{\partial(\rho u_{j1})}{\partial t_0} + \frac{\partial}{\partial x_j} \left( \frac{c^2}{3} \rho \delta_{ij} + \rho u_i u_j \right) = 0 \quad (3.61)$$

$$\frac{\partial(\rho u_i)}{\partial t_1} + \left(1 - \frac{1}{2\tau}\right) \frac{\partial}{\partial x_j} \sum_i \xi_{i,j1} \xi_{i,j2} f_i^{(1)} = 0 \quad (3.62)$$

Again, full derivation left out, rewriting the second term in both equations, replacing the Kronecker delta and the sum over  $f_i^{(1)}$  yields

$$\frac{\partial(\rho u_i)}{\partial t} + \frac{\partial(\rho u_i u_j)}{\partial x_j} = -\frac{\partial}{\partial x_i} \left( \frac{c^2 \rho}{3} \right) + \frac{\partial}{\partial x_j} \left[ (\tau - 0.5) \Delta t \left( \frac{c^2}{3} \rho \left( \frac{\partial u_j}{\partial x_i} + \frac{\partial u_i}{\partial x_j} \right) - \frac{\partial}{\partial x_k} (\rho u_i u_j u_k) \right) \right] \quad (3.63)$$

And for comparison, the incompressible NSE, without external forces

$$\rho \left( \frac{\partial}{\partial t} + u_j \frac{\partial}{\partial x_j} \right) u_i = -\frac{\partial}{\partial x_j} p + \mu \nabla^2 u_j \quad (3.64)$$

Equation 3.63 shows similarities in structure with the NSE, albeit not completely similar yet. Tuning of parameters  $\Delta x$ ,  $\Delta t$  and  $\omega = \frac{1}{\tau}$  to ensure that the magnitude of  $\mathbf{u} \ll \frac{c_s^2}{3}$  essentially negates the relative variation of the density terms. Consequently, this leads to the reduction of  $-\frac{\partial}{\partial x_i} \left( \frac{c^2 \rho}{3} \right)$  to simply  $-\frac{\partial p}{\partial x_i}$ , which equals the pressure term in the NSE. Collecting all constants and variables in front of the Laplace operator ( $\nabla^2$ ) leads to

$$\mu = \frac{1}{3} \left( \tau - \frac{1}{2} \right) \Delta t \rho c_s^2 \quad (3.65)$$

Dividing this equation by  $\rho$  yields the kinematic viscosity, which is an essential parameter for LBM, more about this relation in Section 4.2.

### 3.9 Applications

As mentioned previously, the field of biophysical fluid mechanics is suitable for the application of LBM. This area is characterized by (moderately) complex flow geometries in combination with low Reynolds numbers. The lattice approach of LBM is more suitable for the viscous-dominated low Reynolds regimes. Additionally, modelling of high turbulence is often not reliable in LBM, which excludes high Reynolds number flows. An important dimensionless number which addresses the applicable flow regime is the Knudsen number  $Kn = \frac{\lambda}{L}$ , in which  $\lambda$  is the molecular mean free path and  $L$  is the characteristic length scale of the flow. LBM is mostly suitable for low  $Kn$ -values, also known as the continuum flow regime. In Figure 3.8, for a number of Knudsen numbers, their applicable models are presented.

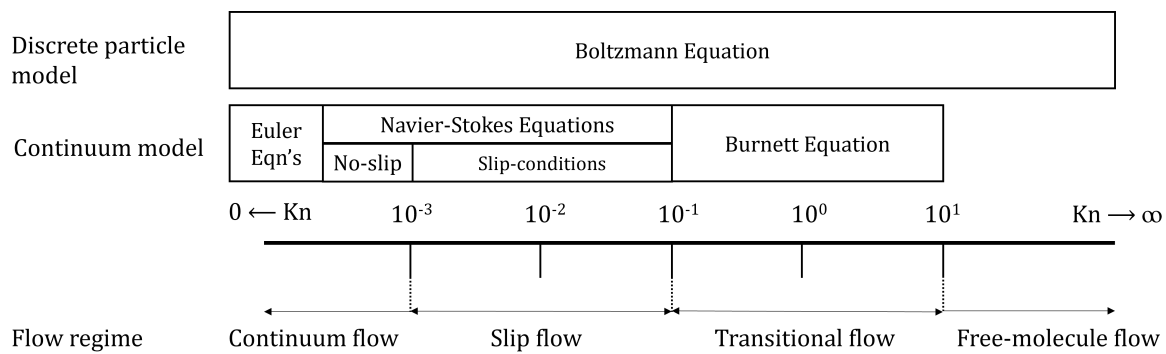


Figure 3.8: Overview continuum models as function of Knudsen number.

Other areas of application include the aforementioned biomedical flows, especially in complex microvasculature. It has also been used to model cerebrospinal fluid, a body fluid surrounding brain tissue. Secondly, porosity and permeability studies, such as membranes, filters and catalysts, with applications in the field of substrate flows and filtration processes. LBM also captures heat transfer quite comprehensively, again, most profoundly on the micro-scale. Examples of applications are microelectric-cooling and microscale thermo-fluidic systems. Finally, a number of multicomponent models have been developed to analyse multi-phase flows, which, in addition to conventional CFD techniques, require little to no treatment.

This section concludes the chapter about the Lattice Boltzmann Method. The next chapter delves more deeply into the LBM solver itself.

# Chapter 4

## Software: APES Simulation Framework

In the previous chapter, the ideas and formulas behind the Lattice Boltzmann method were discussed. This chapter focuses on the software package which takes care of these calculations and is used throughout this thesis, namely APES. This is a collection of tools in order to solve flow problems starting from the geometry to visualization of the results. The simulation suite is based on an octree mesh infrastructure and is capable of parallel computing. The APES simulation bundle is depicted in Figure 4.1 and is available for download at: <https://github.com/apes-suite>.

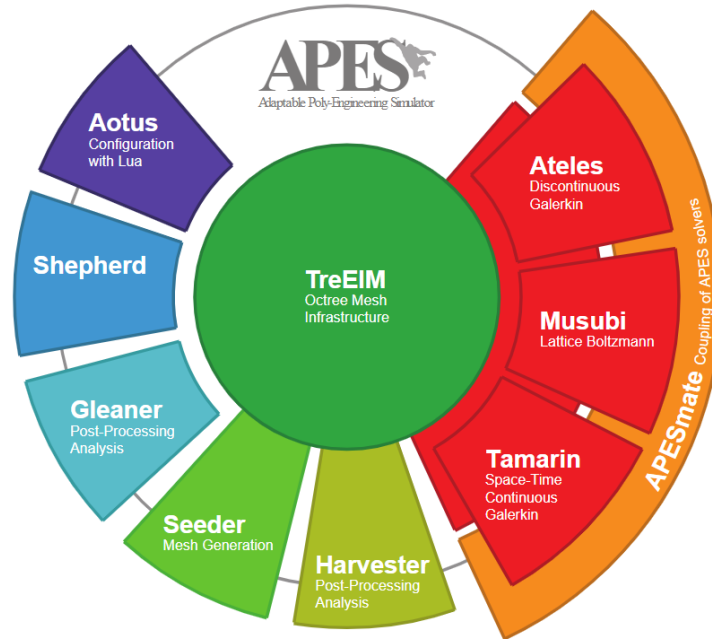


Figure 4.1: APES Simulation Framework [5].

The workflow starts with the first package called Seeder, which generates a structured mesh from a given geometry. Aotus sets up the simulation using lua scripts. Musubi then uses the mesh to calculate the flow field using the lattice Boltzmann method. Harvester prepares the results for post-processing tools, of which Matlab, Python and Paraview are used for visualization purposes. Inherently to LBM, the computational process can be split up and divided over several processing cores which drastically reduces computational time. This procedure of parallelization is used on the Dutch supercomputer Snellius. This section elaborates on all the important tools of the APES simulation framework used in this thesis.

## 4.1 Mesh generator: Seeder

Seeder is the mesh generator component of the APES packages. Its basic operating principles are discussed in this section.

In CFD, a mesh is the discretization of the geometric domain into interconnected elements. It is required to divide the geometry into smaller parts, shapes or sections in order to proceed with numerical methods, allowing for approximation of the governing equation over smaller, manageable regions. Additionally, a mesh also defines the boundaries and establishes the resolution, which in turn determines the accuracy of the simulation, in combination with the chosen numerical method. Using conventional FEM or FVM methods, the mesh size can be anisotropic, meaning an unstructured mesh of different-sized elements. This comes at the expense of describing each relation between neighbouring elements, adding to the computational complexity. In a LBM solver like Musubi, the mesh is uniformly structured, meaning the entire geometric domain is divided into similar-sized elements. This allows for parallelization, as described in Section 4.3.

Seeder is based on an octree principle, which implies partitioning the domain in all three Cartesian directions, resulting in eight smaller regions, or octants, see Figure 4.2. This hierarchical process is repeated until the desired level of refinement is achieved and the domain consists of  $n$  elements, see Equation 4.1.

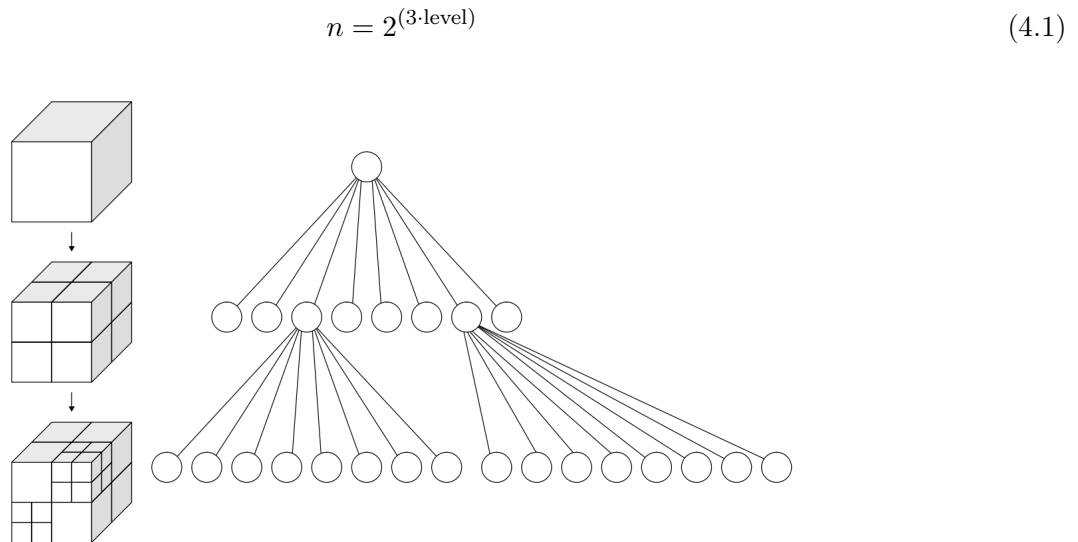


Figure 4.2: Octree procedure [6].

A bounding cube is an encompassing 'cube' containing, in any case, at least the geometry, which encloses the domain. The bisection algorithm uses this bounding cube to initialize the splitting of the geometry up to the stated level. This results in a 'box' of  $n$  elements, either being in- or excluded in the geometry. Every element coinciding with or located in the geometry is then labelled as a part of the definitive mesh. At this moment, the flooding procedure starts, which will flood all elements in the mesh. The flooding propagates from the location of a specified 'seed' within the geometry and stops when every element is 'filled'. Elements that overlap with the boundary of the geometry are not flooded, which emphasizes the necessity of grid refinement when geometries become more complex.

The level determines the number of bisections of the domain, thereby setting the resolution. From Equation 4.2, it can be seen that the level depends on the element length  $dx$ , which is specified beforehand

by the user and the length of the model  $L$ , which is by convenience the largest spatial dimension of the geometry. The level is an integer value, and any non-integer outcome is rounded up, which slightly adjusts  $dx$ . This can be fine-tuned by altering the dimensions of the bounding cube."

$$\text{level} = \log_2 \left( \frac{L}{dx} \right) \quad (4.2)$$

Main advantages of using the above-mentioned octree structure for mesh generation are its suitability for complex geometries, possibility for adaptive mesh refinement and efficient memory usage. Notable disadvantages include their implementation complexity and potential for numerical dispersion.

Seeder uses a combination of inputs to determine the mesh. The user can specify shapes for the geometry using a *.stl* file, containing a model including dimensions. Additionally, boundaries can be prescribed by defining planes in the *seeder.lua* input file, or Solver Input File (SIF). The bounding cube dimensions and seed location are also specified here. Before each simulation, the mesh can be 'harvested' and visualized for inspection to determine its applicability. The user can then visually identify and correct the mesh if needed.

In Table 4.1, a number of different resolutions of meshes are listed, for implication purposes. Note that is for a given geometry and numerous other parameters have an influence on the actual mesh properties. The distance step  $dx$  is halved for each grid refinement, leading to decreasing time step  $dt$  and consequently, higher computational costs. Note that the time is an approximation and depends on the amount of cores dedicated to the computation. See Section 5.1.2 for the actual determination of the mesh sizes used in this research.

| dx                   | dt                   | Total                     | Level |
|----------------------|----------------------|---------------------------|-------|
| $128 \times 10^{-4}$ | $4.4 \times 10^{-5}$ | $\approx 0.5 \times 10^6$ | 9     |
| $64 \times 10^{-4}$  | $1.1 \times 10^{-5}$ | $\approx 4 \times 10^6$   | 10    |
| $32 \times 10^{-4}$  | $2.7 \times 10^{-6}$ | $\approx 34 \times 10^6$  | 11    |
| $16 \times 10^{-4}$  | $6.9 \times 10^{-7}$ | $\approx 280 \times 10^6$ | 12    |

Table 4.1: Mesh sizes and implications for simulation parameters.

All resources related to Seeder used in the research have been briefly discussed and no other options of the mesh generator have been employed.

## 4.2 LBM Solver: Musubi

The LBM solver of the APES packages is Musubi, whose fundamental principles have been discussed in Chapter 3. This section focuses on the Musubi workflow, the relevant Musubi-specific parameters and their implications and significance on the simulations.

Similar to Seeder, Musubi also requires a SIF in which parameters are specified in accordance with a specific table structure. In here, the basics of the simulation are stated such as time-control, property assignation, initial- and boundary conditions, restarts and tracking specifications for post-processing.

Inherent to the nature of LBM solver is the representation of physical parameters through lattice variables or parameters, commonly referred to as lattice parameters. These lattice parameters establish a link to physical parameters via moments computed from microscopic distribution functions. While the discretized nature of lattice parameters ensures numerical stability and accuracy in LBM simulations, it is important to note that they are derived from physical counterparts and carry physical meaning, albeit

in discretized form. The distinction lies primarily in the system of units used. Conversion from physical- to lattice form of significant parameters is discussed shortly.

As with any fluid-mechanical related problem, non-dimensional numbers are essential in understanding the fluid behaviour and characterizing physical phenomena. They play a connecting role in scaling and identifying dominant processes in flows. In general, the associated non-dimensional numbers related to blood flow in arteries are the Reynolds number ( $Re$ ), Mach number ( $Ma$ ), Knudsen number ( $Kn$ ) and Womersley number ( $Wo$ ). The significant numbers for LBM however are the Reynolds number and the Mach number. Manual comparison of the physical- and lattice Reynolds number allows for verification of the correct inputs.

As mentioned in Chapter 3, the relaxation time  $\tau$  and more precisely, its accompanying relaxation frequency  $\omega = \frac{1}{\tau}$ , appearing in the BGK approximation in Equation 3.17, is a vital parameter for tuning the dynamics of a system. It determines the rate at which the distribution function approaches equilibrium during each time-step. The essence of this behaviour in the fluid mechanical realm is found in the viscosity of a system and hence these two are linked. Kinematic viscosity, see Equation 4.3, is related to dynamic viscosity  $\mu$  (resistance to shear stress) and fluid density  $\rho$ . Both of these parameters are often known or approximated for a given system, resulting in a known  $\nu$ .

$$\nu = \frac{\mu}{\rho} \quad (4.3)$$

The relation between the viscosity and relaxation frequency is determined by the Chapman-Enskog expansion, which connects the discrete LB equation to the NSE. The relation, both in relaxation time and -frequency, is given in Equation 4.4, where  $\Delta x$  is the distance-step or lattice spacing and  $\Delta t$  is the time-step.

$$\nu = \frac{(\Delta x)^2}{\Delta t} c_s^2 \left( \tau - \frac{1}{2} \right) = \frac{(\Delta x)^2}{\Delta t} \frac{\left( \frac{1}{\omega} - \frac{1}{2} \right)}{3} \quad (4.4)$$

The distance-step  $\Delta x$  is governed by the mesh size, while the tuning parameter  $\omega$  is set by the user, which leaves the time-step  $\Delta t$  as a result of these choices. The relation between  $\omega$  and  $\Delta t$  can also be elaborated: a higher value for  $\omega$  leads to a lower value for  $\Delta t$ , theoretically allowing for a more accurate simulation due to more frequent updates of the distribution function. However, this can comprise stability, leading to numerical instabilities if  $\omega$  is too high. Conversely, a lower  $\omega$  increases  $\Delta t$ , reducing computational cost and potentially enhancing stability, although at the expense of simulation accuracy. This relation is the result of several factors including relaxation speed to equilibrium (smoothness of adjusting), damping of high frequency modes (suppression of oscillations) and lattice viscosity (introduction of diffusivity). Apart from  $\omega$  tuning, other factors such as grid resolution ( $\Delta x$ ) and overall algorithmic stability also play crucial roles in the accuracy.

The approach taken here is called 'diffusive' scaling, in which  $\nu$  and  $\omega$  are fixed. Alternatively, 'acoustic' scaling is an option in which  $Ma$  is fixed. The difference in approaches lies with the definition of the lattice speed of sound  $c_s$  ( $c_s = \frac{dx}{dt}$  for diffusive scaling). However, acoustic scaling is applicable to compressible flow, hence diffusive scaling is used throughout this research.

The obtained expression for kinematic viscosity is converted to lattice form by non-dimensionalization, leaving it only as a function of  $\omega$ , see Equation 4.5. This limits the possible options for the value of  $\omega$  given the fact that  $\nu_L$  is positive. Plotting Equation 4.5 leads to the graph in Figure 4.3, displaying the domain of values.

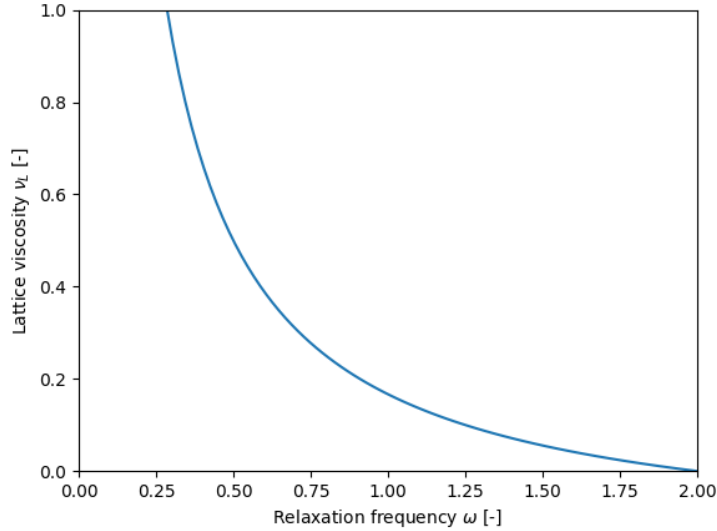


Figure 4.3: Range of values for  $\omega$ .

In practice, a minimal value of 1.5 for  $\omega$  is advised for numerical stability. For lower values, convergence to a steady solution requires an inappropriate amount of time compared to the benefits of the damping properties of high viscosity values.

$$\nu_L = \nu \frac{\Delta t}{(\Delta x)^2} = \frac{\left(\frac{1}{\omega} - \frac{1}{2}\right)}{3} \quad (4.5)$$

Additionally, derivation of  $\nu_L$  also highlights the quadratic relation of the time-step  $\Delta t$  and the distance-step  $\Delta x$ , see Equation 4.6. A finer mesh, with  $\Delta x$  halved, results in a  $\Delta t$  which is a quarter of its original value, amplifying the additional computational resources for more detailed grids. This ratio between  $\Delta t$  and  $\Delta x$  is a consequence of the choice for diffusive scaling.

$$\Delta t = \frac{\nu_L}{\nu} (\Delta x)^2 \quad (4.6)$$

An important parameter is the lattice velocity  $\mathbf{u}_L$ , which is obtained by scaling the macroscopic velocity  $\mathbf{u}$  to the discrete lattice grid. As mentioned previously, diffusive scaling sets the lattice speed of sound  $c_s = \frac{dx}{dt}$ , which leads to the relation as in Equation 4.7

$$\mathbf{u}_L = \frac{\mathbf{u}}{c_s} = \mathbf{u} \frac{dt}{dx} \quad (4.7)$$

As mentioned previously in this Section, the Mach number has an effect on the simulation outcome. A too large  $Ma$  can undermine the assumption of incompressibility and can introduce effects that lead to inaccuracies in the simulation. For incompressible flow like in this research, an upper limit of  $Ma = 0.3$  is usually agreed upon. For  $Ma$  values lower than this, the density of the fluid remains (nearly) constant and the speed of sound is much larger than the flow velocity. For the translation to lattice parameters such as the lattice velocity, a limit can be set to prevent problems regarding compressibility and density fluctuations. A threshold value of  $u_L = 0.15$  is set and exceeding this value at any location at any time-instant causes the simulation to abort.

Musubi gives the option to select a specific relaxation mode for reaching equilibrium distributions for each time-step, with the main ones being 'BGK' and 'MRT'. The BGK mode is named after the group of people who contributed to the BGK approximation, see Section 3.4. It is the simpler of the two modes because a single relaxation time is assumed during each collision. Therefore, it is less computationally expensive at the drawback capturing certain scenarios less accurately. These include non-stationary behaviour of bounceback BC and stability at higher Re, [46] [47]. The MRT mode introduces multiple relaxation times for different moments of the distribution function, making it more flexible at the expense of higher computational cost. It does however provide more stability for complex flow features. MRT does this by locally tuning the relaxation frequency. For this research, the MRT mode is selected for all simulations.

Two different boundary conditions are prescribed in the simulations, an input and output boundary. The input boundary is velocity-driven (Bounceback) and uses a sine-wave as input signal for the velocity at the entrance of the model. Contrarily, at the exit of the model, a prescribed pressure boundary condition (Dirichlet) is employed to dictate a given pressure gradient. The walls of the model utilize a simple first-order accurate bounce-back condition. These are similar for all physical boundaries excluding the entrance and exit. The basics of these boundary conditions have been described in Section 3.7.

This section provides a basic overview of the input parameters, options and model choices relevant to Musubi. The next subsection elaborates on the implementation of particles in the flow simulations.

### 4.2.1 Particles

During the past years, an addition to Musubi has been constructed in order to add a model for particles to simulations. This extension is currently in progress and will be used to study particle behaviour. This section briefly elaborates upon the working principles.

Particle models generally adopt either resolved or unresolved particle representations. In Musubi, individual particle trajectories are tracked for both resolved and unresolved particles. The key distinction lies in how these particles interact with the flow. In simulations involving a relatively small number of particles, the resolved option is typically preferred. This method resolves the detailed flow behaviour between individual particles, which can be computationally intensive. Contrarily, simulations with a large number of particles commonly employ the unresolved approach. This method uses statistical averages to estimate the collective impact of particles without resolving the flow field between them. As a result, this approach is computationally more efficient.

In the implementation of particles in Musubi, particles are two-way coupled, meaning there is a mutual interaction between dispersed particles and the fluid during simulation. This implies that the fluid affects particles, and conversely, particles affect the fluid, forming a coupled feedback loop. Two-way coupling is more computationally expensive compared to one-way or uncoupled systems. However, it offers significant advantages by providing detailed insights into the exact dynamics of individual particles interacting with the fluid. This level of detail is particularly beneficial when a precise understanding of particle-fluid interactions is required, as is the case for large particles. Conversely, one-way coupling can be a good approximation in scenarios where the influence of particles on the fluid can be considered negligible or if computational efficiency is a primary concern. This approach simplifies the simulation by treating particles as passive tracers or sources/sinks without significantly impacting the fluid dynamics. It is often used when the focus is more on the bulk behaviour of the fluid rather than detailed particle-fluid interactions.

Particle collisions are present in the current model, in which momentum transfer is captured. The particles are insusceptible to deformations, mass transfer and the total amount of particles is always conserved. Integration of the equations of motion for the particle dynamics is performed numerous times per single time-step for fluid simulation for accuracy. This separate treatment for particles allows the flow

to be computed at the prescribed temporal resolution, without the need for further refinement of the fluid itself.

The current workflow requires prescribing the initial position, velocity and forces acting upon the particle for each individual particle in the simulation. To ease the manual labour involved here, a script for pseudo-random input values are used for the required number of particles. Due to the nature of parallelization and its preference for specific data structuring, one output file with the dynamical specifications of a single particle throughout the entire simulation is generated for each particle. This requires minimal information transfer between processes and is thus favourable for parallelization. Alternatively, a different approach would be to log every particle’s state per time-step, but this requires significantly more data transfer to establish and is much more computationally expensive.

One might wonder if the particles are passive tracers in the flow. This can be determined by examining the Stokes number  $St$ , which is given in Equation 4.8.

$$St = \frac{\tau_p}{\tau_f} = \frac{2\rho_p U_p R_p}{9\mu_f} \quad (4.8)$$

Where  $\tau_p$  is the relaxation time of the particle and  $\tau_f$  is the characteristic fluid time scale. It is the ratio of a particle’s inertia over the fluid’s viscous effects. Subsequently, this can also be expressed in physical parameters with  $\rho_p$  as the particle density,  $U_p$  as the particle velocity,  $R_p$  as the particle radius and  $\mu_f$  as the fluid’s dynamic viscosity. Equation 4.8 is an empirical relation and is adopted from Gondret et al. [48]. A high Stokes number indicates a dominance of inertia, while a low Stokes number signifies a tendency to follow fluid streamlines, and thus can be labeled as a passive tracer. Stokes numbers between  $10^{-1}$  and  $10^1$  are expected for particles in this research. The Stokes numbers at play determine the choice of the degree of coupling of the particles, as mentioned previously.

Considering the application of radioembolization, certain universal parameters of the particles can be quantified from hereon. In Table 4.2, an overview is given for general particle parameters used for modelling, unless stated otherwise.

| Parameter         | Symbol   | Value | Unit      |
|-------------------|----------|-------|-----------|
| Particle diameter | $D_p$    | 30    | $\mu m$   |
| Particle density  | $\rho_p$ | 1.4   | $gr/cm^3$ |

Table 4.2: Particle parameters.

### 4.3 High performance computing: Snellius

A LB solver like Musubi is inherently suitable for parallelization due to its structured lattice grid. As summarized in Chapter 3, for each lattice point, computations during the collision step are independent of other points, as each point updates based solely on its local neighbourhood and distribution functions. Regardless, during the streaming step, there is interdependence between the lattice points. It involves moving the distribution functions to neighbouring lattice points. However, these dependencies are typically localized and manageable. The structured communication pattern can be leveraged in order to facilitate efficient parallel computation. In other words, it allows a simulation to be split up into different tasks and divided over several computational processes simultaneously. Afterwards, all tasks can easily be ‘stitched’ together to produce a single outcome. In the realm of super-computing, having a multitude of cores is preferred over high core clock speed, which is a measure of the speed of a computer’s arithmetic operations. This is because it provides optimal computational throughput by facilitating scalability,

memory optimization and efficiency across diverse workloads. Additionally, the approach of multiple processes is economically more efficient.

For this research, the National Dutch Supercomputer Snellius has been used for computations. This relatively new supercomputer replaced its predecessor Cartesius in 2021 and is part of the cooperative association of the Dutch educational and research institution SURF. It is named after Dutch scientist Willebrord Snel van Royen, who is most famously known for his law for light refraction, which he derived in 1621. The Snellius cluster operates with a job manager which schedules tasks, delivered via *.sh* files, for reliable operation. These batches are then divided over the requested amount of nodes.

The cluster consists of a collection of four main different node types; 'Thin' nodes, 'fat' nodes, 'GPU' nodes and 'storage' nodes. The thin nodes are numerous but have relatively little memory. There are a total of 504 thin nodes, each node has a total of 128 CPU cores, comprising a total of 64,512 CPU cores. The fat nodes are suitable for memory-intensive processes due to their high RAM capacity. There are a total of 72 nodes with RAM ranging from 1 *TiB* to 8 *TiB*. The GPU nodes speed up certain forms of computations and have a total of performance of 3.0 *Pflops/s*. Finally, the storage nodes provide the required capacity for data storage with a combination of SSDs, HDDs and NVMe memory, resulting in a total available space of around 15 *PB*.

In this research, a maximum of 12 GENOA nodes have been used for computations at once, each containing 192 cores. This brings the total number of cores to 2304, which is acceptably fast and not too demanding on the system load, leading to smaller queue times, if any. The exact number of cores is case-specific in order to find the balance between computational time on one hand and energy consumption and occupying available space on the other hand.

# Chapter 5

## Analysis of turbulence induced particle mixing

### 5.1 Simulation Set-up

This subsection specifies the parameters of the simulation framework for the given geometry, including its spatial and temporal resolutions. The goal of this subsection is to provide a concise overview of the parameters, for transparency and ability to reproduce simulations. This allows further research to verify and build upon findings in this report.

#### 5.1.1 Geometry set-up

In Figure 5.1 a schematic overview of the simulation model is given in 3D. The model consists of four .stl files which, together with one prescribed boundary in Seeder, form an enclosed, airtight model.

| File               | Function                        | Label |
|--------------------|---------------------------------|-------|
| stenosis.stl       | Act as main vessel              | I     |
| catheter.stl       | Hold particles                  | II    |
| stenosis_inlet.stl | Inlet for pulsating flow        | III   |
| catheter_inlet.stl | Inlet for plug flow + particles | IV    |
| stenosis_outlet    | Outlet for flow                 | V     |

Table 5.1: Geometry file-composition.

An overview of the entire geometry of the simulation has now been presented. Individual components of the geometry and the model are elaborated upon in more detail in the coming subsections.

#### Stenosis (I)

A simplified stenosis geometry, as in Figure 5.2, serves as a the basis for the simulation. It is adapted from Jain [49], which in turn has studied this geometry from Varghese et al. [50]. The simplicity of the stenosis as given, contributed to its adaptability and has since been studied extensively.

Two different set-ups are distinguishable, each preserving the curvature of the stenosis, namely an axisymmetric case and an eccentric case. Both cases are identical, apart from the offset of the axis of stenosis from the main vessel axis by a factor of  $0.05D$ . The eccentric case is given priority in the analysis, given its expected earlier onset of turbulence due to this slight disturbance.

The eccentric case is captured in geometric formulation, as given in Equation 5.1.

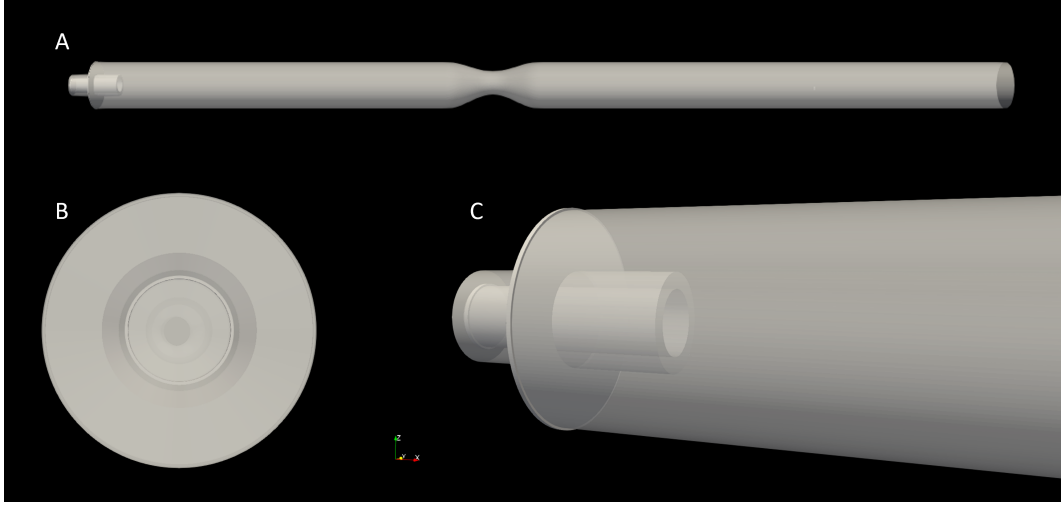


Figure 5.1: 3D images of the model; A) Full model; B) Radial view; C) Catheter closeup.

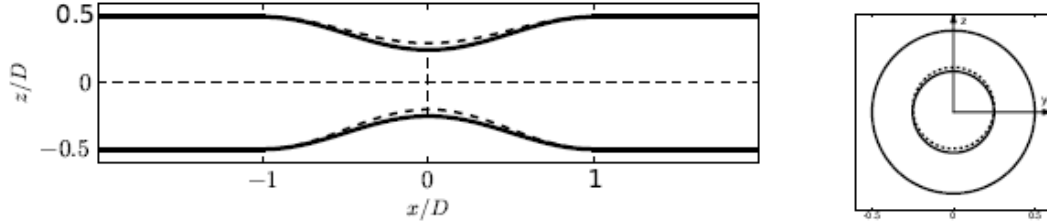


Figure 5.2: Schematic overview of the stenosis in a lengthwise cross-section and an area cross-section. The bold line represents the axisymmetric boundaries of the vessel, the dashed straight line the vessel centerline and the dashed curved lines the eccentric case.

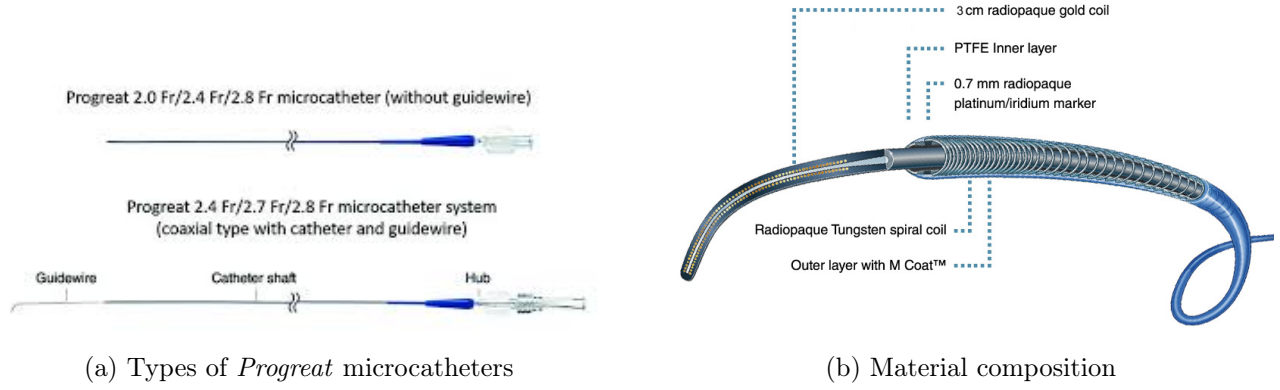
$$\left. \begin{aligned} S(x) &= \frac{1}{2}D [1 - s_0 (1 + \cos(2\pi(x - x_0)/L))] \\ E(x) &= \frac{1}{10}s_0 (1 + \cos(2\pi(x - x_0)/L)), \\ y &= S(x) \cos \theta, \quad z = E(x) + S(x) \sin \theta \end{aligned} \right\} \quad (5.1)$$

Here,  $x$  is the axial coordinate along the vessel diameter. Cross-stream coordinates  $y$  and  $z$  are computed via the function(s)  $S(x)$  and  $E(x)$ .  $D$  is the diameter of the non-stenosed pipe.  $L$  is the length of the stenosis ( $L = 2D$ ).  $x_0$  is the location of the center of the stenosis and  $s_0$  is a constant for the stenosis size ( $s_0 = 0.25$ ). The stenosis throat has a maximum diameter of  $0.5D$ , leading to a total area reduction of  $1 - 0.5^2 = 75\%$  in the throat. The conservation equation of mass indicates that for incompressible flows, the velocity in the stenosis throat will increase by a factor of 4.

## Catheter (II)

The catheter from which particles are released in the stenosis is included in the geometry. It is modelled after a *Progreat 2.7Fr microcatheter*, manufactured by *Terumo Interventional Systems*. The catheter consists of a PTFE inner layer, on which a tungsten spiral coil resides. The catheter is coated with hydrophilic coating *M Coat*, creating a flexible wire suitable for navigating tortuous and narrow blood vessels. The *2.7Fr* variant is frequently used in radioembolization procedures, see Figure 5.3.

The modelled catheter is effectively a rigid, hollow cylindrical shape, with an inner diameter of  $0.6 \text{ mm}$

Figure 5.3: Progreate<sup>TM</sup> [7].

and an outer diameter of  $0.9 \text{ mm}$ , with a constant wall thickness of  $0.15 \text{ mm}$ . The catheter is placed axisymmetrically along the stream-wise axis, with a distance from tip to throat of the stenosis of  $16 \text{ mm}$ . This distance is found to be acceptable for the development of the flow pre-stenosis. The catheter is reduced to only its front  $2 \text{ mm}$ , where the particles will reside and be released from. This choice is made in order to reduce the total geometry and thus computational time, in combination with the ability to prescribe the flow and particles inside the catheter separately. The discrepancy between the flexible nature of the *Progreate 2.7Fr microcatheter* and the rigid modelled catheter is explained by the short axial distance modelled, combined with the physical model used in UT experiments, which is a rigid stainless steel tube. Note that the optimal catheter position, orientation, geometry and material is a study on its own, with the University of Twente actively performing research on in-vitro experiments and simulations regarding catheter influence [28].

### Boundary conditions (III, IV & V)

To finalize the geometry, the different boundary conditions (BCs) are discussed. A total of four BCs are present in the model. The vessel containing the stenosis has a simple velocity bounceback BC, with the no-slip conditions, acting as a wall for the fluid. The inlet for the flow is split into two sections: stenosis and catheter. The stenosis inlet is a velocity bounceback BC, with a prescribed velocity for the pulsating flow, which is further discussed in Subsection 5.1.3. The catheter inlet possesses the same BC type but has a plug flow profile as input. The outlet of the vessel is determined by a pressure BC, for which the pressure of the outflowing fluid can easily be described. This pressure is set via the following Equation

$$P = \frac{\rho_{phy}}{3} \frac{dx^2}{dt^2} \quad (5.2)$$

### 5.1.2 Mesh

Once the geometry is determined and the total model is found to be applicable (airtight, no geometric unwanted shapes, etc.), a mesh can be generated via Seeder. See Section 4.1 for solver specifics and details.

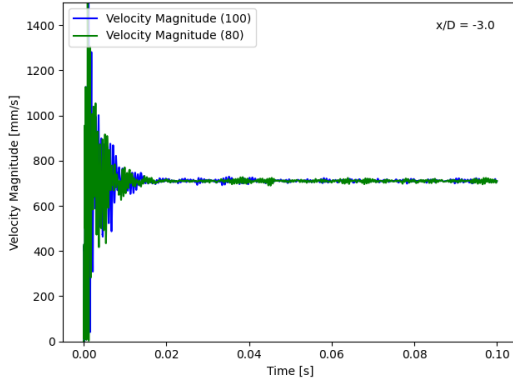
As stated previously, the lattice velocity  $\mathbf{u}_L$  can not exceed 0.15 due to compressibility limits and is directly coupled to the physical flow velocity and the distance step  $dx$  and time step  $dt$ . Given that the physical flow velocity is set in stone for a certain Reynolds number, the only feasible way to decrease the lattice velocity is to decrease  $dx$  and fine tune this parameter to an acceptable value for  $\mathbf{u}_L$ , which is close to the threshold-value of 0.15, but leaves a small margin for any instabilities in the simulation that might occur. Furthermore, increasing the number of lattice elements will reduce the numerical error term at the cost of computational expenses. These considerations lead to a distinction of mesh resolutions for different

flowcases, which are classified as I, II and III, see Table 5.2.

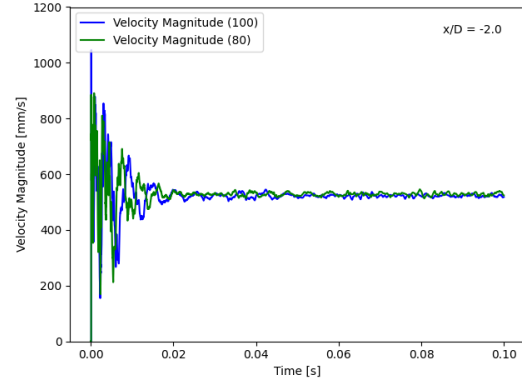
| Class | $dx$ (mm)            | $dt$ (s)             | Total (NoE)               | Level | time to mesh      |
|-------|----------------------|----------------------|---------------------------|-------|-------------------|
| I     | $320 \times 10^{-4}$ | $4.5 \times 10^{-6}$ | $\approx 3.4 \times 10^6$ | 11    | $\approx 10$ sec. |
| II    | $160 \times 10^{-4}$ | $1.1 \times 10^{-6}$ | $\approx 28 \times 10^6$  | 12    | $\approx 1$ min.  |
| III   | $100 \times 10^{-4}$ | $4.4 \times 10^{-7}$ | $\approx 115 \times 10^6$ | 13    | $\approx 5$ min.  |

Table 5.2: Mesh resolutions.

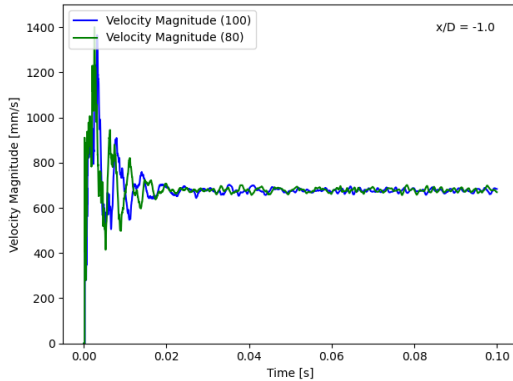
These resolutions provide the framework for flow simulations based on the Reynolds number. However, caution is advised to simply proceed with these meshes. A mesh convergence study has to be performed to determine the applicability of the mesh. The convergence of the simulation has to be demonstrated for the chosen distance-step. Ideally, the convergence of a signal in a model is tested for increasingly smaller  $dx$ , up to the resolution which exhibits acceptable differences to its predecessor. Given previous research by Jain [49], which verified the current resolution for similar simulations, an alternative approach is proposed. For this research, the high resolution mesh ( $dx = 0.01mm$ ), gathered from Jain, is compared to an even finer mesh ( $dx = 0.008mm$ ). For sake of computational resources, a shortened version of the model is used in the mesh convergence study. Moreover, the study is solely flow-based and no particles are introduced in the simulation.



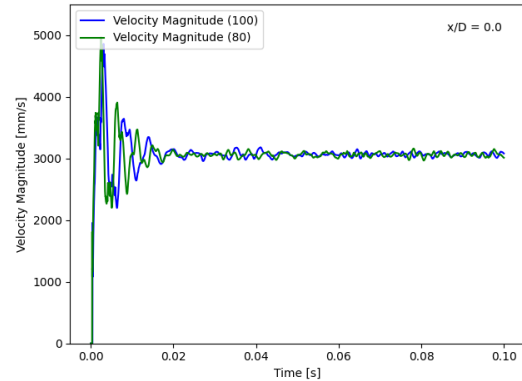
(a) Comparison velocity signal at  $x/D = -3.0$



(b) Comparison velocity signal at  $x/D = -2.0$



(c) Comparison velocity signal at  $x/D = -1.0$

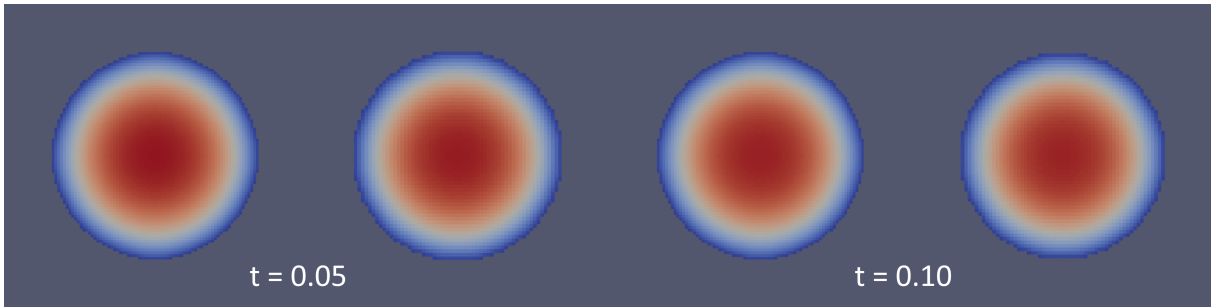


(d) Comparison velocity signal at  $x/D = 0.0$

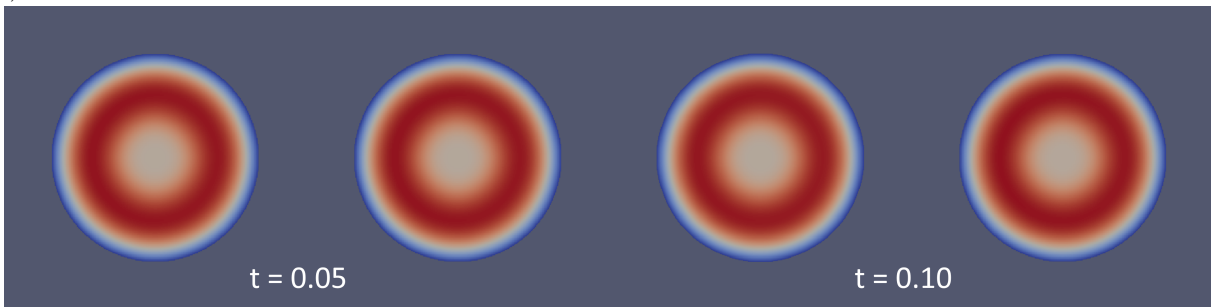
Figure 5.4: Centerline probes pre-stenosis at various locations.

For the mesh convergence study, a constant velocity is imposed at the entrance of the model. It takes a few milliseconds for the initial conditions to wash away and all fluid-related parameters are expected to

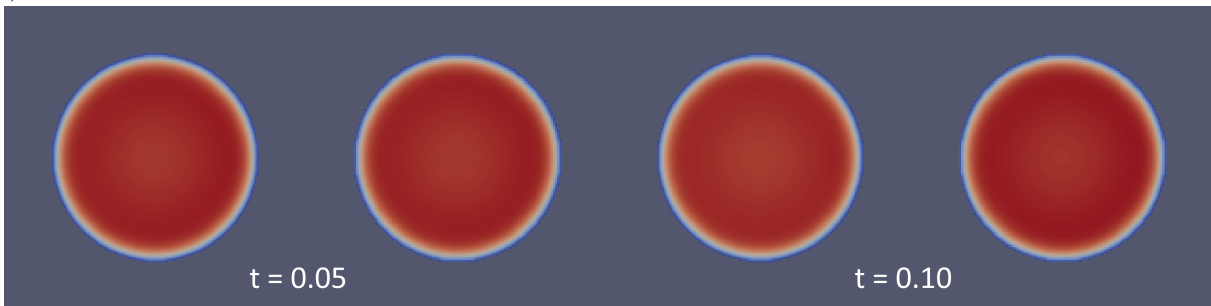
oscillate and subsequently converge to the imposed velocity value or an equivalent value based on local geometry. Figure 5.4 shows the centerline velocity at 4 distinct locations for both meshes. The first two centiseconds are required for the major oscillations to die out. Ideally, a constant signal should be measured, which reassures that the simulation has converged to the steady input. The slight fluctuations present in the plots are attributed to the mixing of flows of the catheter and main entrance. The strength and frequency of the small fluctuations do not differ between the two meshes. The additional detail and high resolution the finer mesh offers do not improve the simulations results. Hence, it is determined that the solution has sufficiently converged for the coarse mesh.



(a) Cross-section at  $x/D = 3.0$ ; 2 snapshots at  $t = 0.05$  and  $t = 0.10$  for  $dx = 0.008mm$  (left) and  $dx = 0.01mm$  (right).



(b) Cross-section at  $x/D = 1.5$ ; 2 snapshots at  $t = 0.05$  and  $t = 0.10$  for  $dx = 0.008mm$  (left) and  $dx = 0.01mm$  (right).



(c) Cross-section at  $x/D = 0.0$ ; 2 snapshots at  $t = 0.05$  and  $t = 0.10$  for  $dx = 0.008mm$  (left) and  $dx = 0.01mm$  (right).

Figure 5.5: Comparison of cross-sections of the model regarding the mesh convergence study.

To further visualize the convergence, several snapshots of the cross-sectional area of the model are compared for both meshes at similar time instances. This can be observed in Figure 5.5. Even though the images are merely visually inspected, no distinct differences can be observed and numerical comparison for the cross-sectional area is not found to be required. This concludes the mesh convergence study. Now that the resolution of the mesh is determined, the next focus is on the flow inside the model.

### 5.1.3 Flow conditions

Table 5.3 contains the properties of the fluid which are uniformly used throughout the simulations in this research. These properties for density and viscosity are frequently used to model blood as a Newtonian fluid and follow from Jain [49]. Hence, the non-Newtonian behaviour of blood is not accounted for. It should be noted that in LBM, modifications to the collision operator can compensate for this non-linearity. However, this requires extensive study about the rheology of blood and comparison with experimental results, which are simply not implemented in this study. The selected relaxation frequency of 1.84 provides the desired trade-off between numerical stability and computational speed.

| Property             | Symbol   | Value                  | Unit      |
|----------------------|----------|------------------------|-----------|
| Density              | $\rho$   | $1.056 \times 10^{-6}$ | $kg/mm^3$ |
| Dynamic viscosity    | $\mu$    | $3.450 \times 10^{-6}$ | $kg/mm/s$ |
| Relaxation frequency | $\omega$ | 1.84                   | -         |

Table 5.3: Inherent flow properties of fluid in simulation.

As mentioned in Section 2.2, blood is not a homogeneous fluid and therefore consists of several components. Out of the physical cellular constituents, red blood cells are the most profound and numerous, with average volume fractions of 35% to 52%. White blood cells and platelets are found in much smaller concentrations. Typical diameters for red blood cells range from  $6 - 8 \mu m$ , which is comparable to the order of magnitude for particles. Similarly for the density, red blood cells possess slightly lower, but comparable density. This introduces an important unmodelled factor in the system. It is inevitable that there is interaction between the microsphere particles and the red blood cells, which is not accounted for in the model.

The main flow through the vessel originates from the inlet of the stenosis (III), This flow possesses a periodic pulsating nature, which is modelled after a simple heartbeat, the driving force of blood circulation in the human body and consequently in the hepatic artery. In Figure 5.6, the input of the flow is displayed.

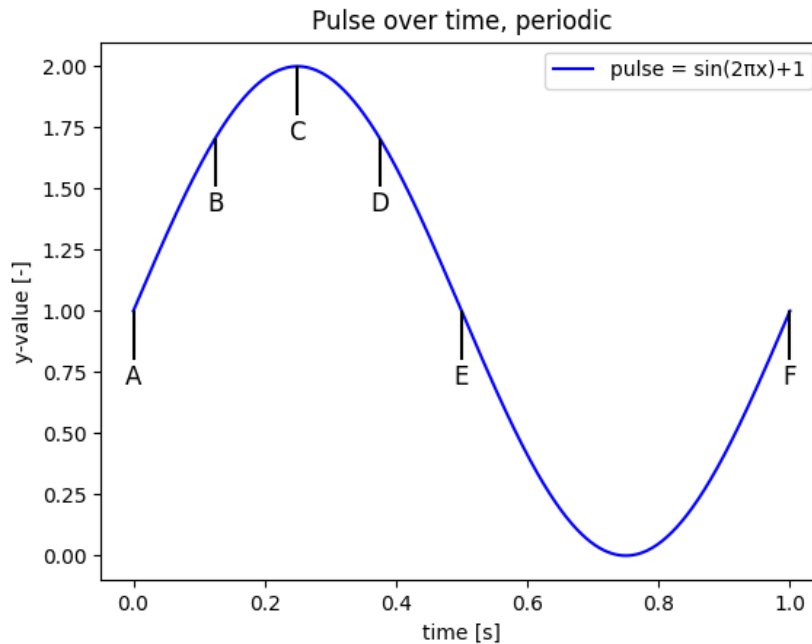


Figure 5.6: Input pulse for the flow.

The pulse is described by a simple sinewave ( $\sin(2\pi x) + 1$ ). This pulse is chosen for its simplicity

and is scaled to a period of 1 second, leading to a heartrate of 60 BPM. This is found to be a proper approximation for a person at rest in the supine position. Note that the y-value is simply a constant, which is multiplied by the required flow velocity for the simulation. This implies that at  $t = \frac{1}{4}s$ , the flow velocity is maximum and at  $t = \frac{3}{4}s$ , the flow velocity is minimum and equal to zero.

In Table 5.4, the most frequently used time instances to characterize injection points during the pulse, are labelled.

| Instant (time ) | Name          | Label | Symbol  |
|-----------------|---------------|-------|---|
| $t = 0.000$ s   | Start         | A     |  |
| $t = 0.125$ s   | Acceleration  | B     |  |
| $t = 0.250$ s   | Peak systole  | C     |  |
| $t = 0.375$ s   | Deceleration  | D     |  |
| $t = 0.500$ s   | Halfway point | E     |  |
| $t = 1.000$ s   | End           | F     |  |

Table 5.4: Labelled time instances in pulse.

These include the starting point (A) and the endpoint (F) which are connected via the periodicity of the pulse. During the peak systole value (C), the flow velocity is maximum, which will introduce the highest lattice velocities in the model. The maximum positive gradient of the flow corresponds with the highest acceleration of the fluid (B), while the maximum deceleration of the flow (D) is expected to exhibit the most influential changes to the flow. Even without simulation results, this can be explained by the fact that during deceleration, the flow velocity decreases and consequently the pressure increases. This creates an adverse pressure gradient in the flow, triggers the onset of instabilities and introduces flow separation. To conclude, the halfway point (E) is also labelled.

In Table 5.5, the flowclasses are assigned flow velocities and corresponding Reynolds numbers. Since assigning  $Re$  to flow can be somewhat arbitrary, a clear definition of the flow is given here: The Reynolds number of the flow is based on the maximum flow velocity of the velocity profile at  $x = -2.5$  ( $0.5mm$  pre-stenosis), during the maximum inflow velocity at time-instant C ( $t = 0.25s$ ).

| Class | Re [-] | $\approx u_{max}[mm/s]$ | Physical representation in hepatic artery |
|-------|--------|-------------------------|---|
| I     | 160    | 259                     | Lowerbound of flow regime                 |
| II    | 450    | 735                     | Common value for flow regime              |
| III   | 700    | 1147                    | Upperbound of flow regime                 |

Table 5.5: Flowclasses.

Due to the location of the catheter on the centerline, cutting through the inlet of the vessel, the cross-sectional area of the inlet represents an annulus with inner radius  $r_i$  and outer radius  $r_o$ . An analytical solution exists for such a flow profile [51]. However, prescribing a specific velocity profile in Musubi is difficult and can be omitted by another solution. Given enough entrance length, the flow can simply develop from a plug flow into the required profile. This option is also chosen in the simulation, and will be discussed per flow case separately.

The flow in the catheter, excluding particles, is much simpler compared to the flow outside the catheter.

It is simply a constant value that corresponds to the average velocity of the flow in the simulation, such as a constant  $y$ -value of 1 in Figure 5.6. Given that the catheter-inlet is not connected to the hepatic artery and that the catheter is ejected at a constant rate during procedure, this assumption came to be.

Regarding the initial conditions, the pressure inside the entire domain of the vessel at the start of the simulation ( $t = 0s$ ) is set equal to the previously mentioned outlet pressure at the BC. This way, no explicit pressure gradient is created and the flow is purely velocity-driven. Additionally, the flow velocity inside the vessel is set to zero in all spatial directions to ensure uniform starting conditions.

Due to the above-mentioned initial conditions, the flow at the very beginning of the simulation still has to develop and might not represent a continuous flow of blood throughout the model. It possesses numerical artifacts which persist and affect fluid dynamics. Additionally, intervals of interest for this study are located early on in the pulse and might still exhibit this transient behaviour.

Combining these two considerations, a decision is made to first simulate a full second of flow only and using the state of the simulation at  $t = 1s$ , as the starting point. In Musubi, this is known as a restart, which captures a snapshot of the flow in the entire domain and saves it as an input or further simulations. The main advantage here is to (partially) eliminate disturbances in the flow due to initial conditions, which approximates the flow more accurately. It basically 'washes' away any physically unwanted behaviour. Drawbacks are the increased simulation time; A restart has to be generated for each and every geometry and flow condition, which increases total computational time. Therefore,  $t = 1s$  has been chosen as a minimal value, one full cycle of pulsating flow.

In the ideal world, where money and time are no issues, the restart is captured as  $t \rightarrow \infty$ . However, it should be noted that the drawback of an extended restart simply outweighs the increased computational cost and no significant added accuracy will be obtained compared to shorter approximations.

#### 5.1.4 Particles

As stated in Section 4.2.1, Table 4.2 contains the inherent properties of the particles in the simulation, which is repeated here for sake of overview.

| Parameter         | Symbol   | Value | Unit     |
|-------------------|----------|-------|----------|
| Particle diameter | $D_p$    | 30    | $\mu m$  |
| Particle density  | $\rho_p$ | 1.4   | $g/cm^3$ |

Table 5.6: Particle parameters.

For every simulation, the particles are released in exactly similar fashion. First of all, the particles are confined to a predefined area, which coincides exactly with the inside of the catheter. This ensures that the particles are always contained in the exact location corresponding to the bounds of the model. A choice has to be made regarding particle distribution; A Gaussian distribution model or a uniform particle model. The former might be closer to reality but the latter gives more control over the particles and allows for more standardized comparison. The Gaussian distribution samples a number of points  $N$  randomly inside the distribution, generating a pseudo-random grid of particles. The procedure for a Gaussian distribution is as follows: Particles are centered around  $y = z = 0$ , leading to a value for the location of the distribution  $\mu = \{0, 0\}$ , and ensuring axisymmetric distribution. The other tuning parameter,  $\sigma$ , dictates the standard deviation in spatial directions. This value is set to  $\sigma = \{0.1, 0.1\}$ . A uniform distribution is more straightforward. An axisymmetrical grid of particles is generated inside the catheter, ensuring that the Center of Gravity (C.o.G.) of the distribution lies at  $y = z = 0$ . This ensures a uniform starting distribution in the two spatial directions  $y$  and  $z$ .

The Probability Density Functions (PDFs) are displayed in Figure 5.7. A single 'slice' of the catheter is highlighted in Figure 5.8. Note that the distribution in use is 3D and consists of a number of slices,

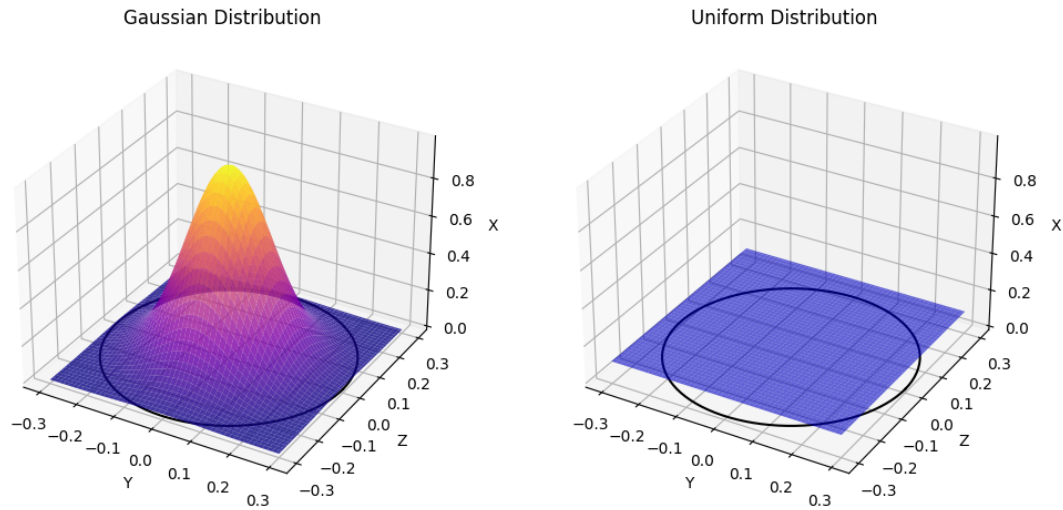


Figure 5.7: Gaussian vs Uniform particle distribution in 3D.

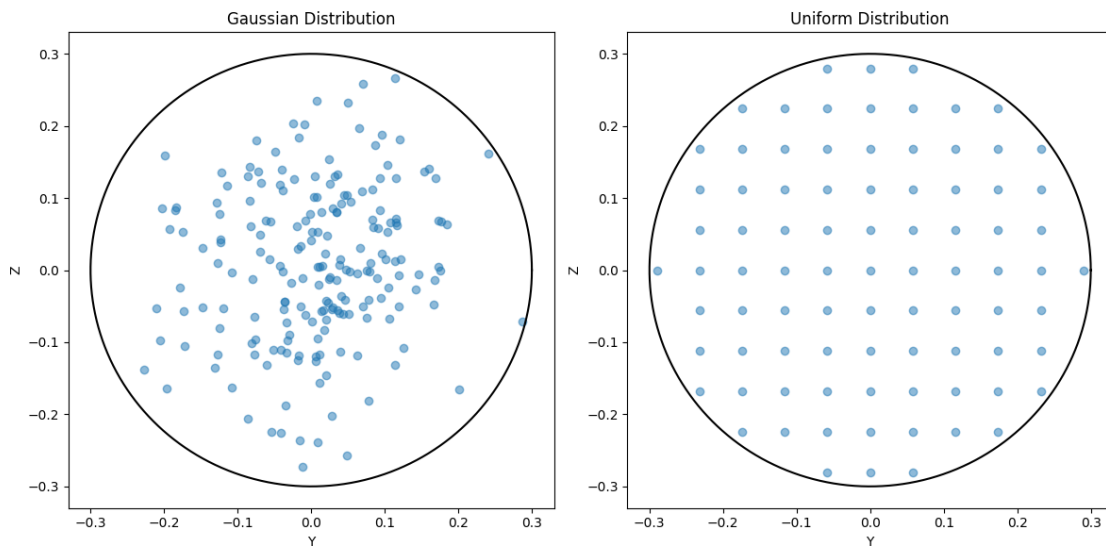


Figure 5.8: Gaussian vs Uniform particle distribution in 2D.

making up the inside of the model catheter. The number of particles is set to 979, to ensure axisymmetry. A target of 1000 particles was established beforehand, compromising computational speed and accuracy. In radioembolization procedures, a typical volume-fraction of the holmium microspheres is in the order of magnitude of 1% [52]. The initial distribution which is used in all simulations is displayed in Figure 5.9.

Now that the distribution is initialized, the simulation can proceed. Simultaneously, the particles are released at one specific time instant, releasing them all at the same time step  $dt$ . Instantaneously, all particles adopt their local flow velocity and start to move with the surrounding fluid. There are no externally specified forces acting upon the particles such as gravity. Prescribing a gradual acceleration, or random initial velocities, mimicking particles in a suspension is out of the scope of this research. The

## Uniform particles distribution (Total: 979)

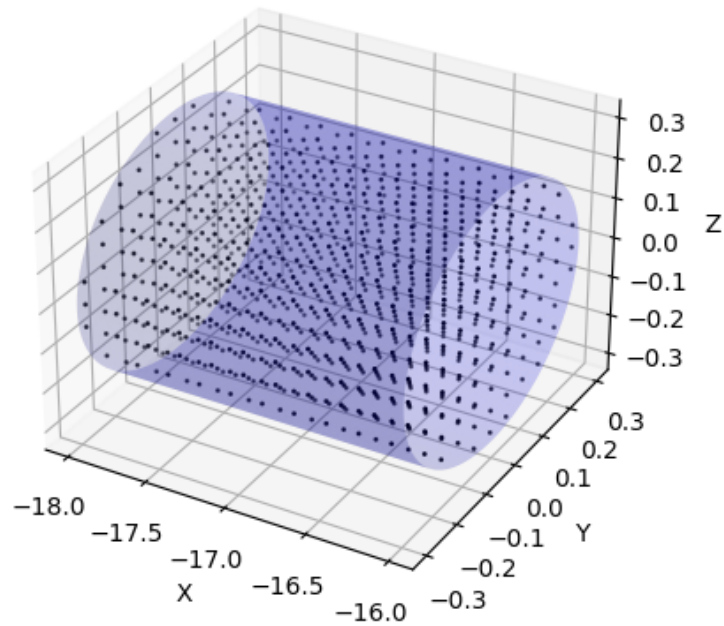


Figure 5.9: Initial particle distribution.

implementation of a 'release-interval' instead of an instantaneous time-step has been considered, but has been ignored given its limited added value.

With this subsection, the basis of the simulation framework has been completed and discussed. From hereon, each individual simulation is addressed in detail and its results are elaborated upon.

## 5.2 Analysis of flow

Prior to particle analysis, the flow itself, without any introduction of particles is addressed. This allows for a basis and future comparisons between flow-only and flow-containing particles. As stated in Section 5.1.2, three flow classes are derived to distinguish different types of flow. These are not chosen arbitrarily but rather coincide with distinct flowcases inside the hepatic artery. This Section elaborates on the flow profile of each of these classes. For every flowcase, the Reynolds number is the main characteristic of the flow.

Again, the Reynolds number of a flow is conventionally based on the maximum flow velocity, which occurs at the centerline in an axisymmetric pipe, inducing a parabolic velocity profile dome. A sufficient entrance length, see Equation 5.3 allows the flow enough distance to develop a steady velocity profile before entering the stenosed part of the model. This is important since it provides similarity between the different flowcases.

$$L_{h,lam} = 0.0575ReD \quad (5.3)$$

Additionally, it is important to capture all the turbulent activity post-stenosis. Ignoring turbulent effects might exclude parts of area for mixing. Contrarily, a margin which is too spacious only adds to the computational time. Research by Jain [49] has shown that for an additional length of  $L_{post,sten} = 10D$  is sufficient and applicable for the Reynolds numbers in play.

The following sections discusses the three different flow classes. A range of visualization plots are used to analyse the flow. Pressure and density maps are not included, since the incompressibility of the simulations is not in jeopardy. The main area of focus is the post-stenosis part, which is the second half of the stenosed pipe. This part represents the hepatic artery in which turbulent flow might occur. The part before the stenosis is used to develop the flow from the catheter and main vessel. The stenosis throat contains the highest flow velocities and generates a jet of flow exiting the throat. The jet is not a naturally occurring flow phenomenon in the hepatic artery. It is the result of the eccentric throat geometry, which induces turbulence. Therefore, the last section of the post-stenosis part represents the flow in the hepatic artery.

### Flow class I: $Re = 160$

Figure 5.10 shows velocity magnitude across a bisecting plane in the stenosis at various time instances. Note that this is the absolute velocity magnitude, containing all three spatial directions. Observing the plot yields the conclusion that the flow shows laminar behaviour. The deflection in positive y-direction of the main jet post-stenosis is clearly visible. The flow does not exhibit any indications of turbulence at the current flow velocity. The imposed flow velocity at the left boundary travels quickly through the model and the maximum flow velocity is observed in the throat of the stenosis, at the centerline. The streamlines are evenly spaced, see Figure 5.11. This plot shows a uniform spaced grid showing the flow direction, near the throat section. Note that the arrows are not scaled to the velocity magnitude. Little to no rotation is observed in the flow, see 5.12, which shows the vorticity in the flow. Vorticity is defined as the curl of the velocity field ( $\boldsymbol{\omega} = \nabla \times \boldsymbol{\xi}$ ) and represents the tendency of a continuum to rotate. There is flow re-circulation post-stenosis, in which the flow travels backwards parallel to the bulk flow of the jet. This can be observed in the direction of the arrows in Figure 5.11. The maximum re-circulation velocity occurs close to the stenosis throat and its magnitude is around 10% of the maximum velocity in the simulation. The pressure and accompanying density plots of the simulation show behaviour corresponding to incompressible flow, with little variation in magnitude across the flow profile, leading to a stable simulation. Figure 5.13 displays the developing profile of the flow front at an instantaneous time-instant. The values are absolute and only contain the  $x$ -component of the velocity, parallel to the centerline. Point C, peak systole has been selected for this visualization, given the occurrence of extremes around this point. The front develops

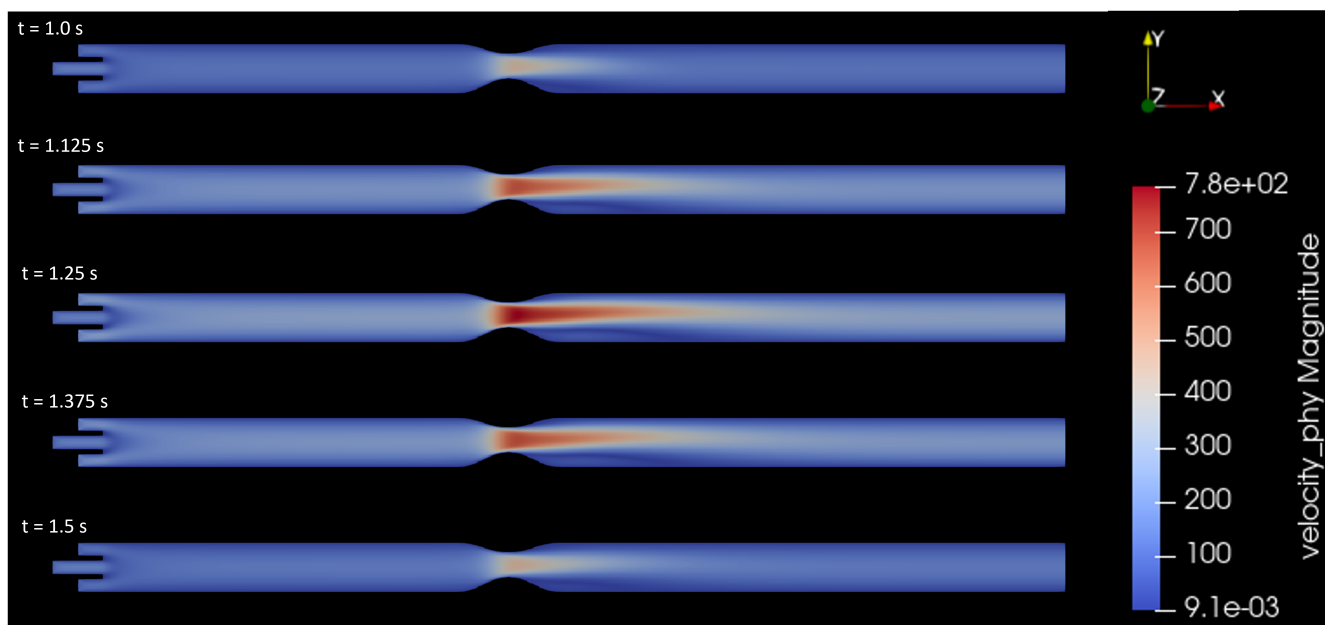


Figure 5.10: 2D Longitudinal cross-section plots of velocity field for class I.

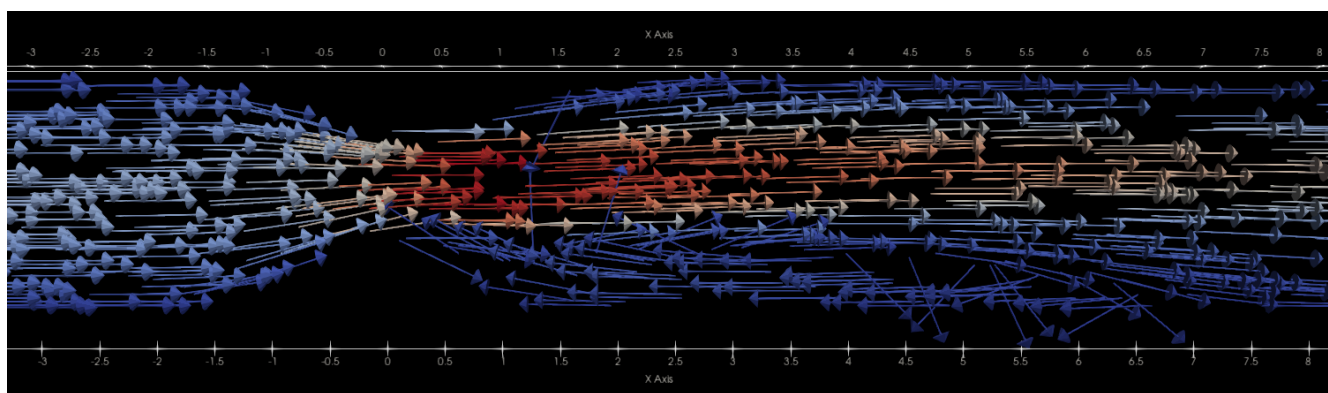


Figure 5.11: 2D Longitudinal cross-section plots of flow direction for class I at  $t = 1.250$  s  $\curvearrowright$ .

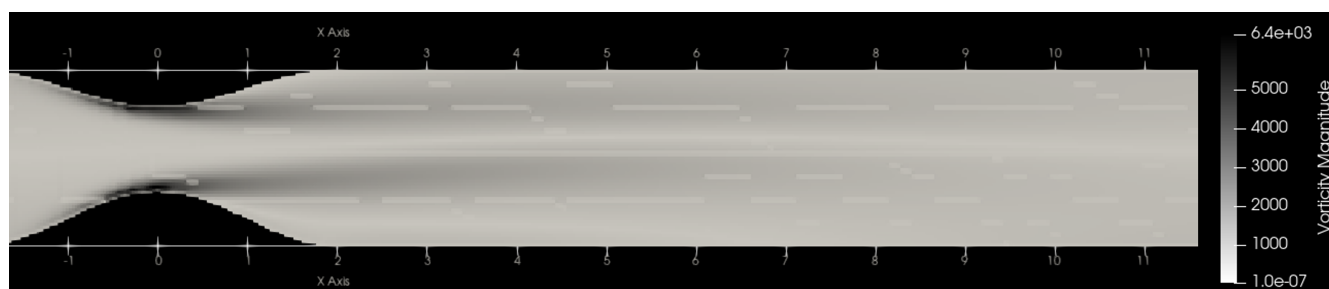


Figure 5.12: 2D Longitudinal cross-section plots of vorticity for class I at  $t = 1.250$  s  $\curvearrowright$ .

quickly to a Poiseuille profile pre-stenosis and adjusts to that same profile post-stenosis inside the vessel's spatial bounds.

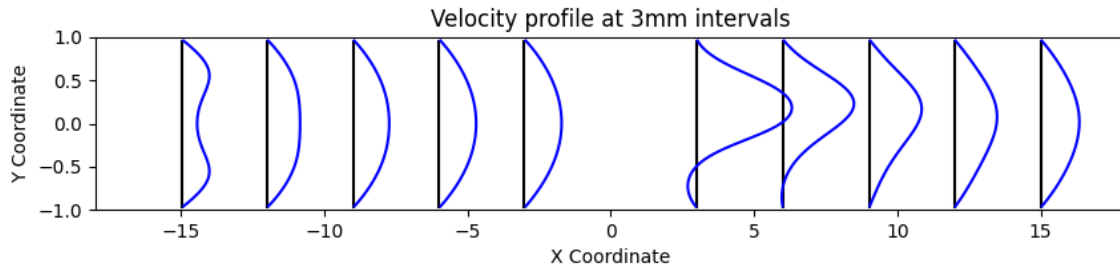


Figure 5.13: Flow-profile for class I at  $t = 1.250$  s  $\curvearrowright$ .

### Flow class II: $Re = 450$

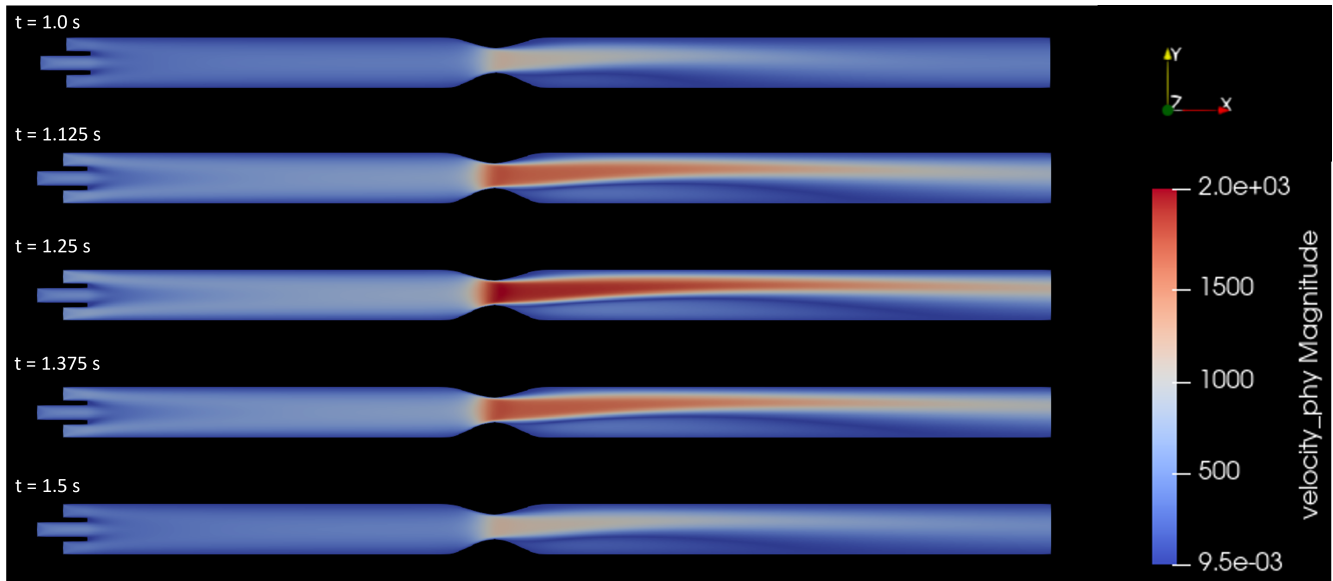


Figure 5.14: 2D Longitudinal cross-section plots of velocity field for class II.

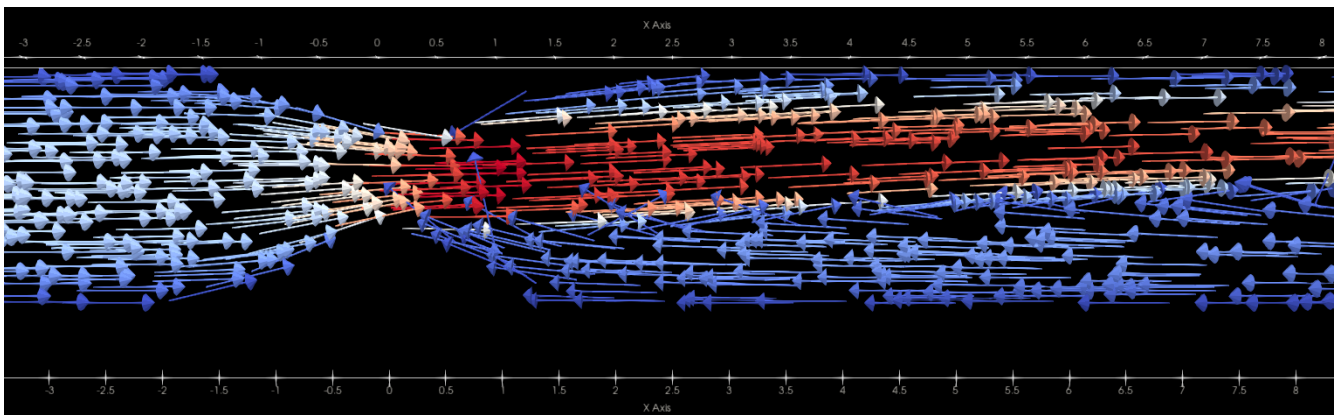


Figure 5.15: 2D Longitudinal cross-section plots of flow direction for class II at  $t = 1.250$  s  $\curvearrowright$ .

Similarly for flow case II, the velocity profile is shown for the first half of a second after the restart in Figure 5.14. The layout of the plots show similar structure to Figure 5.10 in terms of flow velocity magnitude. The deflection of the jet exiting the stenosis throat is even more visible and the angle of deflection is larger as well. The maximum velocity magnitude is increased threefold, which corresponds to the expected results regarding the Reynolds number increase. In the current configuration, the jet does

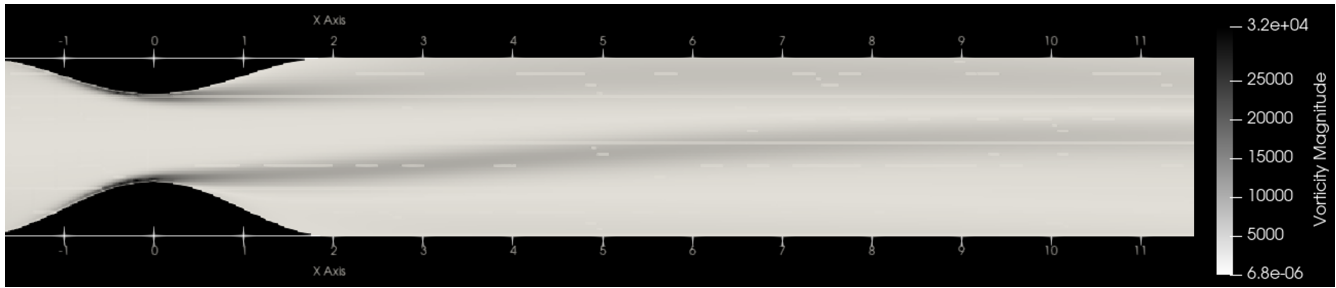


Figure 5.16: 2D Longitudinal cross-section plots of vorticity for class II at  $t = 1.20 \text{ s}$ .

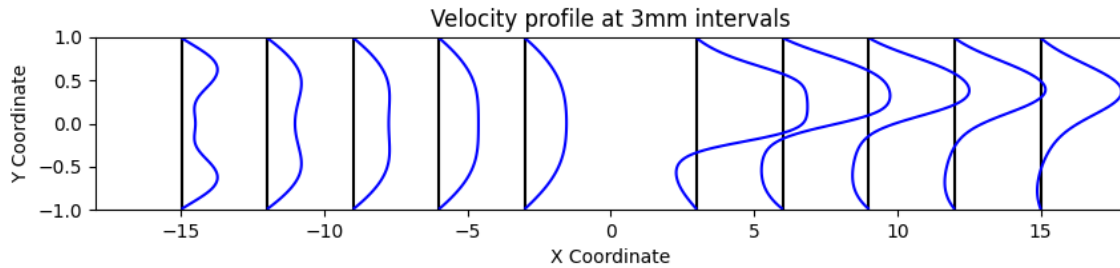


Figure 5.17: Flow-profile for class II at  $t = 1.250 \text{ s}$ .

not collapse and the streamlines remain parallel to each other. The re-circulation of the flow underneath the jet increases compared to flow case I, with velocities up to 20% of the maximum velocity. In Figure 5.15 it can be observed that the flow reversal occurs further downstream compared to flow case I, e.g. the flow direction in-frame is all uni-directional for the bottom half of the vessel post-stenosis. The interface between the jet and reversed flow is can become a shear layer, which can contribute to turbulent characteristics. However, the transition of the flow direction is rather smooth across the interface. Vorticity plot in Figure 5.16 correlates with the velocity profile, in which the contour of the jet is clearly visible again. The magnitude increases five-fold compared to flowcase I, but the flow can still be classified as laminar flow. The developing flow profile however, see Figure 5.17, is clearly different than for flowcase I. The flow requires a larger distance to transform into Poiseuille flow pre-stenosis and the velocity increase in the throat propagates throughout the entire post-stenosis length of the model. The velocity profile remains skewed up to the end of the model. It is decided not to elongate the model to encompass this transition to a symmetric flow profile in the context of this thesis.

Similarly to flow case I, streamlines are parallel, no significant indicators of turbulent behaviour can be observed in the flow.

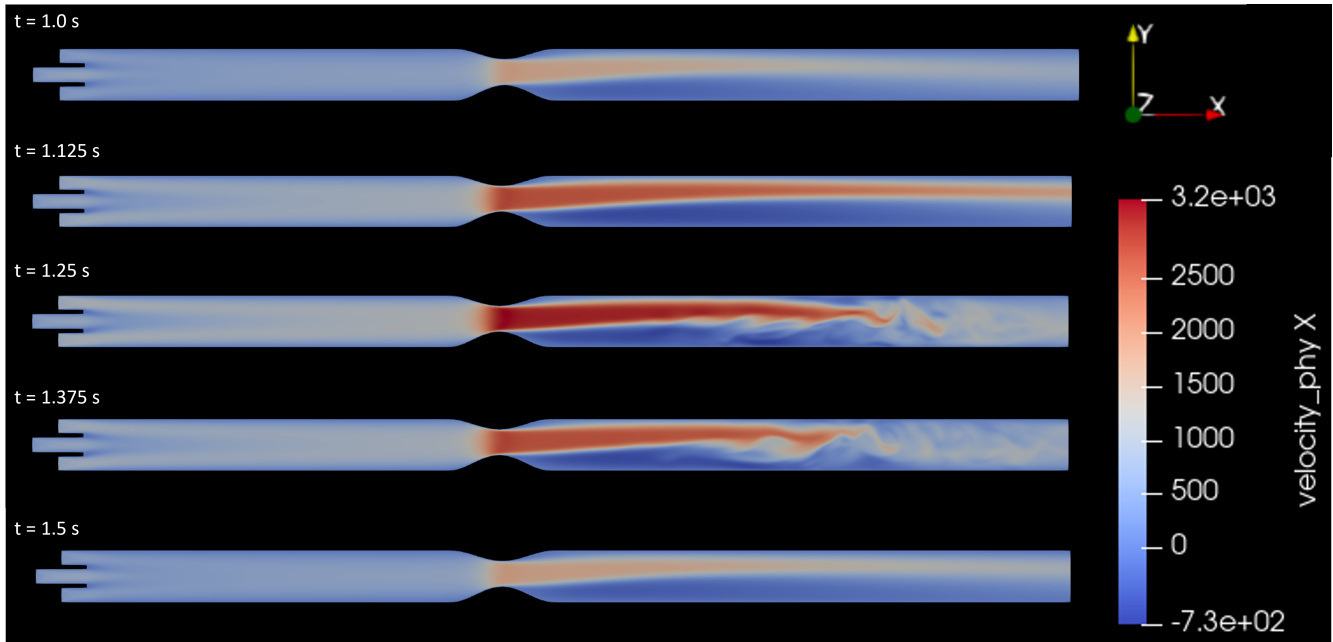
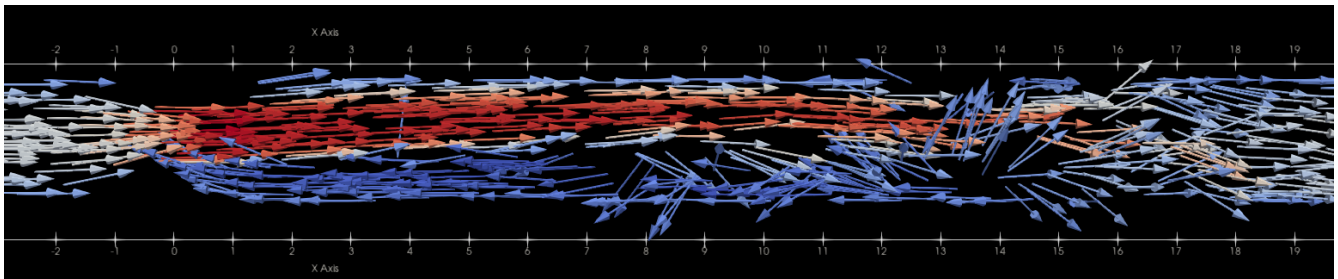
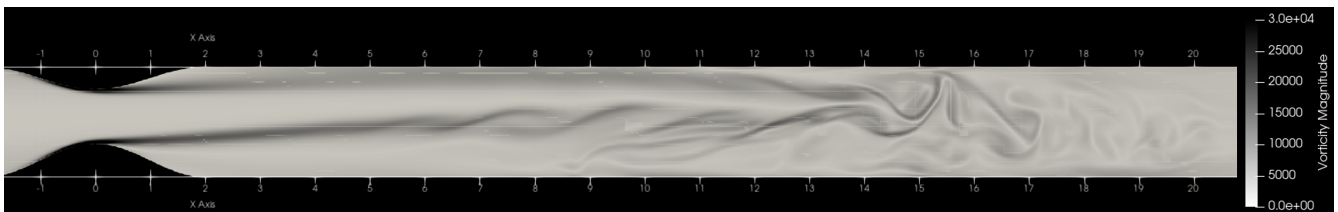
Flow class III:  $Re = 700$ 

Figure 5.18: 2D Longitudinal cross-section plots of velocity field for class III.

Figure 5.19: 2D Longitudinal cross-section plots of flow direction for class III at  $t = 1.250$  s  $\curvearrowright$ .Figure 5.20: 2D Longitudinal cross-section plots of vorticity for class III at  $t = 1.250$  s  $\curvearrowright$ .

Flowclass III finalizes the flow analysis. In Figure 5.18, the familiar 5 plots of the first half a second are displayed again. The flow velocity is significantly higher compared to classes I and II. The jet exiting the stenosis throat breaks down in between  $t = 1.125s$  and  $t = 1.250s$ . This period of deceleration of the cardiac cycle induces the first turbulent activity in the flow, thus far. The flow velocity becomes too large to sustain and the jet breaks down in random swirling rotational motion. The shear interface between the jet and the surrounding fluid induces great perpendicular velocity gradients. In Figure 5.20, the vorticity manifests along the centerline of the stenosis and different size vortices can be distinguished. Note that this plot is merely a snapshot in time and that the vortices are characterized by randomness, meaning that the local flow-field rapidly changes. It is also important to note that between  $t = 1.375s$  and  $t = 1.500s$ ,

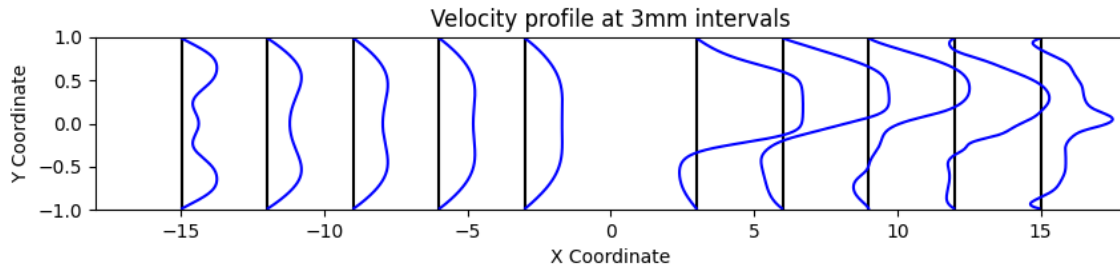


Figure 5.21: Flow-profile for class III at  $t = 1.250$  s  $\uparrow$ .

the flow stabilizes again and the turbulent effects decay and die out. This clearly indicates the transient behaviour of turbulence for this flow class, opposed to sustained turbulence. Figure 5.19 highlights the re-circulation of the flow, mainly under the jet. The velocity field possesses more random flow directions, especially halfway through the post-stenosis part. Directional arrows are not the most optimal way to visualize the rotation in the flow, however, their purpose here is to emphasize the re-circulation of flow. Finally, plot 5.21 show the flow profile, under the same temporal and spatial conditions as previous plots. The flow requires a longer length to develop to a somewhat parabolic flow-profile. The post-stenosis part shows the upwards deflection of the jet, which gradually angles towards the centerline again. The re-circulation of flow is most prominent below the jet, but a small section of re-circulation can be observed above the jet. Note that for turbulent flow, the flow profile is not a proper metric, given its random and sporadic nature to change direction and magnitude.

As the indications of (transition to) turbulent flow are clearly visible in the flow plots, a certain degree of particle mixing can be expected for this flow-case.

Now that the basic premise of each flowclass has been briefly discussed, the addition of particles to the simulation is now justified. Again, the same flowclasses are investigated.

### 5.3 Analysis of particle mixing

The flow as displayed in Subsection 5.2 serves as the basis for particle transport through the model. The particle initialization procedure is described in Subsection 5.1.4. . The simulations return data files containing the spatial information per particle in the simulation for every 10th sampling time-step, of which the position and velocities are the variables of interest. This results in a sampling frequency of 23, 91 and 227  $kHz$  respectively for the three flowclasses. Tracking of the particles initiates when the particles are released in the simulation and ends when the particles cross any physical bound of the model. In practice this implies that the particle tracking terminates when the particles cross the outlet boundary. In practice, this results in a different number of sample points per particle, due to initial positioning and trajectory. It is important to distinguish three different section of the model. The pre-stenosis part consists of the particle release in the catheter tip and includes the necessary distance for the flow front to develop. Particle mixing behaviour is not of interest here, since this section is purely to develop the flow and initialize the particles. The next section contains the stenosis onset, throat and stenosis expansion. It ensures that the flow accelerates and serves as the onset for turbulence in the model. Particles will be driven towards the centerline due to the narrowing of the vessel. The final section includes the section in which particle mixing is of interest. It represents the hepatic artery in which turbulent flow might induce particle mixing. In Table 5.7, an overview is given of the 9 main simulation cases, which are labelled according to their flow class and particle release-instant.

| Flow class | Re  | Particle release-instant  |   |  |
|------------|-----|---|---|--|
|            |     | B  | C  | D  |
| I          | 160 | I-B   | I-C   | I-D  |
| II         | 450 | II-B  | II-C  | II-D   |
| III        | 700 | III-B   | III-C   | III-D  |

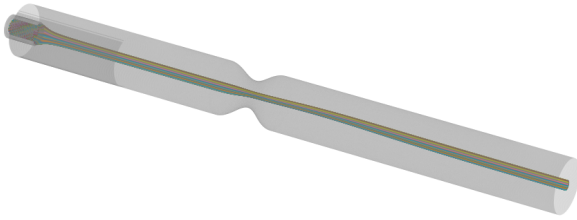
Table 5.7: Simulation overview, labelled.

In the following, mixing behaviour of particles has been analysed with visualizations and statistical measures. The main focus of the particle distribution is in the  $y - z$ -plane, normal to the vessel's main axis. Therefore, 2D particle distribution plots give proper insight and are used frequently to assess mixing behaviour. Regions are referred to in terms of cardinal directions, with the north being positive  $y$ -direction. Additionally, 3D plots of particle trajectories help paint an immediate overview of the evolution of the particles, albeit more computationally expensive to construct. Finally, in an attempt to quantify the data, several established statistical methods are employed to determine the mixing in each simulation for comparison. All of the plots are discussed in more detail in the coming sections. The goal of this subsection is to obtain a general overview of the nine simulation cases.

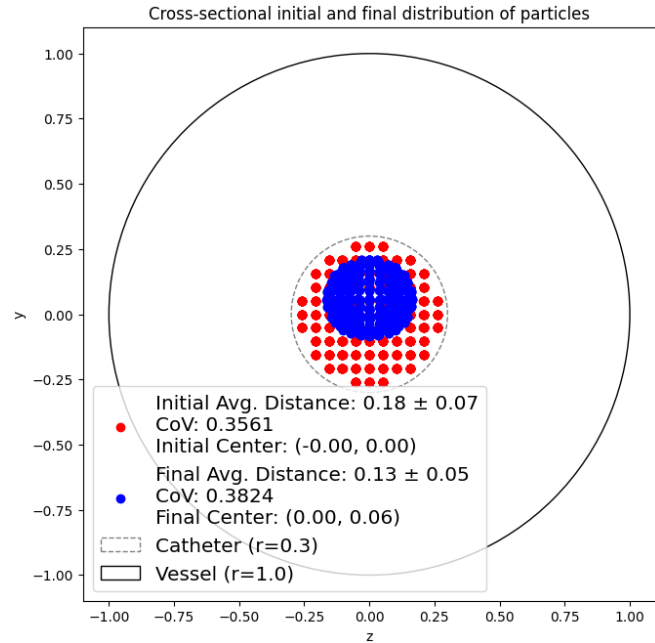
### 5.3.1 Preliminary simulation analysis

#### Cases: I-B, I-C & I-D

The results of flow class I are grouped together given their similarities. Nonetheless, subtle differences manifest in the simulations which are worthy of elaboration.



(a) I-B: 3D particle trajectories.



(b) I-B: Initial (Red) and Final (Blue) particle distribution.

For simulation I-B, the particle trajectories in Figure 5.22a show streamlined behaviour all the way throughout the model for the entire simulation time. The particles are being pushed towards the centerline due to the narrowing of the stenosis throat. There is a slight deflection upwards (in positive  $y$ -direction), which is visualized in Figure 5.22b. This behaviour is expected given the offset in  $y$ -direction of the throat. The plot displays the Center of Gravity (C.o.G.) of the distribution and the average distance to the centerline. The C.o.G. is defined as the average location of all the particles combined. These two are simple yet efficient metrics to assess the final particle distribution. Note that the term 'final' refers to the position of the particles at the time they exit the model, which in this case is at the outlet boundary. Additionally, little variation in  $z$ -direction can be distinguished. The redirection of flow through the stenosis throat leads to a general increase in particle clustering.

Plot 5.23 shows the average distance to the centerline across the entire model (dark blue line). It plots the average distance on the  $y$ -axis versus the scaled  $x$  distance in terms of the amount of diameters. Walking through this graph, starting from the  $x = 0$  position, first shows the particles in the catheter tip. These particles do not move radially in the catheter so the average distance remains the same. Then the distance abruptly increases, due to flow effects. The flow in the annulus around the catheter has a higher velocity than the flow exiting the catheter. For the low Re-numbers in play, this allows for the slight expansion of flow exiting the catheter, which is then quickly suppressed again. This can be attributed to the developing Poiseuille flow profile, which stabilizes at around 5 lengthwise diameters inwards. The particles are then slightly more clustered compared to the catheter configuration, however, they enter the stenosis throat symmetrically. Inside the throat, the average distance decreases to a minimum value, due to the acceleration of the bulk of the flow. The upwards deflection in turn increases the average distance again. Due to the excessive length of the model for the lower flow class, the particles return to the Poiseuille flow distribution, albeit, slightly offset. The shaded band around the main blue line represents the standard

Particles' Average Distance to Centerline  $\mu$  with standard deviation  $\sigma$ , along model

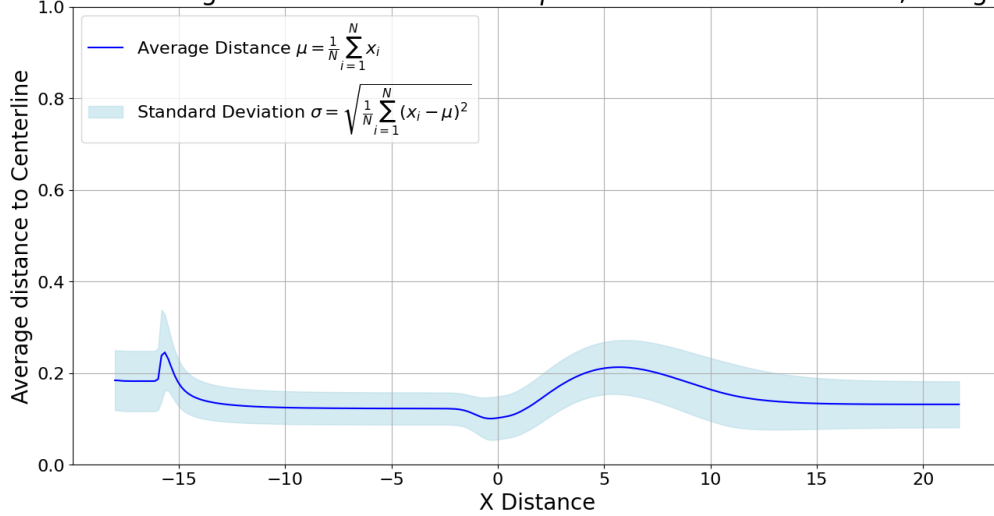
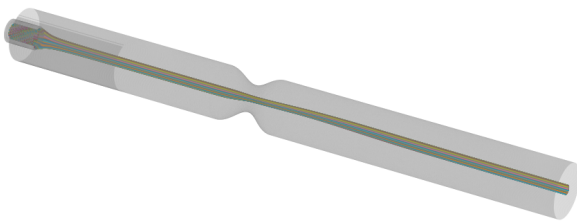
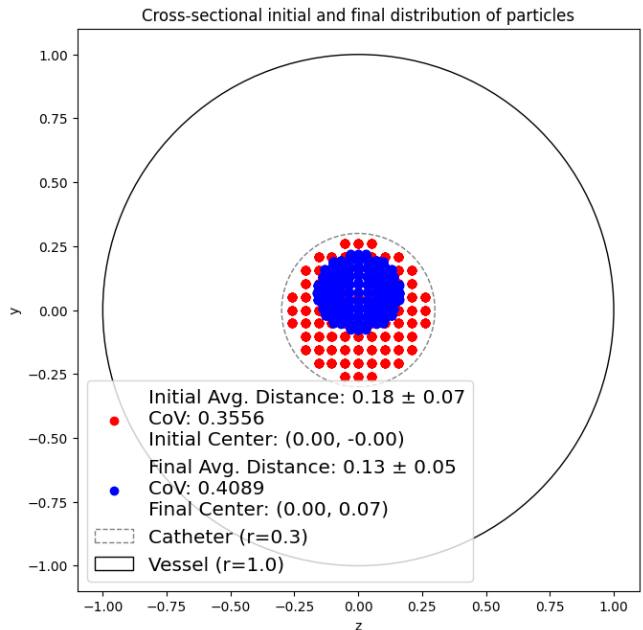


Figure 5.23: I-B: Mean and Standard deviation.

deviation, which is fairly constant throughout the simulation. Note that the standard deviation is always a single value for any given time or distance instant. The values on the y-axis do not serve as absolute values for the standard deviation. Also, note that interpolation of particle positions is used in order to construct a continuous graph.



(a) I-C: 3D particle trajectories.



(b) I-C: Initial (Red) and Final (Blue) particle distribution.

Simulation case I-C is nearly identical to I-B in terms of visual inspection of the trajectories, see Figure 5.24a. It seems like the pulsating nature of the flow has little effect on the particle transport for these sections of the pulse. Slight differences can be observed in the C.o.G of the final distribution, which is slightly shifted upwards, see Figure 5.24b. This can be explained by the higher flow velocities and hence the larger deflection due to the eccentricity. However, the essence of clustered particles remains

for simulation I-C. Figure 5.25 highlights almost the exact same evolution of the distribution's average distance compared to simulation I-B.

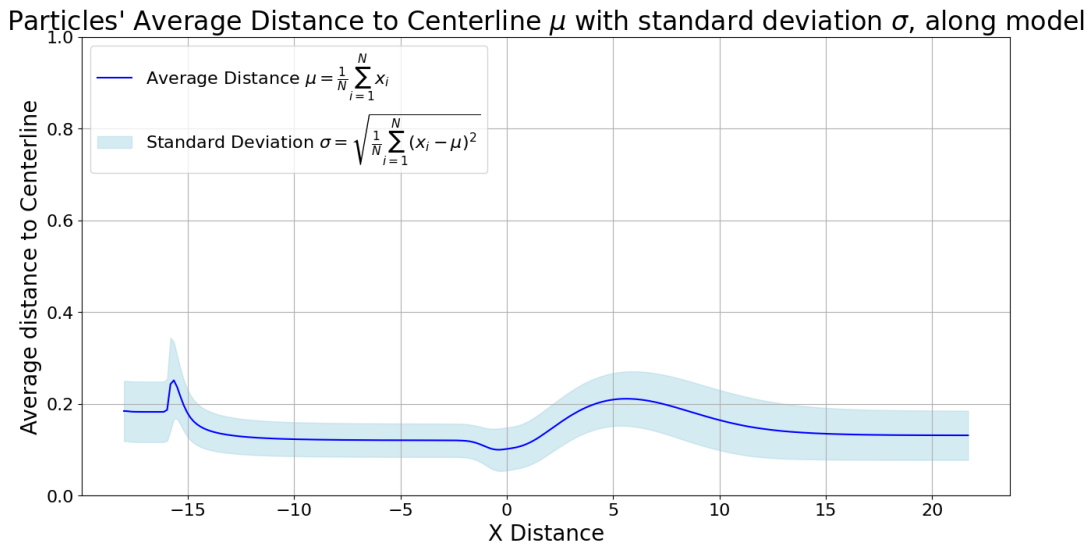
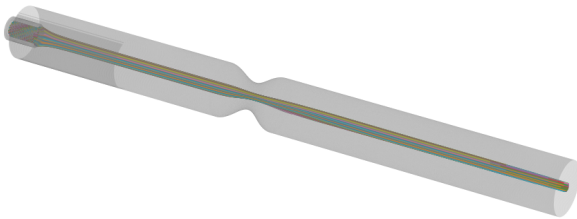
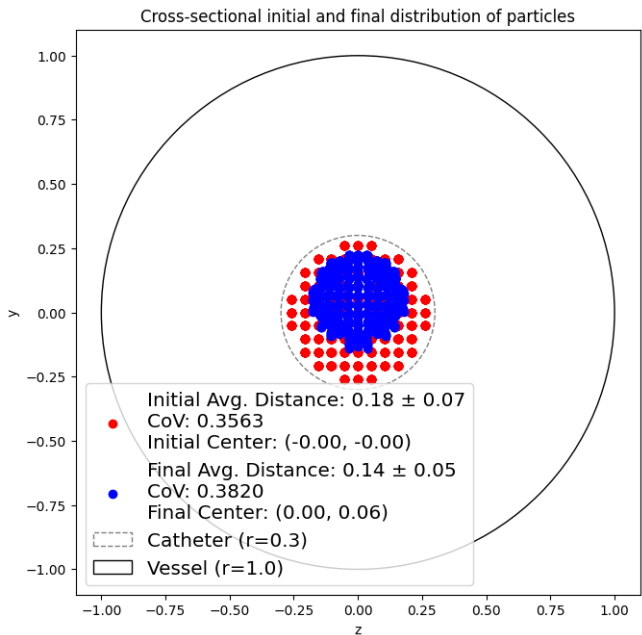


Figure 5.25: I-C: Mean and Standard deviation.



(a) I-D: 3D particle trajectories.



(b) I-D: Initial (Red) and Final (Blue) particle distribution.

Finally, the particle trajectories of simulation I-D are displayed in Figure 5.26a. Major similarities can be observed for the last particle-release instant compared to the first two instances (Figure 5.26b). The C.o.G of the final distribution shifts ever so slightly downwards again, matching the result of I-B. Once again, this amplifies that the phase of the pulse has little effect on the final particle distribution at low Re.

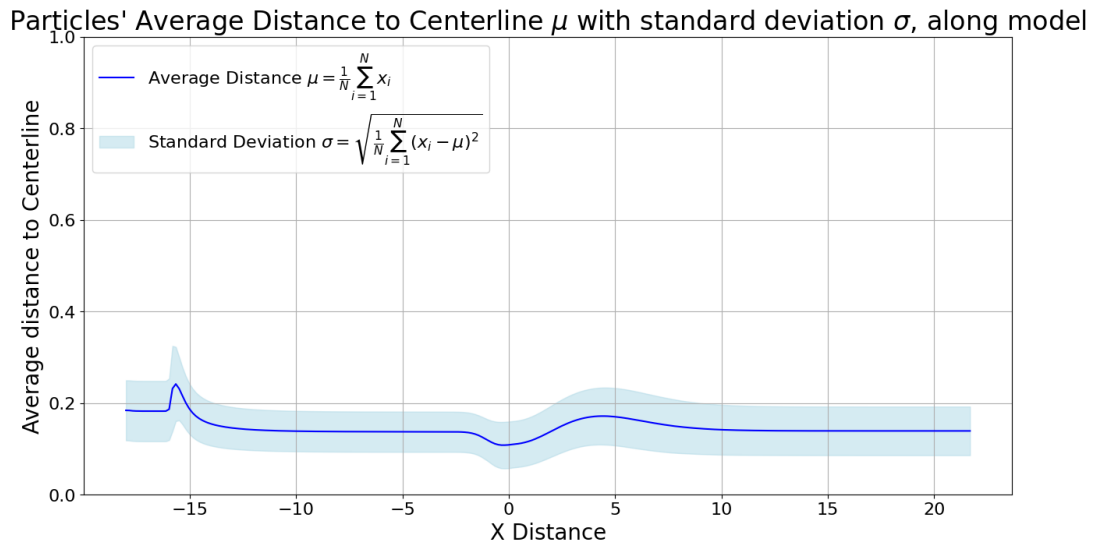
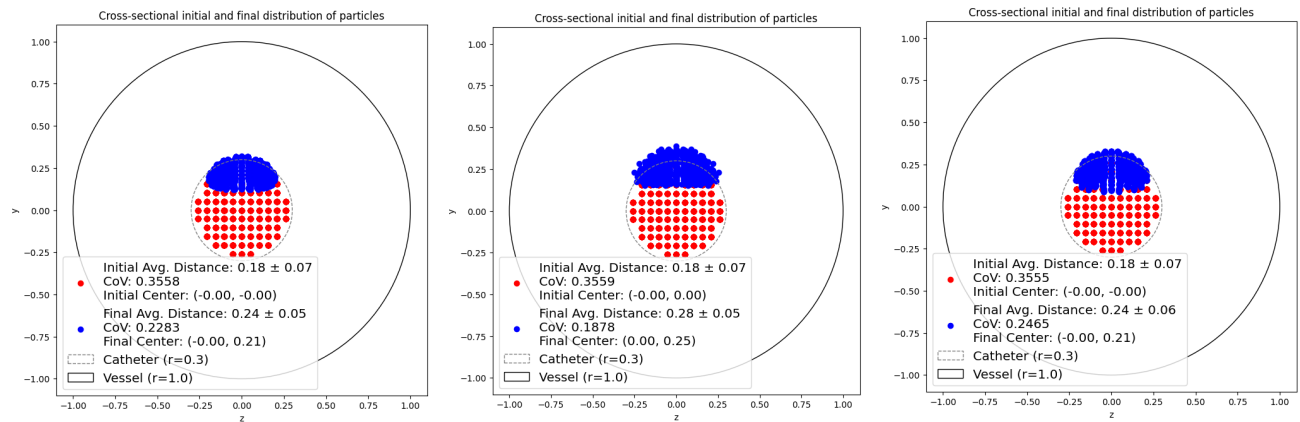


Figure 5.27: I-D: Mean and Standard deviation.

To conclude, as expected, flow case I does not exhibit any particle mixing. However, it provides values to compare future simulations in terms of particle dispersity and mixing behaviour quantification.

### Cases: II-B, II-C & II-D

For flow class II, the same visualization graphs are used as for flow class I. Given their similarity to each other, a more concise analysis is performed. As can be seen in Figures 5.28 and 5.29 the particle distributions differ little again. The same II-B to II-C and the consequent downwards shifting behaviour from II-C to II-D is present. Since the jet, which carries the particles is stronger in flow class II, the deflection is larger and the effects on particle transport are still active when the particles exit via the outlet. There are no particles which deviate from the trajectory of the jet which yields the same conclusion when looking at the flow field. The particles clearly stay within the bounds of the jet, and not a single particle crosses the interface between the forward and backward-flowing regions.

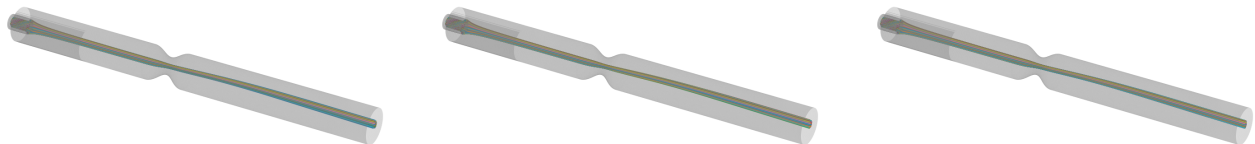


(a) II-B: Initial (Red) and Final (Blue) particle distribution.

(b) II-C: Initial (Red) and Final (Blue) particle distribution.

(c) II-D: Initial (Red) and Final (Blue) particle distribution.

Figure 5.28: Flowclass II, 2D cross-sectional particle distribution.



(a) II-B: 3D particle trajectories.

(b) II-C: 3D particle trajectories.

(c) II-D: 3D particle trajectories.

Figure 5.29: Flowclass II, 3D particle trajectories.

Given their similarity, Figure 5.30 suffices to highlight the distribution's average distance to the centerline. The pre-stenosis region again experiences rapid expansion and compression of the distribution when exiting the catheter. The following region up to the stenosis exit is quite similar to flow class I. The main difference between I and II is highlighted by the larger average distance and the longer convergence to a steady state in the post-stenosis part. One can argue that the effects of the jet have not worn off, which in turn leads to an incomplete overview. This argument can be countered by the fact that no turbulence is expected further downstream so a similar convergence to a stable Poiseuille flow profile is expected (e.g. see Figure 5.25). The main takeaway for this flowclass is the absence of any turbulence and consequent mixing behaviour.

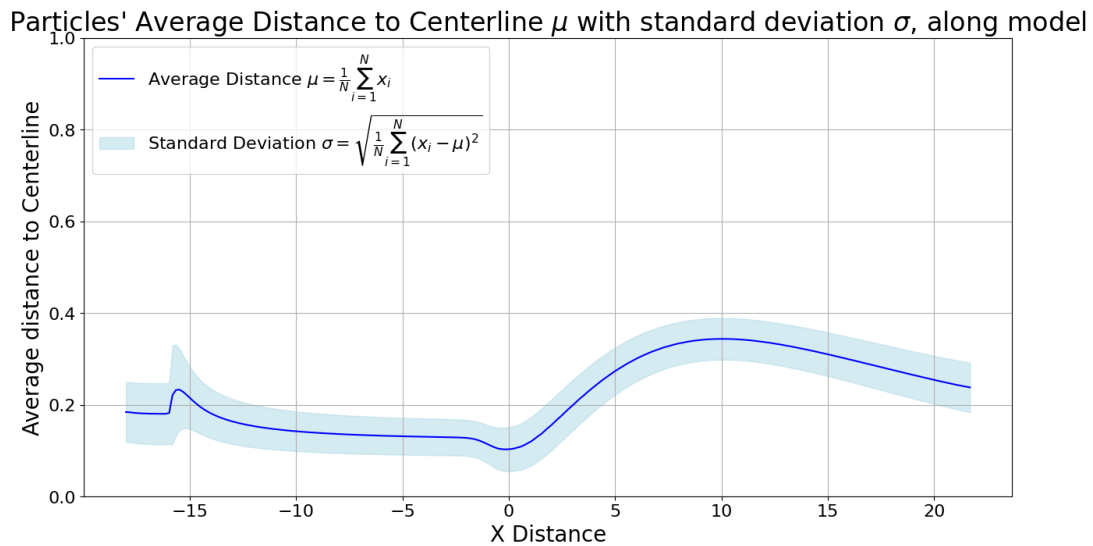


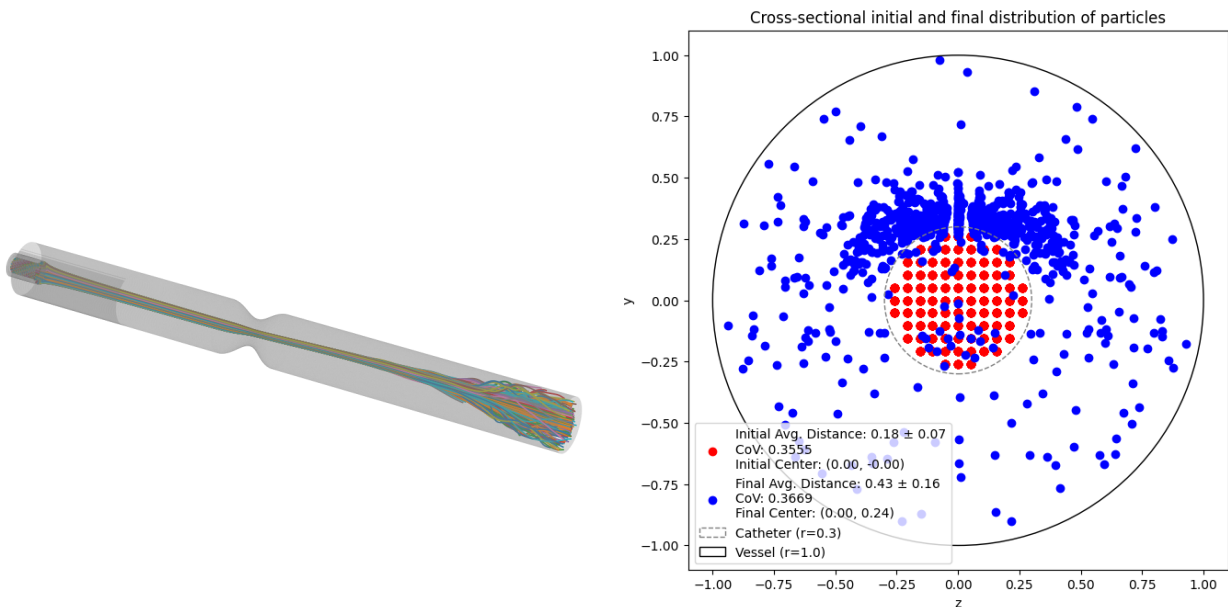
Figure 5.30: II-C: Mean and Standard deviation.

**Case: III-B**

Flow class III is the first in which turbulence is observed, so it is expected to monitor an inherently different particle distribution. Given the higher  $Re$  at play, particles traverse the model more quickly. The average particle residence time in the model is around 0.05 seconds for this flow class. At particle release instant B, the input flow velocity is but the flow is starting to decelerate towards peak systole. In Figure 5.31a the familiar 3D model of the particle trajectories is displayed. This confirms the hypothesis of particle mixing for flowclass III. Particles travel smoothly through the throat but halfway in the post-stenosis region, the particles disperse in both the  $y$ - and  $z$ -direction. In Figure 5.31b, the initial distribution and the final distribution are displayed. Observing the distribution, symmetry is almost conserved in  $z$ -direction. The upward shift of the distribution's C.o.G. is noticeable. A large cluster can be distinguished in the upper half of the cross-section, which overlaps with a semi-circle. The origins of the jet can still easily be traced in the final distribution. The average distance to the center has increased to a value of 0.43. The standard deviation is 0.16 resulting in a Coefficient of Variation (CoV) of 0.37.

These values can be compared to a theoretical case of perfect particle mixing: A system which demonstrates spatial homogeneity, wherein particles are perfectly mixed, and the distance between particles remains uniform throughout the entirety of the system. In this hypothetical system, the average distance of the particle distribution is 0.667 and the standard deviation is 0.236, resulting in a CoV of 0.354.

It is important to note that the final distribution is rather a screenshot at the end of the simulation. It does not consider particles which have not yet reached the outlet of the model. A total of 2 particles have not crossed the outlet boundary at the time of termination of the simulation. These particles are either still travelling towards the outlet, or have left the model via the vessel walls, in which case their absolute distance to the centerline has exceeded a value of 1.



(a) III-B: 3D particle trajectories.

(b) III-B: Initial (Red) and Final (Blue) particle distribution.

Figure 5.31: III-B: Simulation results.

Figure 5.32 shows the cross-section divided into numerous slices, which subdivide the surface into sections. The particle density per section is then calculated. This provides insight into the regional

dispersity of particles. The standard deviation between the densities of the sectors is also provided as a statistical metric. It highlights the clustering of particles around the jet location. The outer ring close to the vessel walls contains noticeably fewer particles compared to the center. Especially near the northern and southern areas, the degree of mixing is lower compared to the eastern and western regions. Nevertheless, the sectional density of this simulation is not uniform.

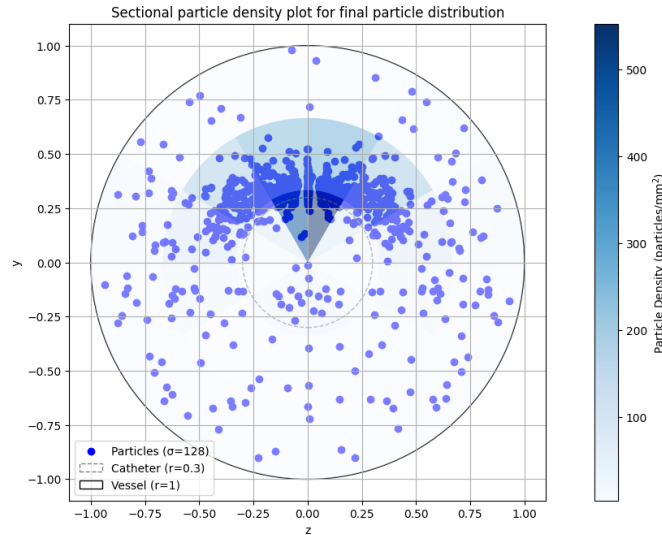
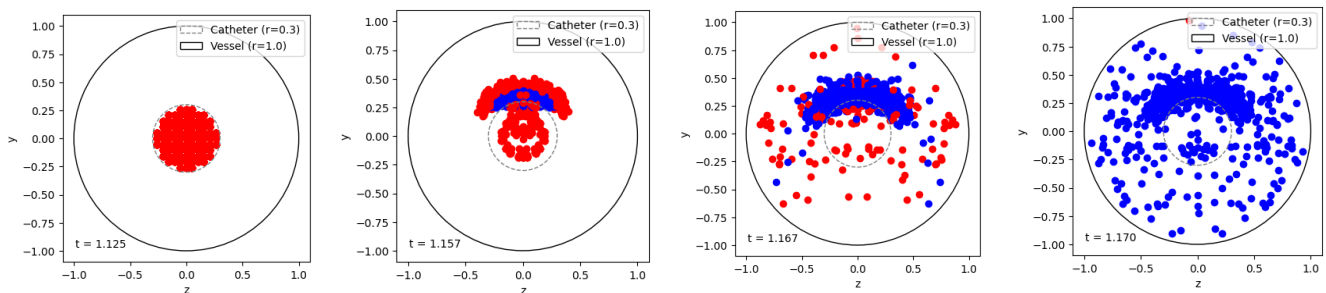


Figure 5.32: III-B: Sectional density.

Figure 5.33 shows the cross-sectional area of the flow at different time instances. Note that particles in red represent particles still in simulation while the final location of the particles which have exited the simulation at the given time-step is blue. See Figure caption for an explanation. It highlights the delay between the front and the rear of the initial particle distribution in terms of travel time. The majority of the particles remaining close to the centerline exit the simulation first. These particles are captured by the jet, which retains its shape up to the time-instant where the turbulence is introduced. This observation agrees with the expected results based on the flow field. There are two outlier particles which stay within the simulation for its entire duration.



(a) Initial particle configuration;  $t = 1.125$  s. (b) Particles in throat vicinity;  $t = 1.157$  s. (c) Majority of particles exited;  $t = 1.167$  s. (d) (Almost) All particles exited;  $t = 1.170$  s.

Figure 5.33: III-B: Snapshots in time.

Finally, Figure 5.34 shows quite a different plot compared to the previous. The same average distance can be observed for the particle distribution in the pre-stenosis and throat region. However, the average distance approaches a value of 0.43 in the post-stenosis region. The standard deviation is a clear indicator

of mixing behaviour, which significantly increases after around 8.5 lengthwise diameters. Given the slope of the standard deviation bounds, it is reasonable to assume that the mixing behaviour might not have settled during the entire length of the simulation. Any error regarding the average distance can be attributed to the spline interpolation method.

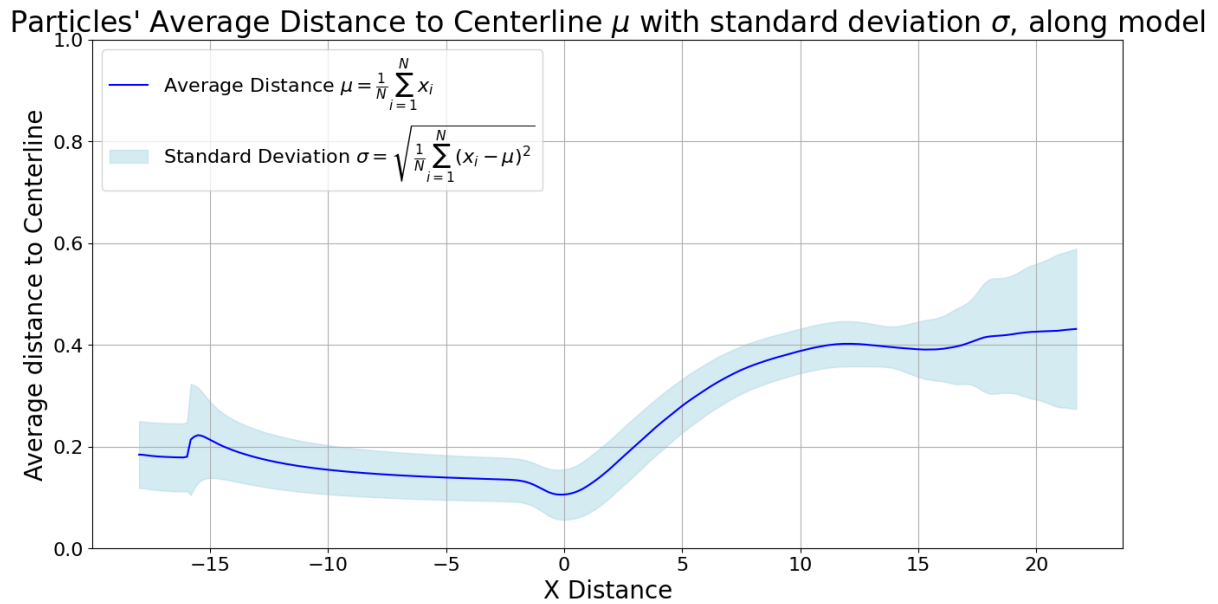
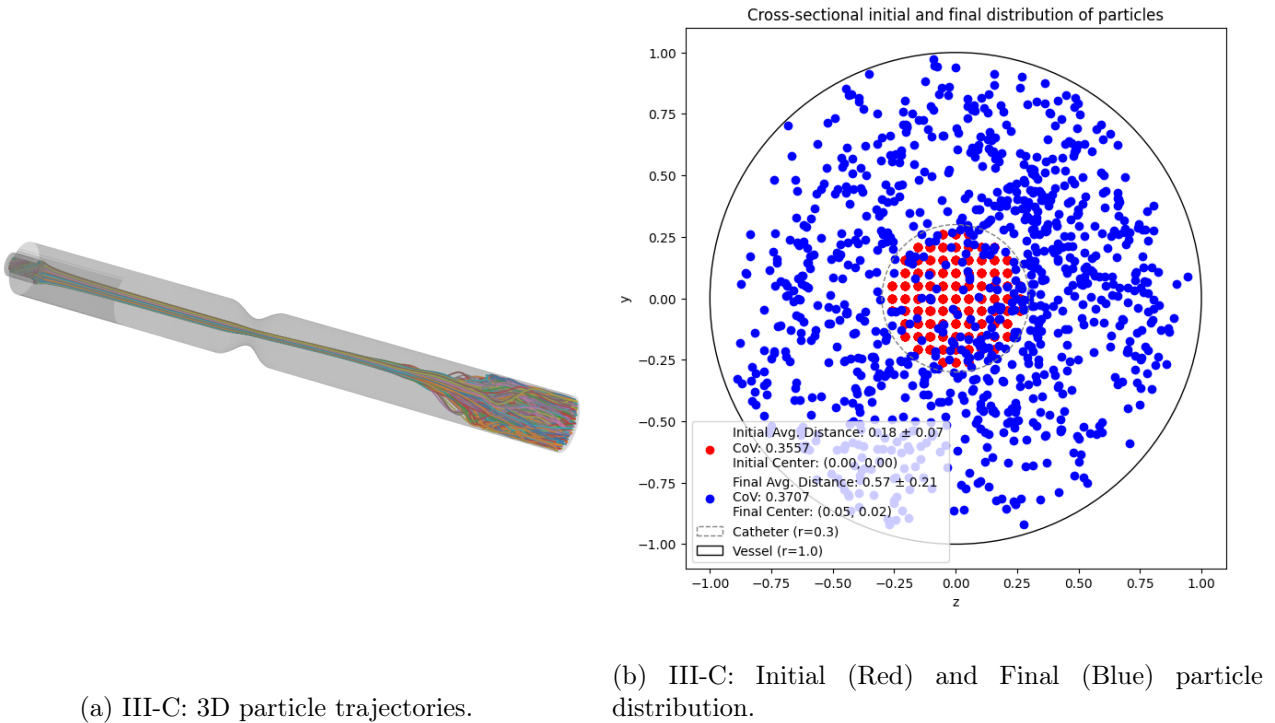


Figure 5.34: III-B: Mean and Standard deviation.

**Case: III-C**

Simulation III-C shows the first real signs of proper mixing behaviour thus far. In Figure 5.35a, the spaghetti-like trajectories are similar but more profound to those of Figure 5.31a. The addition of Figure 5.35b further distinguishes the two simulations. The average distance has increased by 33% compared to III-B. The C.o.G. has significantly shifted eastwards, and slightly upwards. Little remains of the effect of the positively upwards reflected jet. The location of the onset of turbulence is closer to the stenosis throat compared to that of III-B, which translates into more profound mixing behaviour. Subsequently, the clustering of particles can be extracted from the final particle distribution plot. In general, the region near the vessel wall is still sparsely populated compared to smaller radii region, but this effect has worn off compared to III-B.



(a) III-C: 3D particle trajectories.

(b) III-C: Initial (Red) and Final (Blue) particle distribution.

Figure 5.35: III-C: Simulation results.

Figure 5.36 confirms the improved mixing behaviour, the slices are more uniform and the standard deviation of the population density has decreased almost five-fold compared to III-B. The section of the outer annulus is the least populated region. The middle annulus contains the majority of the particles. These slices boast population densities twice or thrice as low as the outer regions. Symmetry is clearly not conserved for the final particle distribution in  $z$ -direction. However, the overall spread of the particles is more extensive.

Particle traverse time of the model is comparable to III-B, with a throughput of around 0.05 seconds, which can be extracted from Figure 5.37. Figure 5.37b highlights the differences in particle location at the given time instant. Certain particles have been displaced to the outer edges whilst some are still travelling through the stenosis throat. This is an important factor to keep in mind while assessing the mixing criteria later on. Figure 5.37d indicates the presence of an outlier particle still in simulation while the rest has exited the simulation.

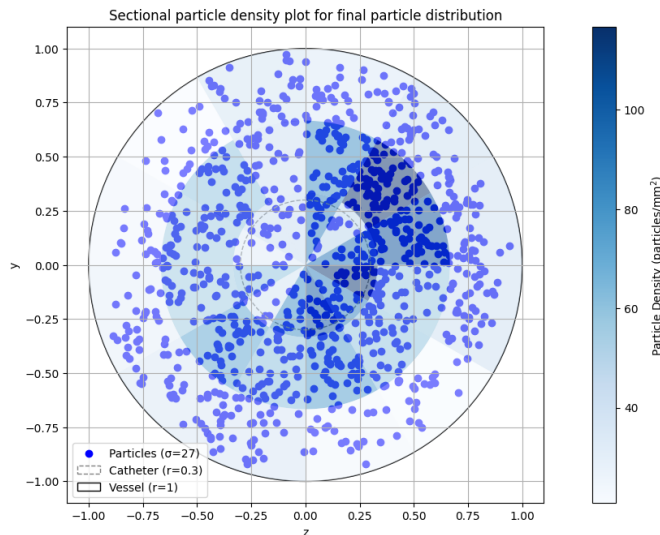
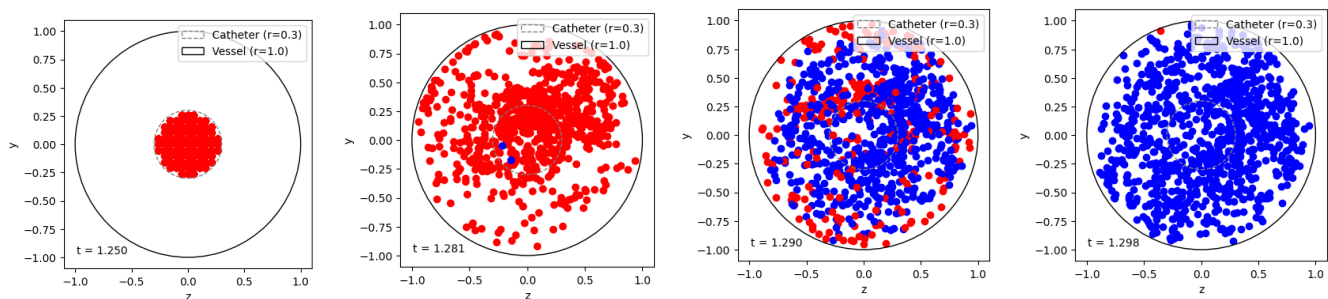


Figure 5.36: III-C: Sectional density.



(a) Initial particle configuration;  $t = 1.250$  s. (b) Particles in throat vicinity;  $t = 1.281$  s. (c) Majority of particles exited;  $t = 1.290$  s. (d) (Almost) All particles exited;  $t = 1.298$  s.

Figure 5.37: III-C: Snapshots in time.

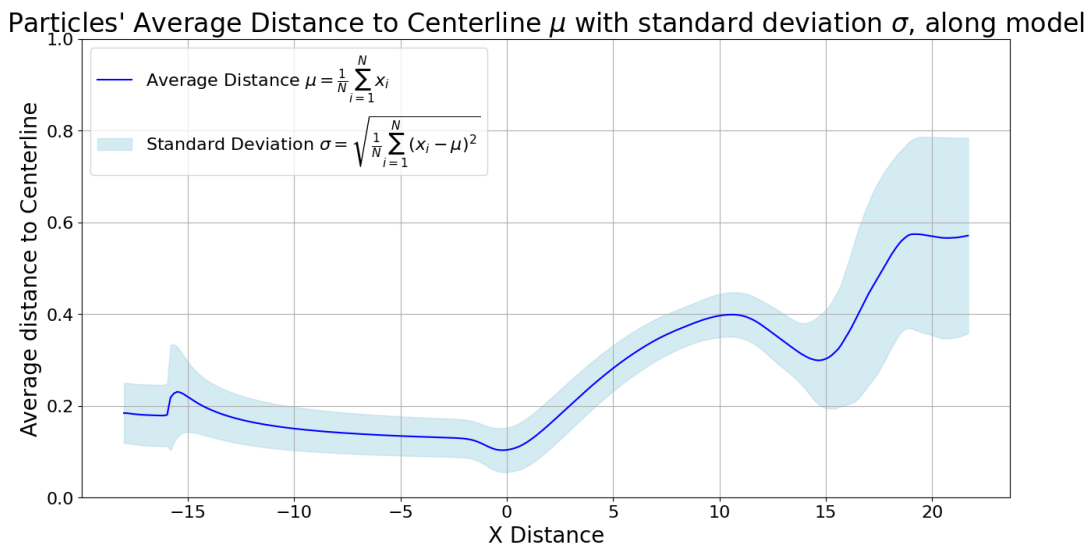


Figure 5.38: III-C: Mean and Standard deviation.

Regarding Figure 5.38, the onset of turbulence now occurs after a drop in average distance, which is then followed by a large increase, complemented by an even larger standard deviation. The average distance seems to stabilize around its maximum value, an extrapolation that a larger model and a longer simulation can answer. The standard deviation seems to have reached a constant value. One statement that can be established from this observation is that the jet containing the particles travels further compared to III-B but breaks down with more turbulent activity, causing a larger spread in particles.

**Case: III-D**

The final simulation III-D allows for examination of the later stages of turbulence in the pulse. The onset of the turbulence in the simulation appears at a distance which is in between III-B and III-C. Visible in Figure 5.39a, the mixing volume is smaller compared to III-C, and additionally, mixing takes place in the final stages of the model. The average distance exhibits the highest value yet. Figure 5.39b shows a spread of particles which is comparable to III-C. The jet's effects, which has left its mark in all previous simulations, now seems to be of lesser influence. Average distance has increased compared to III-C by around 5%, with the standard deviation changing remaining similar. The C.o.G. is shifted slightly off-center, albeit still reasonable close to the centerline.

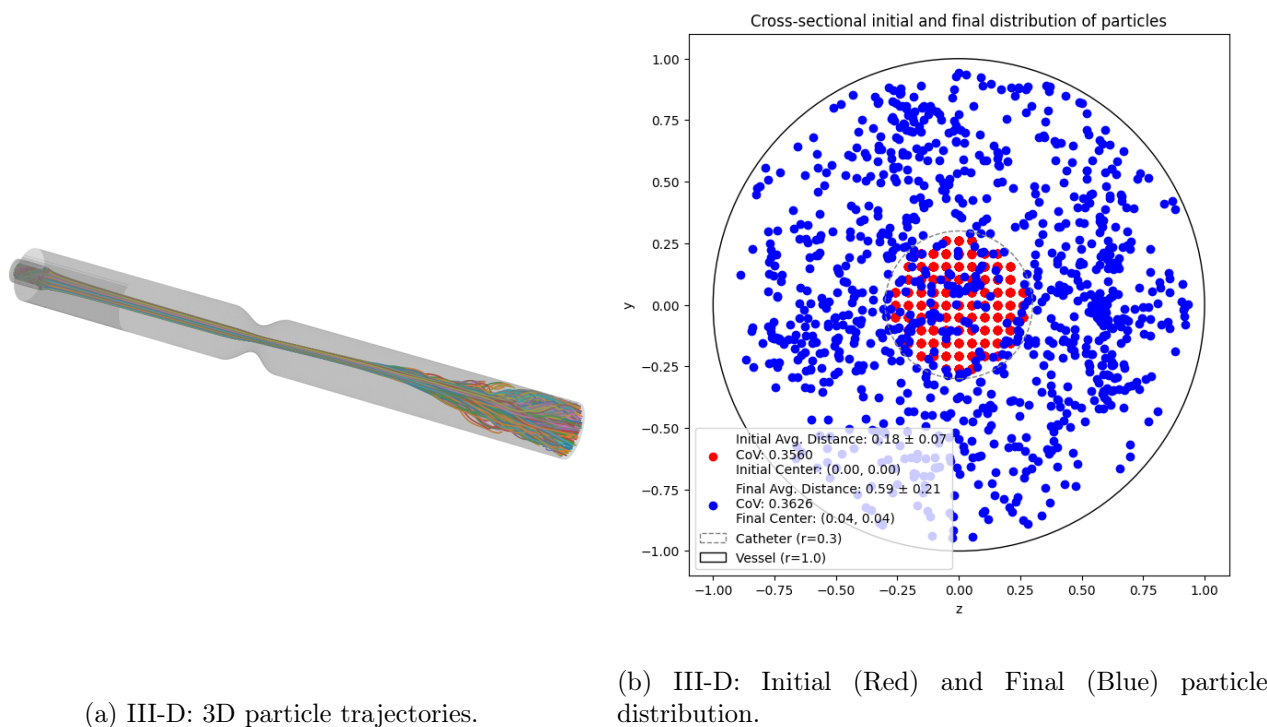


Figure 5.39: III-D: Simulation results.

The sectional plot, see Figure 5.40 confirms the previously stated. The middle sector contains almost the entirety of the particles. The standard deviation of the population density is 25, which is 512% lower than III-B, and also slightly lower than III-C. Also note that there are a handful of particles which are still in the model at the termination of the simulation instead of exiting via the outlet. Figure 5.41 indicates a similar throughput time compared to III-B and III-C.

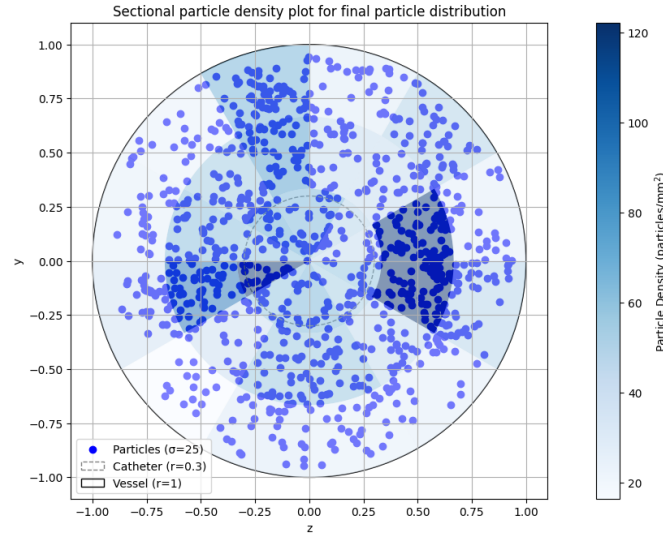
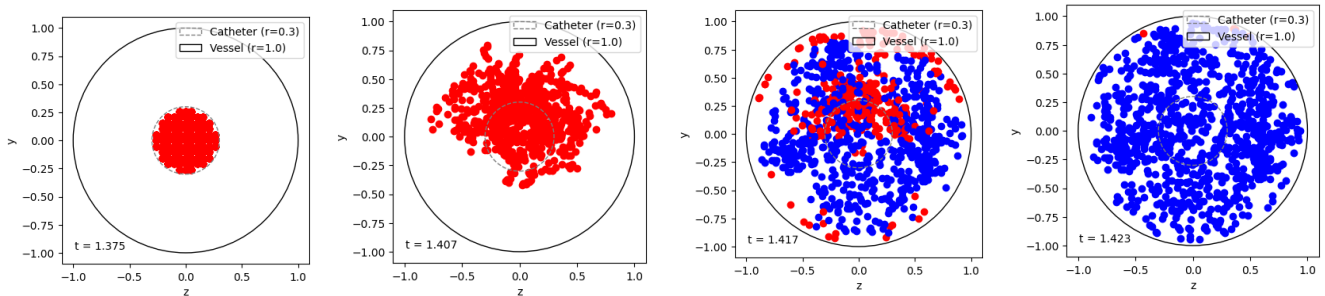


Figure 5.40: III-D: Sectional density.



(a) Initial particle configuration;  $t = 1.375$  s. (b) Particles in throat vicinity;  $t = 1.407$  s. (c) Majority of particles exited;  $t = 1.417$  s. (d) (Almost) All particles exited;  $t = 1.423$  s.

Figure 5.41: III-D: Snapshots in time.

The statistical graph in Figure 5.42 is comparable in shape to III-C, in which the average distance falls prior to the smooth jump to a higher ensemble average. The drop does not necessarily mean that the particles follow the jet, which in turn approaches the centerline again, but rather that particles might travel more quickly to the other regions of the model. A key difference is the fact that the line has not yet reached a stable value, indicating that the mixing behaviour might not have settled yet.

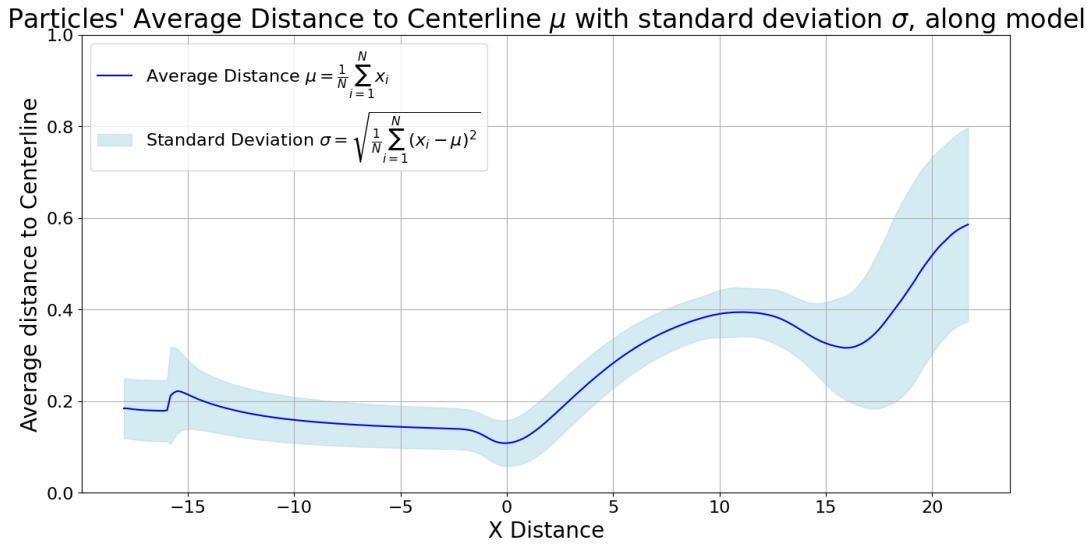


Figure 5.42: III-D: Mean and Standard deviation.

This concludes the preliminary analysis of the nine simulations. This analysis of particle distribution has indicated basic insights, which highlights with which simulation cases to proceed in more detail. Flowclass I shows purely laminar flow behaviour and the subsequent particle trajectories coincide with the parallel streamlines. Flowclass II indicates slight disturbances in the flow, which translate to a rougher final distribution of particles. Early characteristics of mixing behaviour could be attributed to the observed randomness, however, their influence and effects are very minimal to the particle transport. These two flowclasses have provided insight into the low  $Re$  flowregime, but are from hereon excluded for further study. This leaves the highest flow class III for further elaborate analysis, which commences in the Chapter 7. In the next chapter, a comparison between different density particles is performed.

# Chapter 6

## Comparison mixing behaviour with higher density particles

This chapter delves into the comparison of simulations with the aforementioned density of microsphere particles and higher density particles. The first part consists of an overall effect analysis of the density and subsequent comparison with the previous simulation results, in Chapter 5. More generally, the chapter aims to link the flow characteristics to the resulting particle distributions for both simulation cases. This allows for establishment of an important connection between the particles and the flow. Once this connection has been established, the detailed analysis of the initial simulations is commenced.

### 6.1 High-density particle simulations

The nature of this section needs some explanation given its specifics. During the process of submitting simulations to Snellius, a discrepancy has been found between the proposed simulation basis and the actual simulation input. This difference has been identified as the value for the particle density. All other parameters for both the flow, the model, and the particles remain unaffected. Conventionally, it is practice to disregard the simulation results, given the mistake in initial conditions. However, given the fact that these simulations are (computationally) expensive, an alternative assessment can be established. This is mainly due to the fact the incorrect density has a practical value, see Table 6.1. The mistake can simultaneously provide more information regarding the influence of density on the simulations.

| Particle density | Symbol | Unit      |
|------------------|--------|-----------|
| Normal (Holmium) | 1.4    | $gr/cm^3$ |
| High             | 10.56  | $gr/cm^3$ |

Table 6.1: Simulation differences.

From hereon, till the remainder of this chapter, the simulations in Chapter 5 are referred to as normal density and the other as high-density. The high-density particles are exactly 10 times as dense as the fluid itself, resulting in a factor of  $\approx 7.5$  more dense particles. This alteration makes the particles comparable to a material in between silver and lead. As the particles are heavier, their inertia is larger, hence their Stokes number is higher. This could allow for the hypothesis of particles which are less likely to follow the streamlines, but given the order of events, this hypothesis was never proposed.

Given the nature of the flowclasses, only the third flowclass is eligible for analysis. Flowclasses I and II exhibit little to no differences compared to the normal density simulations and provide no new insights.

### 6.1.1 Flow

A comparison can be made between the initial- and final state of both simulations. Using the restart system, for both densities, the initial state (pre-), is identical. The injection of particles, due to the two-way coupling affects the flow itself. Its effects should be engraved in the flow profile, even after the simulation has terminated. Inspection of the cross-section flow profiles, like in Section 5.2 provides this visual comparison.

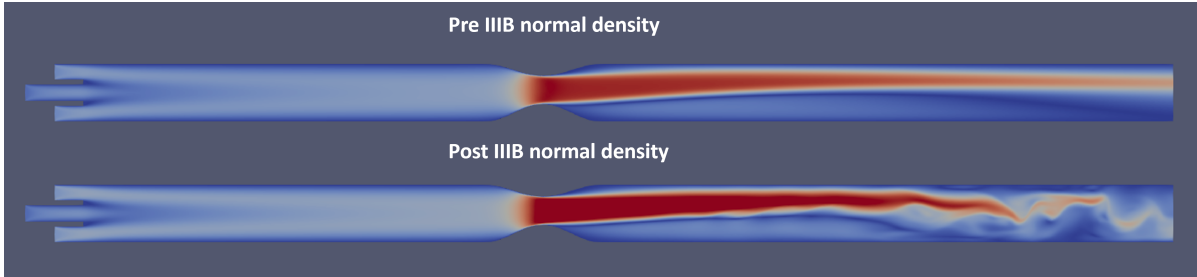


Figure 6.1: III-B, normal density: Pre ( $t=1.125$  s  $\curvearrowright$ ) and Post ( $t=1.250$  s  $\curvearrowright$ ).

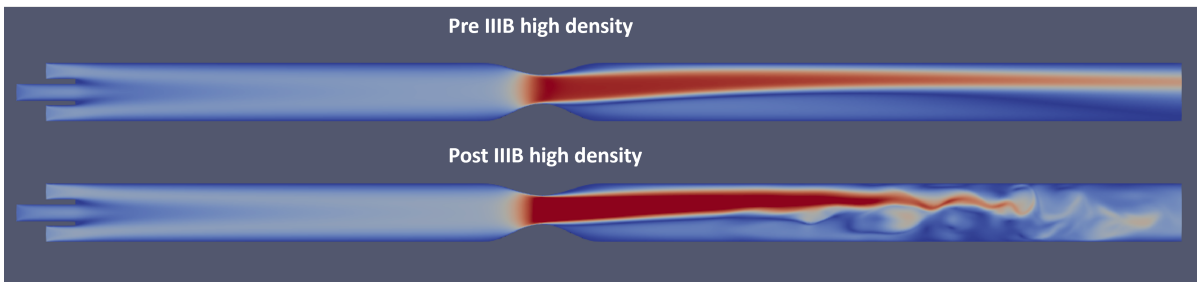


Figure 6.2: III-B, high-density: Pre ( $t=1.125$  s  $\curvearrowright$ ) and Post ( $t=1.250$  s  $\curvearrowright$ ).

For simulation III-B, the difference between the normal and high-density is clearly visual. Both simulations boast turbulent activity, with the jet collapsing and the subsequent vortices in the flow. The jet of the normal density retains its shape slightly longer and the flow itself possesses a slightly higher velocity in the latter stages of the model. However, the most important metric is the visual cue that the simulations differ, which indicates the effect of the particle density on the simulations.

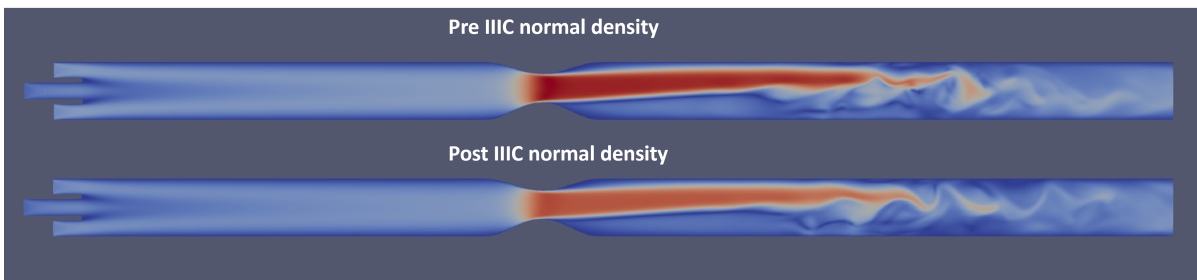


Figure 6.3: III-C, normal density: Pre ( $t=1.250$  s  $\curvearrowright$ ) and Post ( $t=1.375$  s  $\curvearrowright$ ).

Again, both post-snapshots differ between the two simulations. The vorticity of the broken-down jet in the normal density simulation seems to propagate more significantly into the final stages of the model compared to the high-density simulation.

For the final comparison, the post-snapshots are harder to distinguish apart. However, conducted numerical analysis has shown that both states are different and hence, the particle effects still propagate

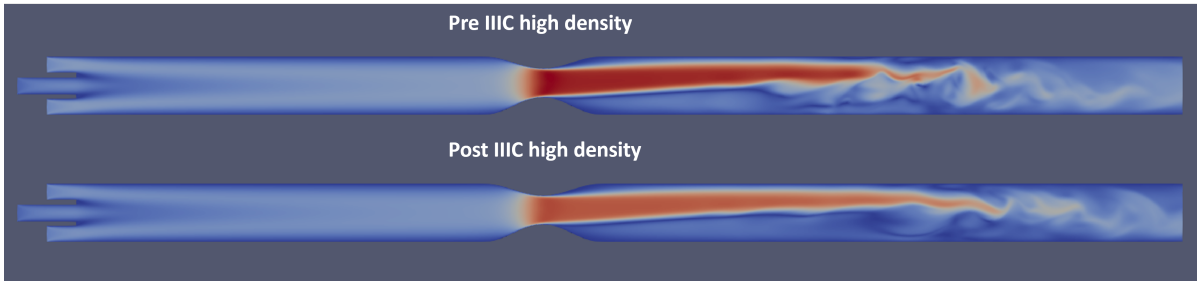


Figure 6.4: III-C, high-density: Pre ( $t=1.250$  s) and Post ( $t=1.375$  s).

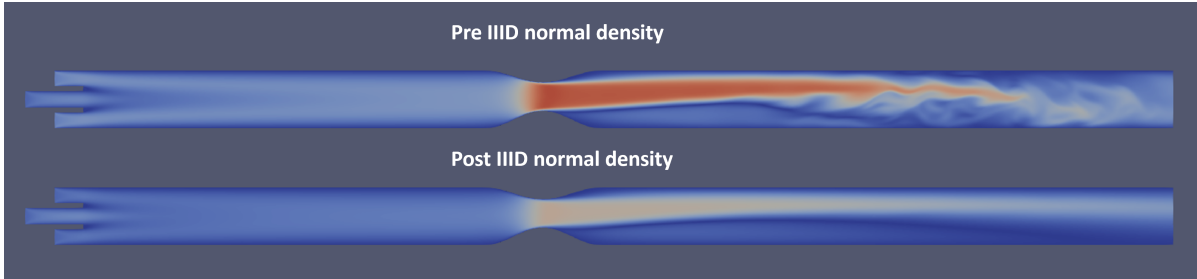


Figure 6.5: III-D, normal density: Pre ( $t=1.375$  s) and Post ( $t=1.500$  s).

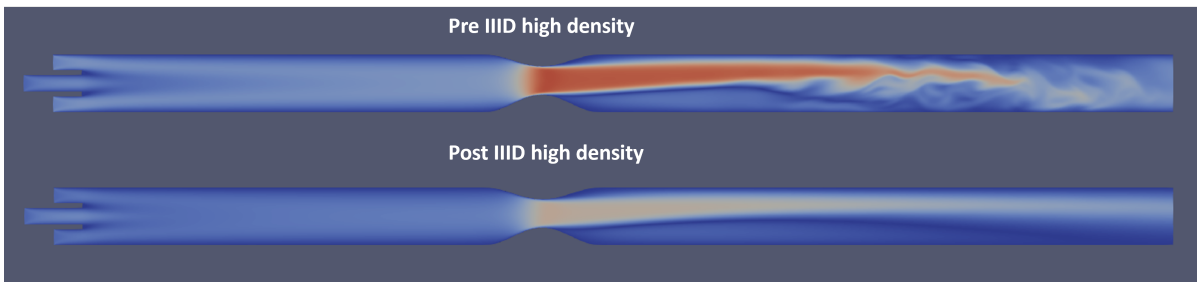


Figure 6.6: III-D, high-density: Pre ( $t=1.375$  s) and Post ( $t=1.500$  s).

up till this time-point. Note that for all the turbulent initial and final states, the snapshot in time is not conclusive about the flow, given the chaotic nature of the flow dynamics.

### 6.1.2 Particles

Now this next section provides further visual comparison of the particles itself. For every simulation, the post-stenosis particle trajectories are given. From hereon, the normal density particles are displayed in blue while the high-density particles are displayed in green. The purpose of these visuals is to clearly differentiate between the location of the onset of turbulence. This approach ignores the distribution in  $z$ -direction, a justified choice given the limited significance of the third spatial direction for this application. Note that these plotted trajectories are the result of each individual particle's route through the model up till the point that the simulation itself terminates. For all simulations, this time window amounts to exactly  $1/8$  of a second. Additionally, the statistical plot containing the particle distribution's average distance to the centerline has been given for both simulations.

Even by visual inspection, see Figure 6.7, one notices clear differences for III-B. The onset of mixing is located further downstream, at around 9 or 10 lengthwise diameters, for the normal density particles, while a fraction of the high-density particles initiates their deviation from the jet trajectory at 6 lengthwise diameters post-stenosis. Concerning the mixing behaviour, the high-density mixing is much more profound,

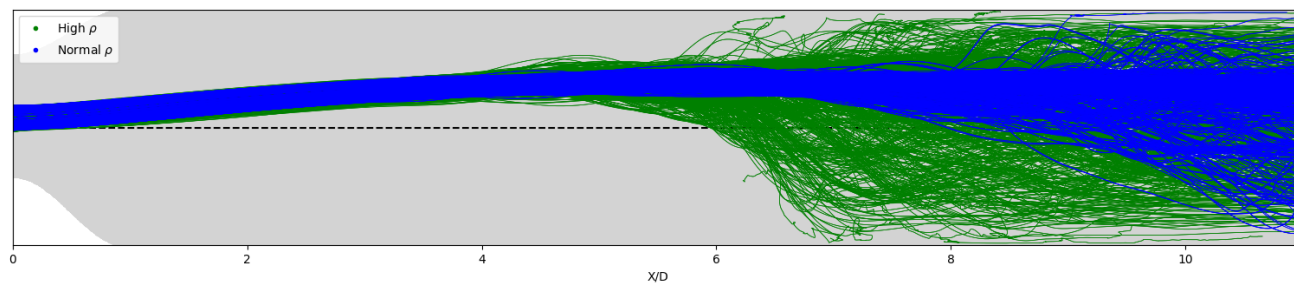


Figure 6.7: III-B 2D post-stenosis particle trajectory comparison.

most likely due to the particle-induced flow characteristics.

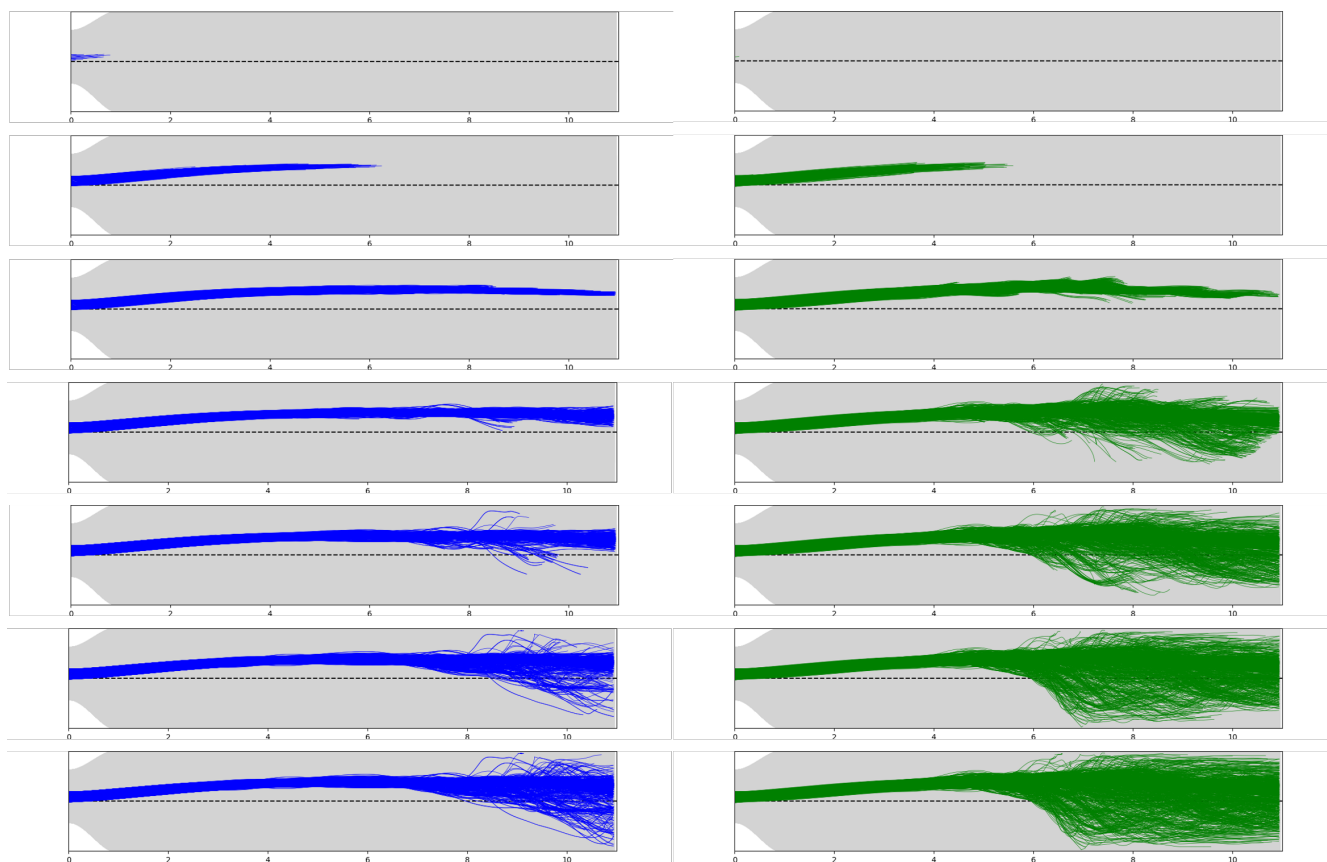


Figure 6.8: III-B snapshots of trajectories at similar time-steps.

Temporal analysis yields the observation that the onset of turbulence and the jet breakdown occur earlier in the high-density simulation. This indicates the importance of the particle density as a variable. In the third and fourth time-step, the normal density trajectories are almost all exclusively laminar, while that is not the case for the high-density particles. There, turbulence induced mixing has already been initiated. Given that the particles are practically at the same location at a given time-step prior to this mixing, implies that the high-density particles have induced favourable mixing conditions while traversing that section of the flow.

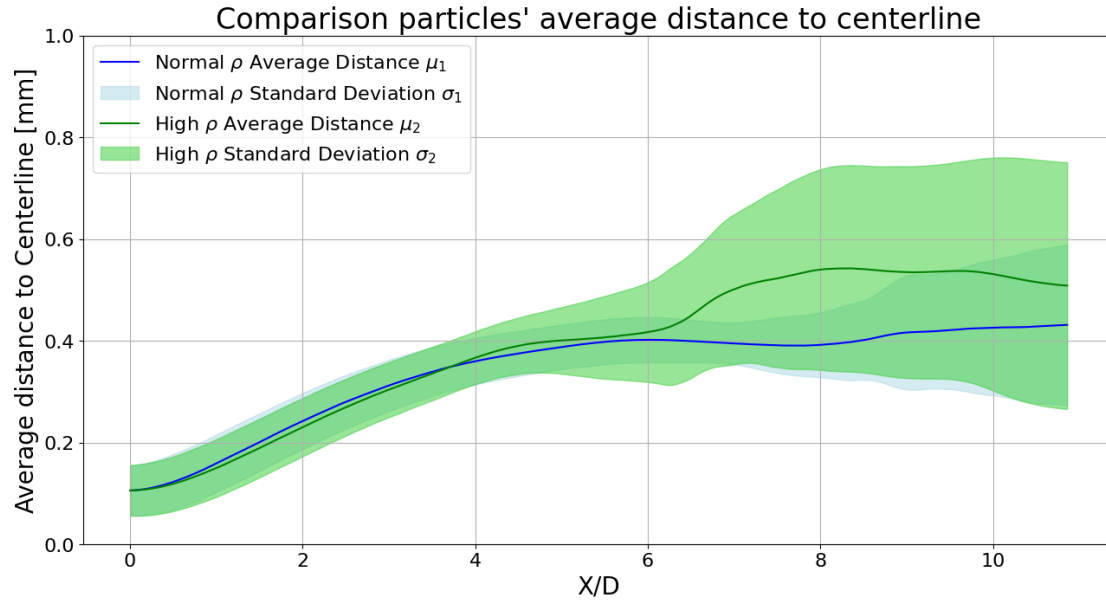


Figure 6.9: III-B Statistical comparison.

The overlay of statistical graphs corresponds with Figure 6.7. The gradual jump in average distance for the high-density simulation coincides with the location of the spread of trajectories. Noticeable is the fact that the net effect of mixing remains stable, but even decreases in the final stages of the model.

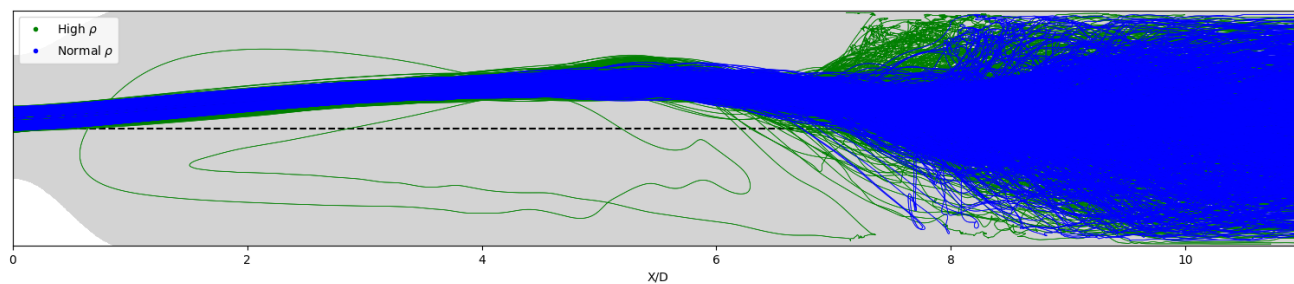


Figure 6.10: III-C 2D post-stenosis particle trajectory comparison.

Figure 6.10 highlights two distributions which resemble each other more closely. The onset of mixing still remains a bit further upstream for the high-density particles, but the locations have shifted towards each other, near lengthwise diameter 7. These two simulations share more similarities compared to III-B but the high-density simulations performs better in terms of final particle distribution. Two outlier high-density particles are caught in a major re-circulation zone and consequently don't exit the simulation via the outlet.

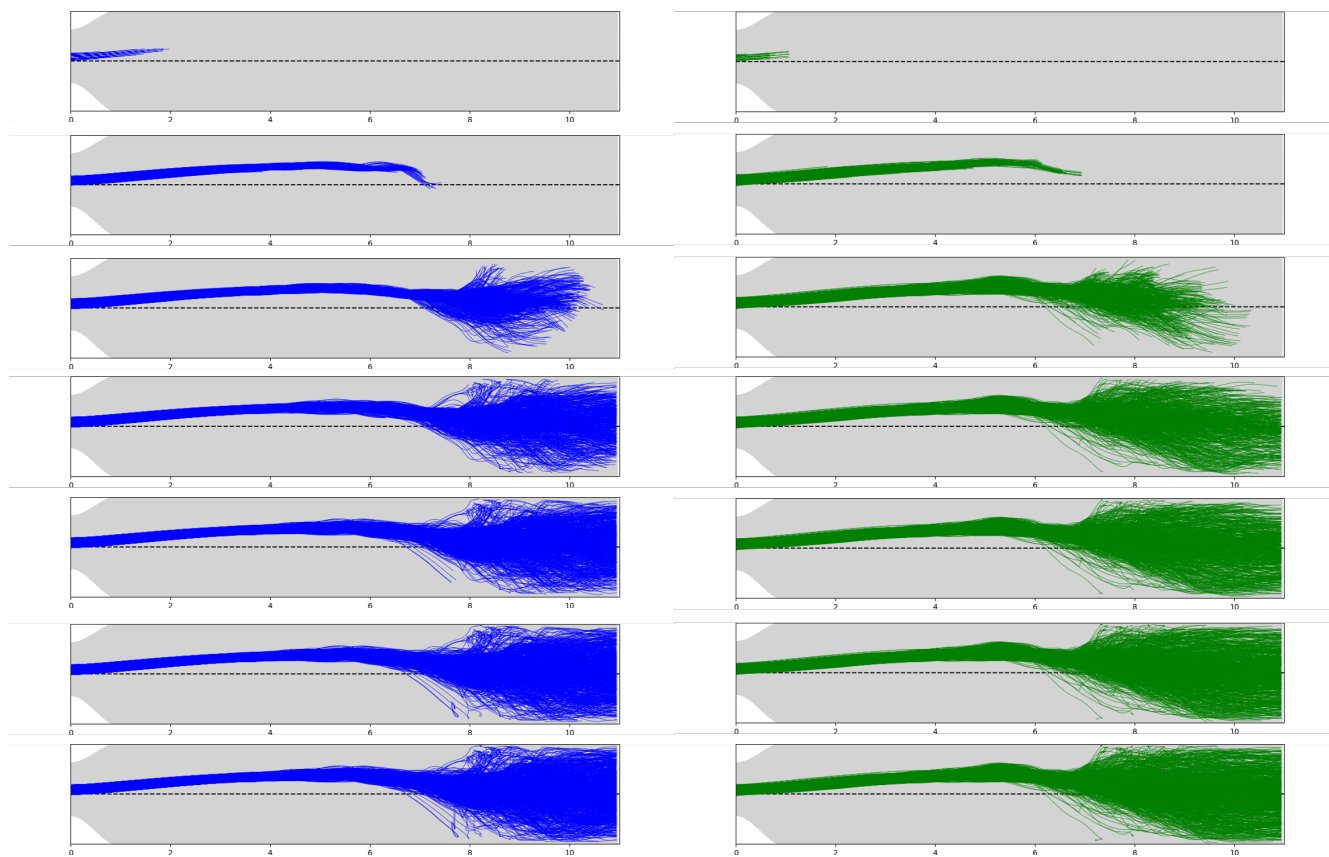


Figure 6.11: III-C snapshots of trajectories at similar time-steps.

Evolution of the trajectories in Figure 6.11 yields the conclusion that there is no significant temporal variation between the two simulations. One can observe that the particles near the peripheral sections of the lumen arrive later than the centrally distributed particles. An observation which has been made previously.

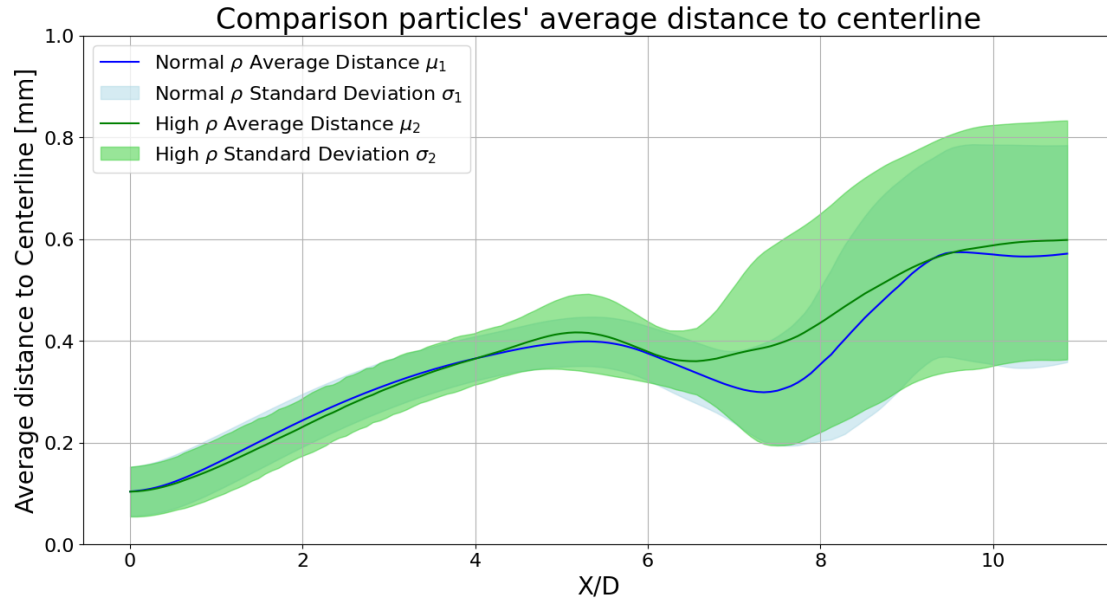


Figure 6.12: III-C Statistical comparison.

Inspection of the statistical plot, Figure 6.13, yields some extra insights. The increase in average distance for the normal density particles is more abrupt and less gradual than the high-density particles. This observation contradicts the very gradual line in the previous simulation.

The final simulation comparison, see Figure 6.13, continues the trend in which the normal density particles exhibit better mixing characteristics compared to the high-density simulations. The initiation point of the has shifted to the latter stages of the model, namely at around 9 lengthwise diameters. Given that this simulation coincides with the final turbulent period of the pulsating input, this checks out.

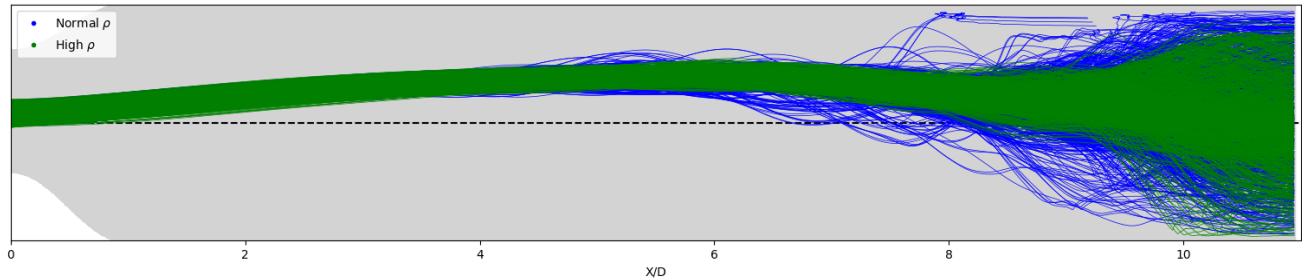


Figure 6.13: III-D 2D post-stenosis particle trajectory comparison.

The evolution graphs in Figure 6.14 display fairly similar behaviour up till the fourth time-step. During the fifth, for the normal density particles, several trajectories branch off from the main jet at around 6 lengthwise diameters. Behaviour which is absent in the high-density simulations. This is most likely induced by the differences in flow between the two simulations and improves the mixing behaviour of the normal density particles.

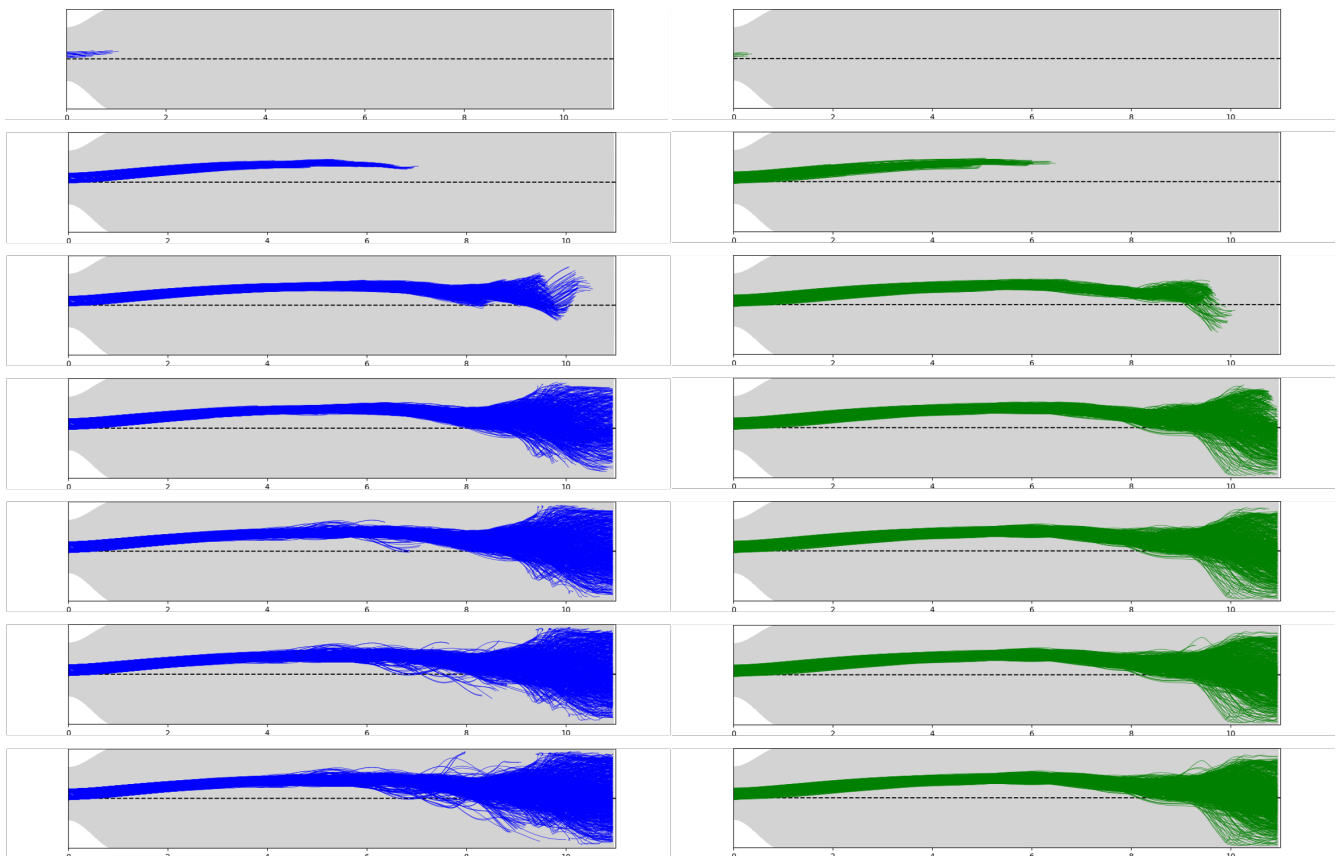


Figure 6.14: III-D snapshots of trajectories at similar time-steps.

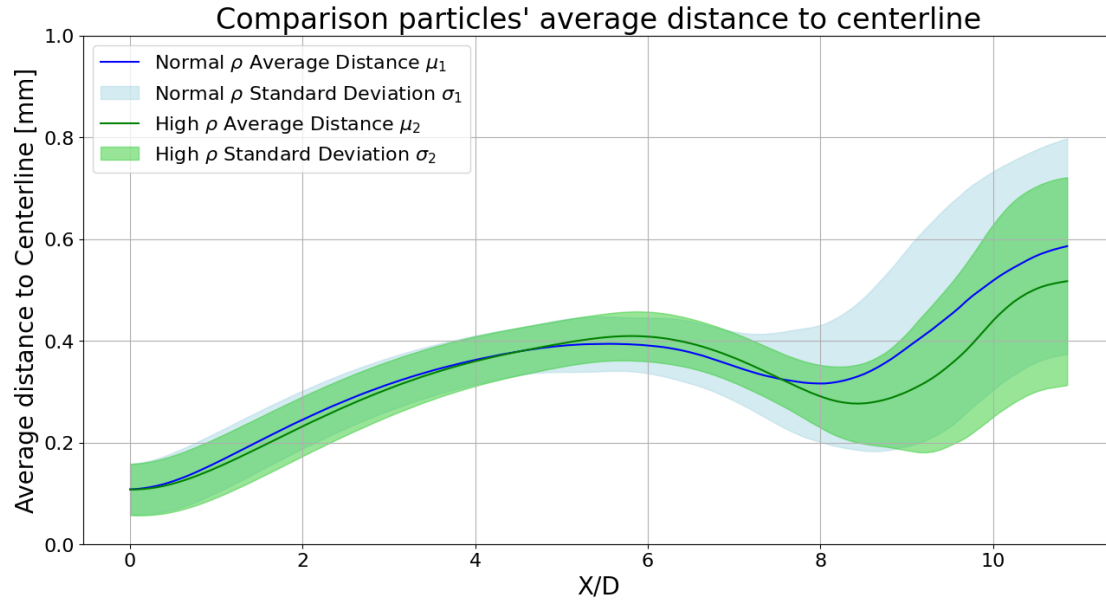


Figure 6.15: III-D Statistical comparison.

Figure 6.15 confirms the differences in mixing behaviour, mainly due to the fact that the particles in the high-density simulations adhere to the jet's trajectory. For both simulations, the limited length of the model itself prevents the capture of the full activity, which can be extracted from the slopes of both lines.

**Synopsis** *The effect of particle density on particle distribution and flow dynamics is significant.*

*An increased particle's density affects its inertia, translating in a slower throughput time and a decreased likelihood of acting as a passive tracer.*

*Even though a trend is observed which finds a higher density particle corresponding to better mixing performance at high turbulence intensity, no definitive relation can be established.*

## Chapter 7

# Implications of turbulence induced particle mixing

This chapter is dedicated to a more detailed elaboration of the simulations III-B, III-C and III-D. The goal of this chapter is to provide an in-depth analysis of the flow itself, coupling the suspected turbulent activity to the onset of particle mixing. This allows for a conclusive correlation between turbulent flow characteristics and particle mixing behaviour. The chapter consists of three main sections. An attempt at establishing a connection between the centerline flow velocity and the onset of particle mixing is made by analysing the temporal aspects of the flow in more detail. Secondly, Power Spectral Density (PSD) plots are employed, visualizing the Turbulent Kinetic Energy (TKE) along regular axial positions. Finally, a concise overview is which addresses the main research question and contains the essence of this research.

### 7.1 Fluid mechanical analysis

Along the centerline of the post-stenosis region of the model, probes have been placed at a regular interval to track all three spatial components of the fluid elements that happen to coincide with the given location. This allows for tracking of the total velocity magnitude during the entire duration of the simulation. The goal of this section is to connect the statistical graphs, given in Chapter 5 with this observed centerline flow velocity (CFV). This has been done for all three simulations in question (III-B, III-C, III-D), including a suspected laminar simulation (II-B) for comparison. Before the analysis commences, it should be noted that the CFV is not entirely representative of the flow in which particles are located. The centerline does not fully coincide with the jet containing the particles.

The plots which are utilized to visualize the centerline flow employ three axes. The left vertical axis measures the average distance to the centerline, identical to those in the statistical plots. The horizontal axis represents the x-distance in the model, post-stenosis. The right vertical axis is the basis for the CFV graphs and contains the time, from the beginning of the simulation up till the end. The absence of an axis for the magnitude of the CFV is justified, given that the purpose of this plot is to connect the changes in average distance to macroscopic characteristics of the CFV. The probes are placed at  $x = 8$ ,  $x = 12$ ,  $x = 16$  and  $x = 20$ .

Additionally, an attempt is made by using an alternative plot to quantify the onset of mixing, or at the very least, distinguish the simulations. A method is proposed where the trajectories of the particles are analysed. During the simulation, the velocity of the particles can be calculated by using the positions of particles in between time-steps. This allows for the decomposition of the velocity in individual spatial directions. The  $y$ - and  $z$ -direction are then used as metrics. If, a deviation in a particle's combined  $y$ - and  $z$ -direction is observed, which exceeds a certain threshold value, then a red dot is placed at that exact location. This is only done for the first time a particle exceeds this threshold. The  $x$ -location of

this instance is then registered and an average distance at which these initial deviations in trajectories take place is computed. This could be an indication of the onset of particle mixing, by employing the flow velocity as an indicator. The threshold value is set to 1/3 of the maximum radial deviation, which corresponds with the maximum deviation present in the simulation. The trajectories are colour codes based on their velocity magnitude.

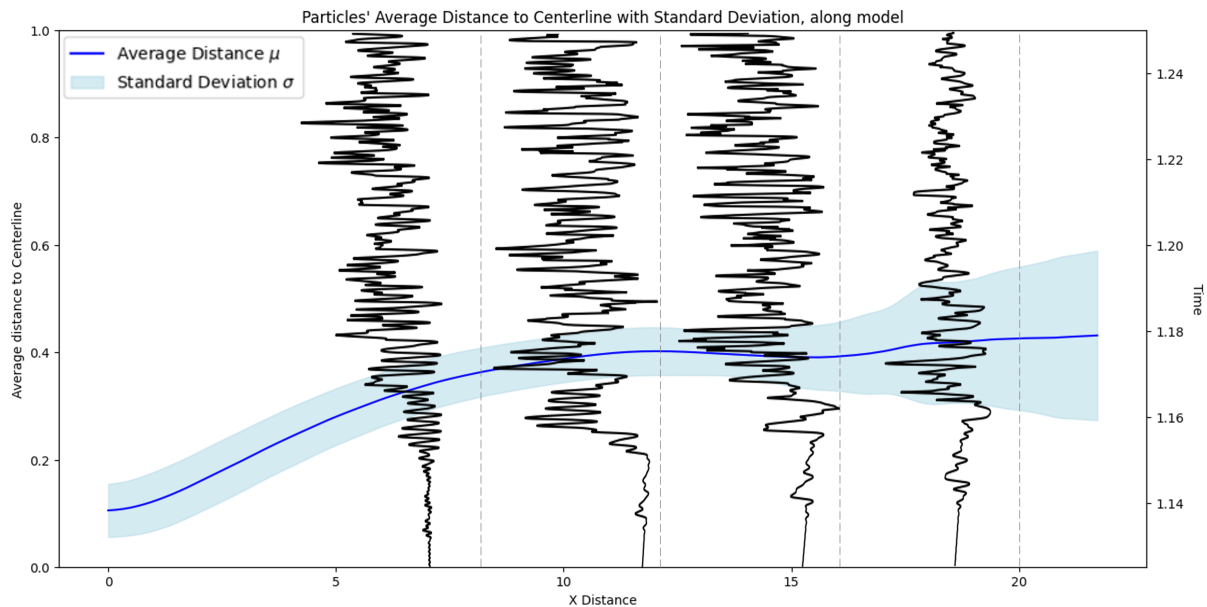


Figure 7.1: III-B Centerline velocity probes at interval locations.

For simulation III-B, the initiation of fluctuations in the flow is clearly visible. The transition to smooth, relatively smooth and suddenly chaotic behaviour is present in the first few centiseconds of the simulation. A general trend which sees the CFV drop while travelling further downstream the model can be observed.

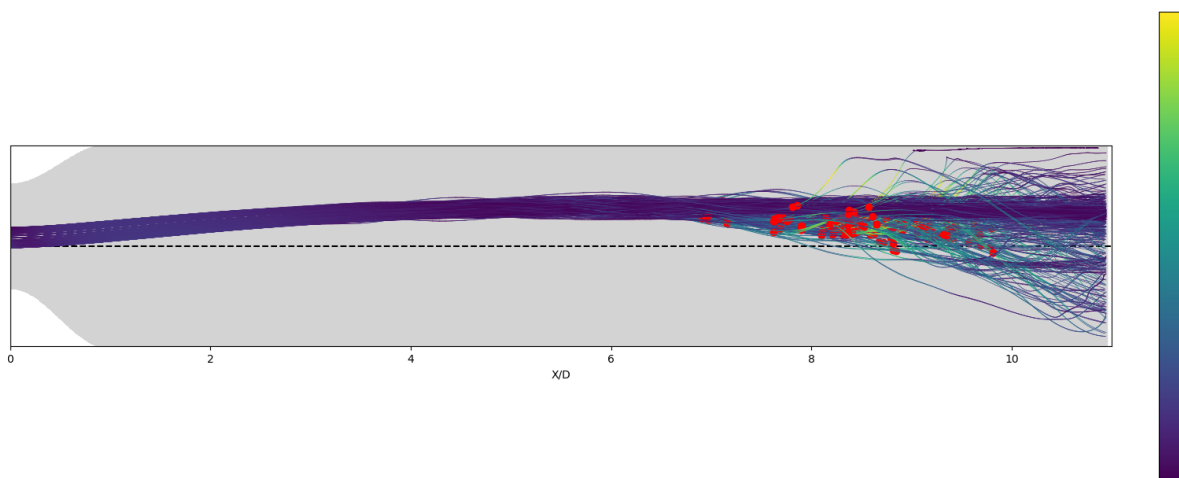


Figure 7.2: III-B Combined  $y$ - and  $z$ -velocity deviations, initial positions of deflection marked by red dots.

From Figure 7.2, an average  $x$ -position where the velocity threshold is exceeded is 8.03 lengthwise

diameters post stenosis is computed. This agrees with the visual analysis, as the region in which particle trajectories start to deviate from the jet's.

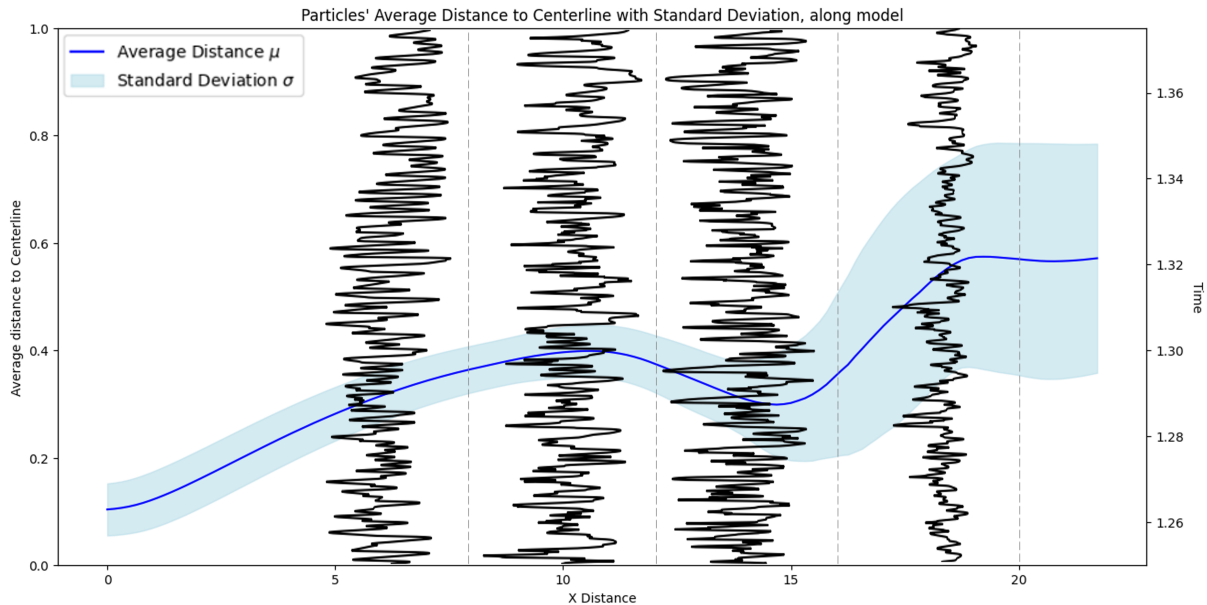


Figure 7.3: III-C Centerline velocity probes at interval locations.

Simulation III-C starts and end in the turbulent regime, something which could also be concluded from the cross-sectional plots in Subsection 5.2. Fluctuations decrease in magnitude in the final regions of the model.

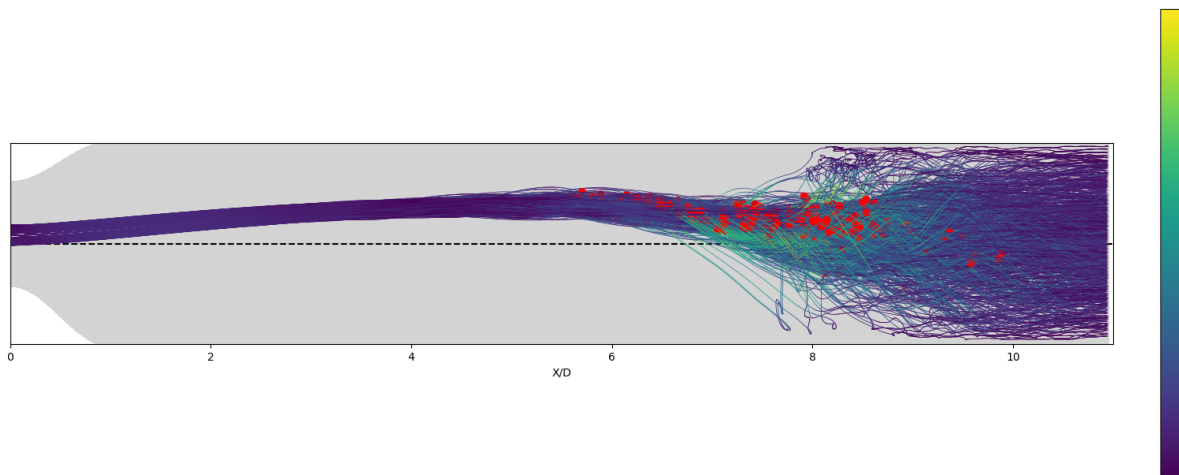


Figure 7.4: III-C Combined  $y$ - and  $z$ -velocity deviations, initial positions of deflection marked by red dots.

From Figure 7.4, an average  $x$ -position where the velocity threshold is exceeded is 7.47 lengthwise diameters post stenosis is computed. This is more than half a diameter upstream compared to III-B. This indicates a shift in turbulence onset towards the stenosis throat.

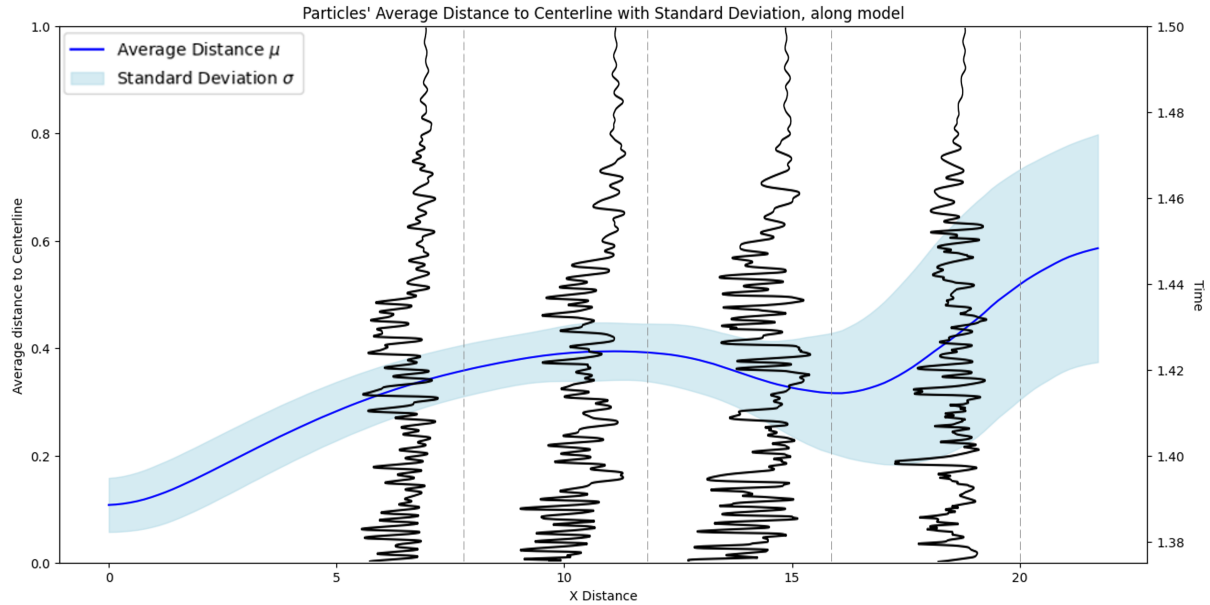


Figure 7.5: III-D Centerline velocity probes at interval locations.

Simulation III-C contains the last phases of turbulence in the flow. The chaotic fluctuations slowly die out and fade. Transition to laminar flow is observed for the final centiseconds of the simulation. Even though the intensity of the fluctuations remains generally lower compared to III-C, it still suffices for mixing behaviour.

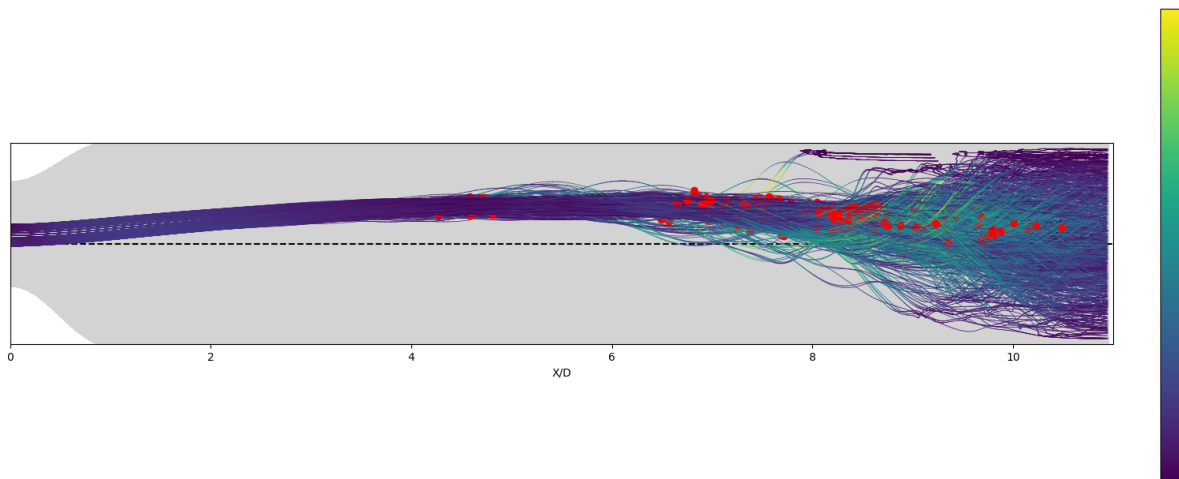


Figure 7.6: III-D Combined  $y$ - and  $z$ -velocity deviations, initial positions of deflection marked by red dots.

From Figure 7.6, an average  $x$ -position where the velocity threshold is exceeded is 7.68 lengthwise diameters post stenosis is computed. This value lies between simulations III-B and III-D. Its onset of mixing shifts further downstream and will eventually die out.

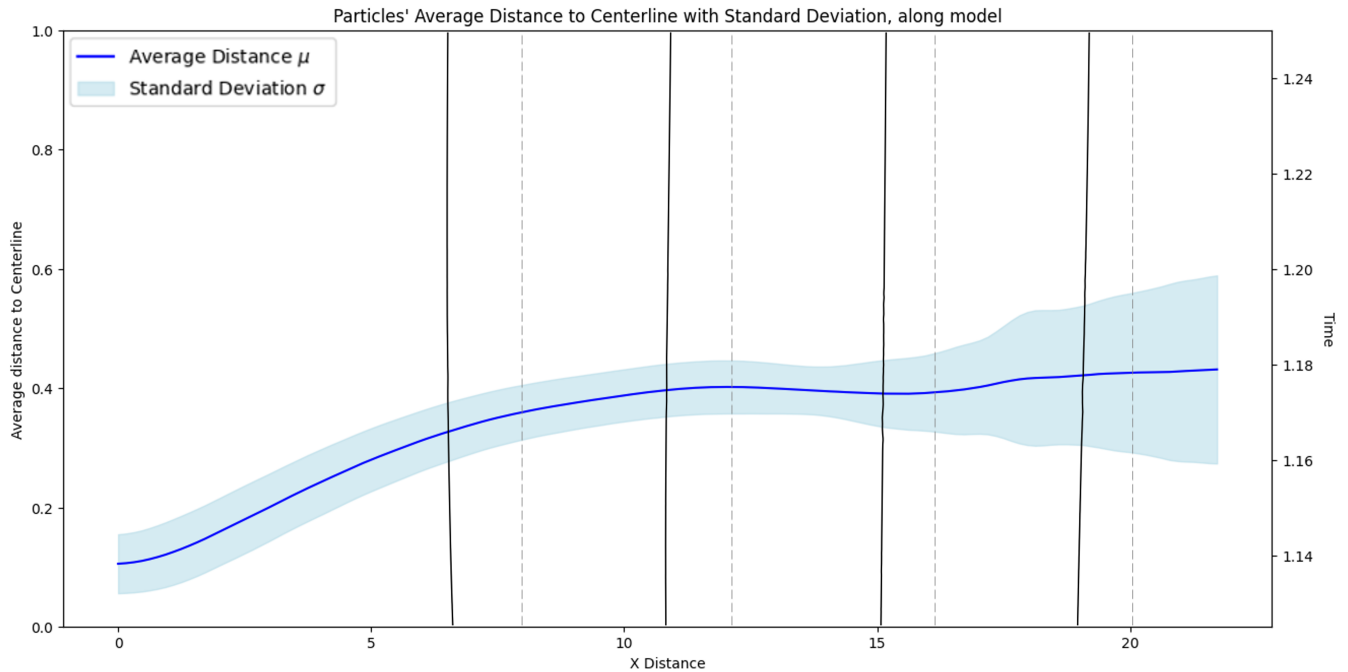


Figure 7.7: II-B Centerline velocity probes at interval locations.

Finally, for comparison, a similar plot is given for simulation II-B. As can clearly be extracted from the plot, no chaotic nature or flow fluctuations are present. This confirms the connection between laminar flow and the absence of particle mixing in the simulation. However, it is not possible to link the flow fluctuations to the onset of particle mixing. The breakdown of the flow of the jet remains uncaptured, given that it occurs above the centerline. The velocity decomposition method with the locations of trajectory deviations provides a rough indication, but as an average, it does not cover the dynamics of the jet breakdown.

## 7.2 Power Spectral Density

For the three simulations III-B, III-C and III-D, the plots in Chapter 5 imply the following hypothesis: the turbulent characteristics, induced by the flow, lead to the mixing of the microsphere particles. However, since the definition of turbulent flow is loosely defined, and no distinct quantified measure fully suffices to translate flow properties into the labels 'laminar' or 'turbulent', a different approach must be taken in order to classify this flow, and especially its (onset to) turbulence. Note that the statement of words here is selected carefully; There exists a transition (region) or onset rather than a sudden change in flow behaviour, which can be quite gradual [53].

In Figure 7.8, free flow along a flat plate is depicted. Note that this is a very different flow configuration than the one in question, but it clearly highlights the transitional region.

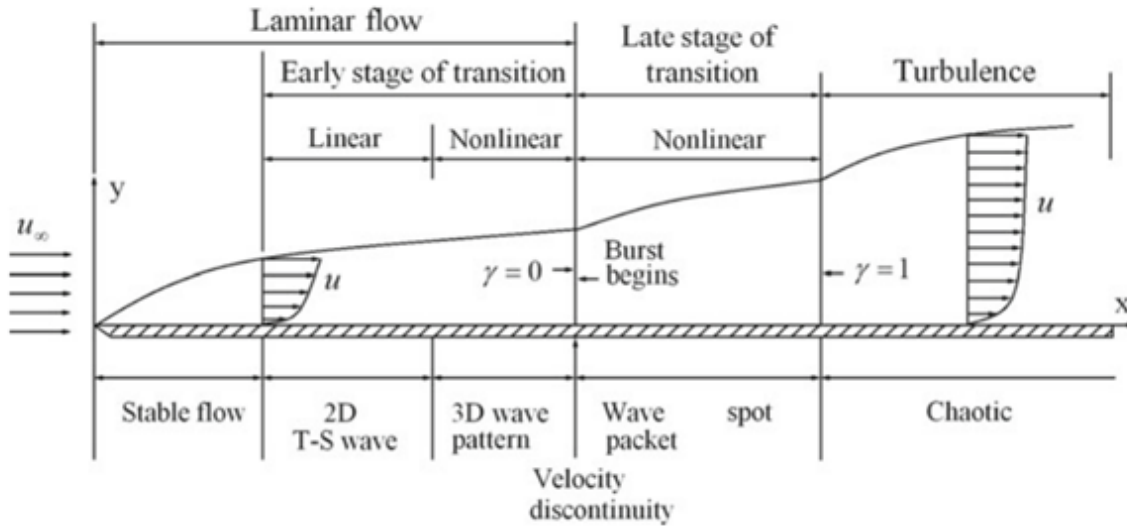


Figure 7.8: Boundary layer flow on a flat plate, developing from laminar- via transitional- to turbulent flow. Parameter  $\gamma$  is the intermittent factor;  $\gamma = 0$  indicates the onset of spike generation,  $\gamma = 1$  indicates the completion of turbulent transition [8].

In order to assess the turbulence in the flow, a PSD plot, in combination with overlaying axial flow profiles is used. A PSD plot captures any form of frequency of the to-be-analysed signal and plots its intensity. In this case, the TKE characterizes the power or intensity of the frequency.

The basis of this approach requires some theory. In essence, it is assumed that the observed flow ( $u(x, t)$ ), consists of a mean part ( $\bar{u}(x)$ ) and a fluctuation part ( $u'(x, t)$ ), see Equation 7.1. Triple decomposition according to Hussain & Reynolds, in which an additional term is included for the phase of the period is out of scope here [54].

$$u(x, t) = \bar{u}(x) + u'(x, t) \quad (7.1)$$

Two distinct parameters defining turbulence are now possible to compute: The Intensity of Turbulence ( $I$ ) and the parameter of interest, TKE ( $k$ ), which is defined in Equation 7.2, where the  $'$  superscript denotes the fluctuating parts of the decomposed velocity signal.

$$k = \frac{1}{2}(u_x'^2 + u_y'^2 + u_z'^2) \quad (7.2)$$

Turbulence is conceptualized from hereon as a collection of eddies of varying sizes. The largest eddies in the flow undergo instability and subsequently disintegrate, imparting their energy to smaller eddies. The energy transfer process, known as an 'energy cascade' continues iteratively as smaller eddies further dissipate energy to the smallest scales. Termination of the energy cascade occurs when the local Reynolds number reaches a sufficiently low value, at which point eddy motion starts to stabilize and molecular viscosity becomes predominant in dissipating kinetic energy. Hence, the characterization of turbulent flow hinges upon the distribution of turbulent kinetic energy across multiple length-scales. One can wonder how small this 'smallest' scale might be. To answer this, Soviet mathematician Andrey Kolmogorov proposed a mean-field theory in 1941 characterizing three parameters for this scale. The subsequent Kolmogorov-length, -time and -velocity scales are given below respectively:

$$\eta = \left(\frac{\nu^3}{\epsilon}\right)^{\frac{1}{4}}$$

$$\tau_\eta = \sqrt{\frac{\nu}{\epsilon}}$$

$$u_\eta = (\nu\epsilon)^{\frac{1}{4}}$$

With these parameters, it is possible to determine the scale at which turbulent kinetic energy is dissipated into heat using the variables kinematic viscosity ( $\nu$ ) and dissipation rate ( $\epsilon$ ).

Given the core insight of a transitional or turbulent flow consisting of a wide range of eddies and their consequent energies, one can start to decompose the flow into its distinct contributions. In the realm of signal analysis, the tool to transform a signal in time to a signal in temporal frequency is the (discrete) Fourier transform. A variation of the formula, Welch's periodogram is used for this analysis [55]. Figure 7.9, shows a typical evolution of energies over a range of frequencies.

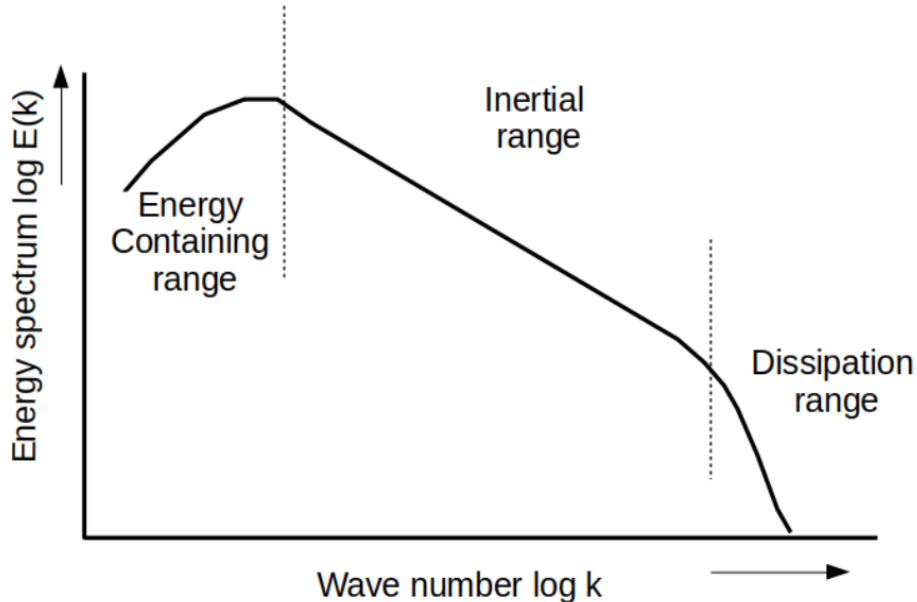


Figure 7.9: Energy spectrum  $E(k)$  as a function of the Wave number  $k = \frac{2\pi f}{c}$ . Note the log-log plot layout.

Three distinct regions can be identified; 1) The energy-containing range, the largest eddies supply energy to smaller eddies, absence of viscous dissipation. 2) The inertial (sub-)range, where a constant energy flux

across scales retains an equilibrium, with a constant power law of  $-\frac{5}{3}$ , which gives rise to the constant slope. 3) The dissipation range, in which viscous effects dominate over inertial and kinetic energy is converted into heat on the Kolmogorov scales. Comparison of the PSD of the to-be-analysed flows with the inertial range ( $-\frac{5}{3}$  slope), yields insights into the nature of turbulence in that flow.

The PSD plots, from here onwards plot the power of the signal  $[\frac{m^2}{s^2}]$  on the  $y$ -axis versus the Strouhal number  $Sr$  in [-] on the  $x$ -axis. The latter is defined as:

$$Sr = \frac{fL}{U} \quad (7.3)$$

Where  $f$  is the frequency in  $[Hz]$ ,  $L$  is the characteristic length, i.e. hydraulic diameter, in  $[m]$  and  $U$  is the flow velocity in  $[\frac{m}{s}]$ . This allows for non-dimensionalization.

Four post-stenosis locations are selected for the PSD analysis. These include the stenosis throat ( $x = 0$ ), the location just before the general turbulence onset ( $x = 12$ ), the location coinciding with the general onset of turbulence ( $x = 16$ ) and finally at a distance far downstream, in which turbulence might start to dissipate and die out ( $x = 20$ ).

Visual inspection of the flow itself implies that the stenosis throat experiences laminar flow with slight fluctuations. Some of these are caused by the particles traversing the throat. Figure 7.10a confirms this observation of predominantly laminar flow. For all four simulations, an immediate drop is observed at around  $Sr = 0.05$ , corresponding to laminar flow. A general trend can be extracted based on Figures 7.10b, 7.10c and 7.10d. This trend shows III-C possessing the most significant turbulent activity, followed by III-B and III-D respectively. The flow of II-B sticks out due to its consistent drop-off for the lower  $Sr$ -regime compared to flowclass III. The sporadic peaks in the higher  $Sr$ -regions can be attributed to noise.

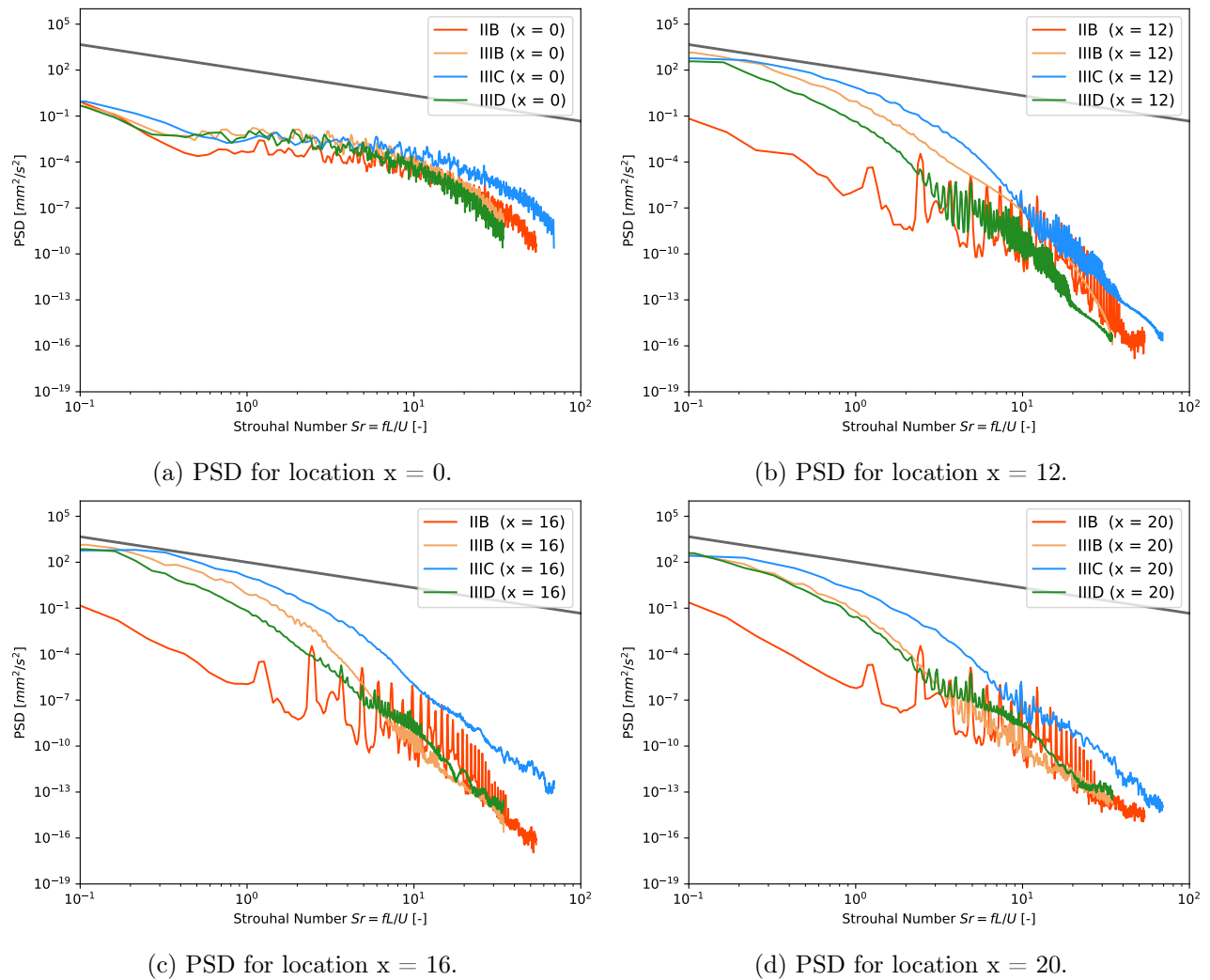


Figure 7.10: PSD plots for different locations post-stenosis.

### 7.3 Final overview

This final section is dedicated to combining all the aforementioned analysis into a single simulation overview. Linking these individual overviews allows for answering the research question, as stated in Chapter 1. Brief elaboration of the structure of each figure, see Figure 7.11. The first row depicts the 2D cross-sectional view of the post-stenosis region, containing the particle's trajectories. The dashed black line represents the centerline, at which, on a regular interval, probes are located. These are the black dots, spaced out uniformly, measuring the three spatial components of the flow velocity at those locations. As a result of this, the centerline flow velocity in row two is computed. The dashed line there represents the y-axis corresponding to zero magnitude. Similarly to Subsection 7.2, the power spectral density plots, see row three, provide the visual analysis of the turbulent kinetic energy. Finally, at the location of the probes, a snapshot is taken of all the particles'  $y$ - and  $z$ -locations when they reach a given  $x$ -coordinate. This results in the particle distribution as given in row four.

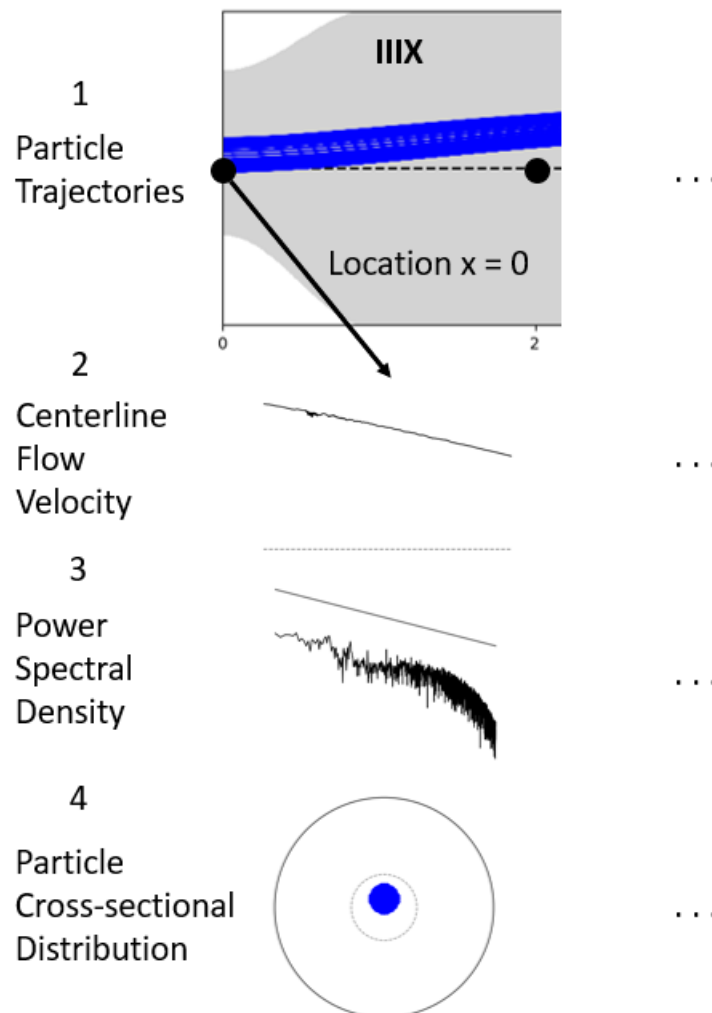
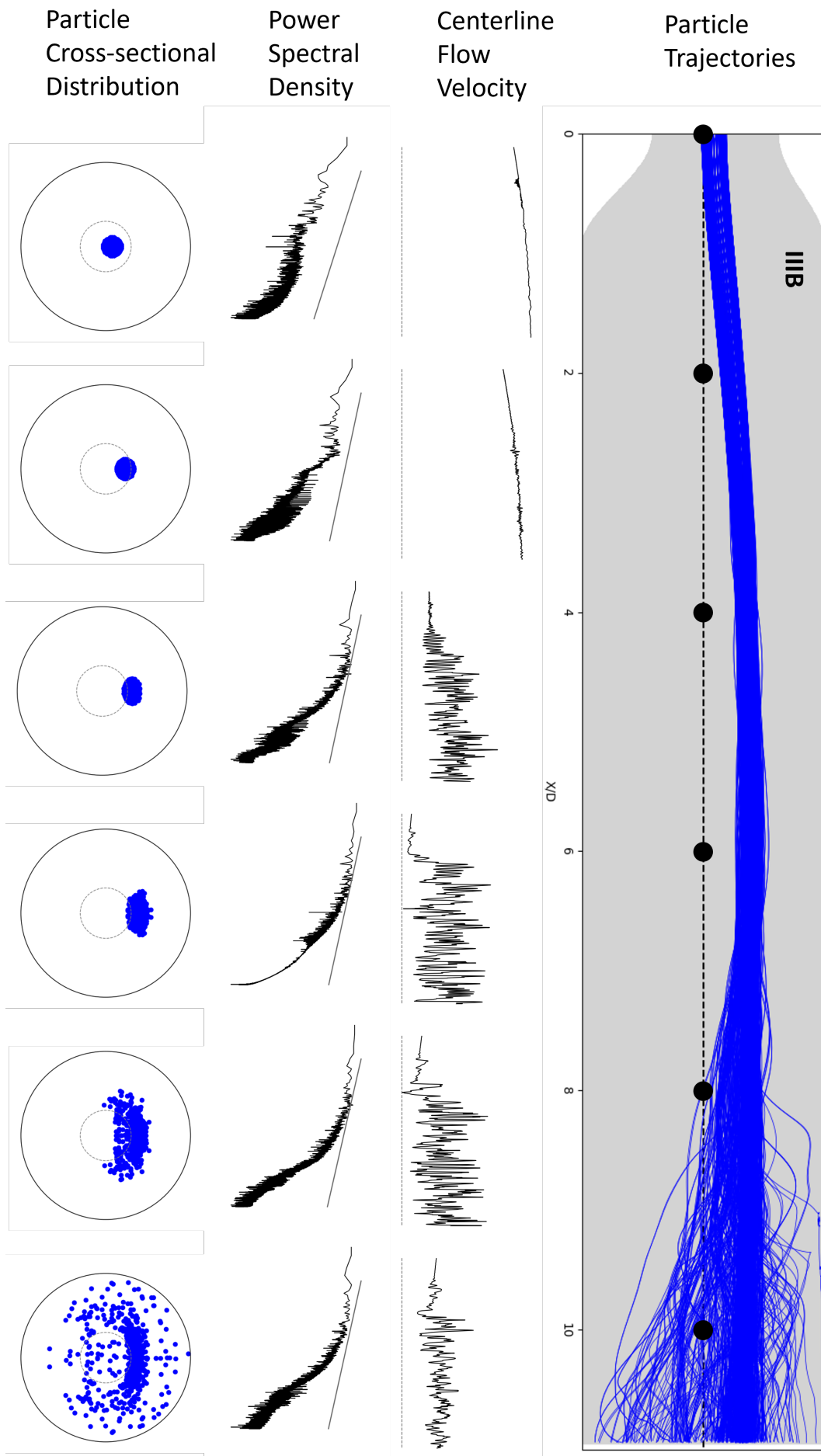
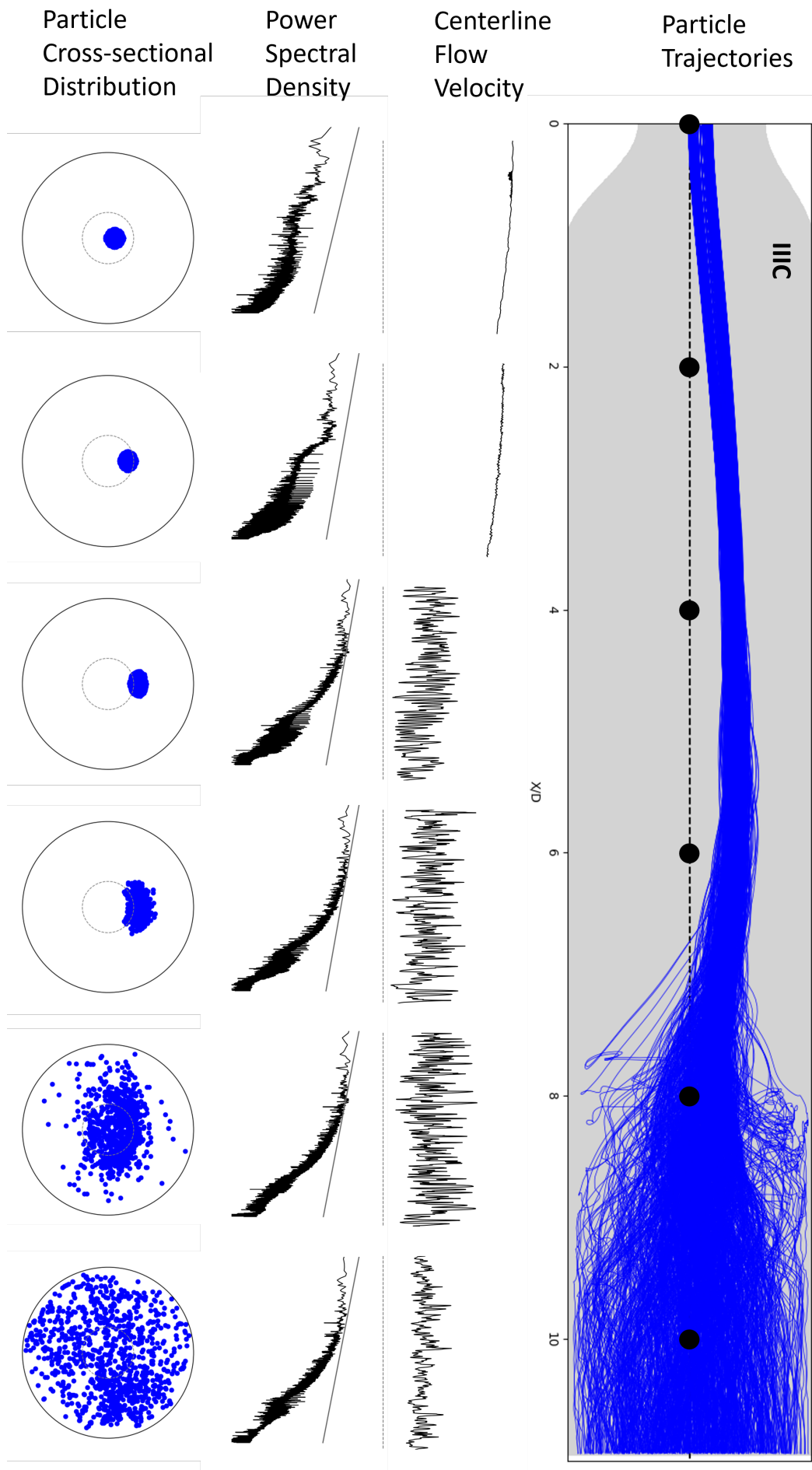
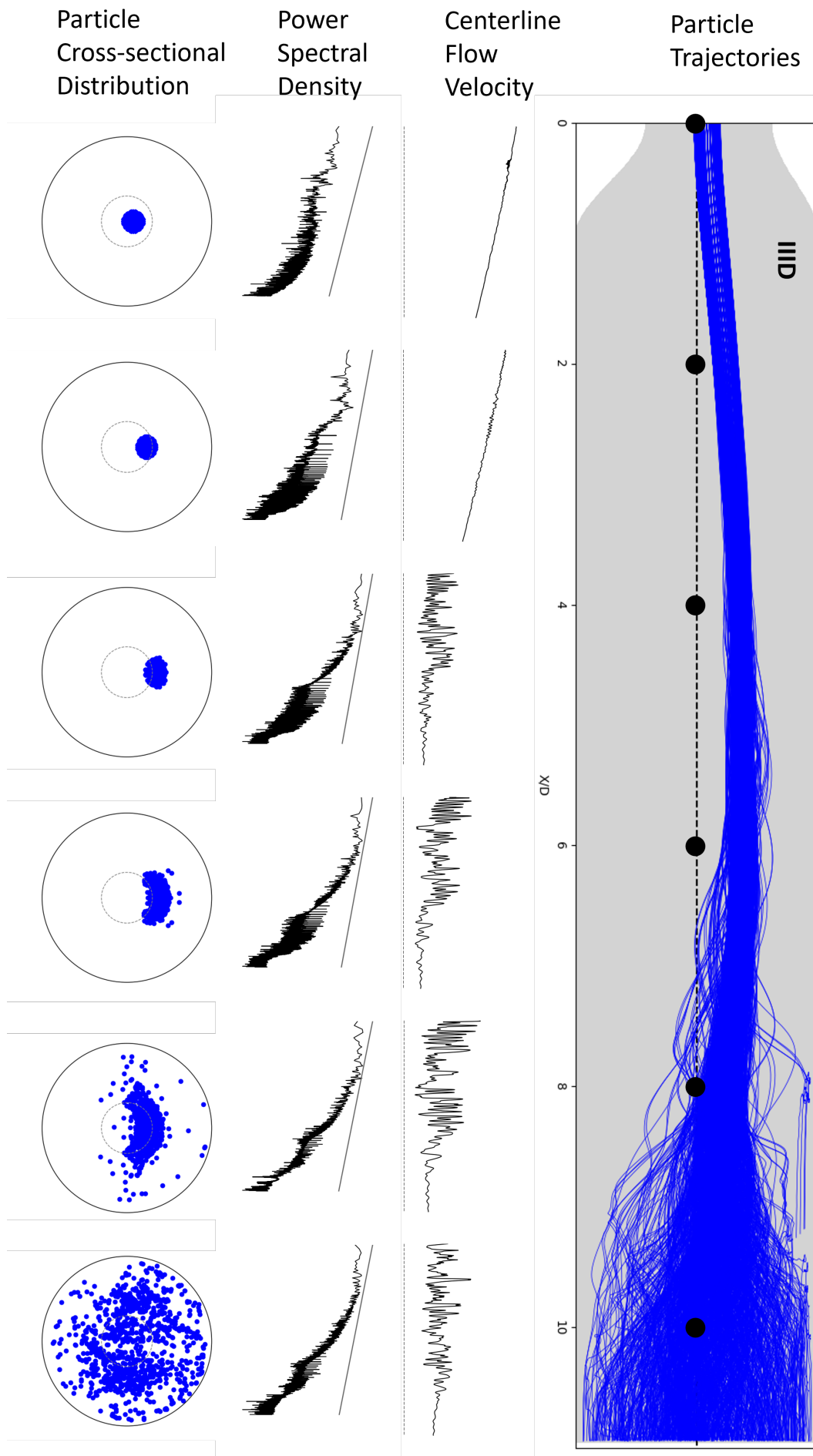


Figure 7.11: Guide for reading the final simulation overviews.

For readability, the overview is in landscape format, so rotate the pages 90 degrees counterclockwise. In addition to the three overviews, a statistical plot, containing four simulations (laminar II-B and flowclass III) is given in Figure 7.12.







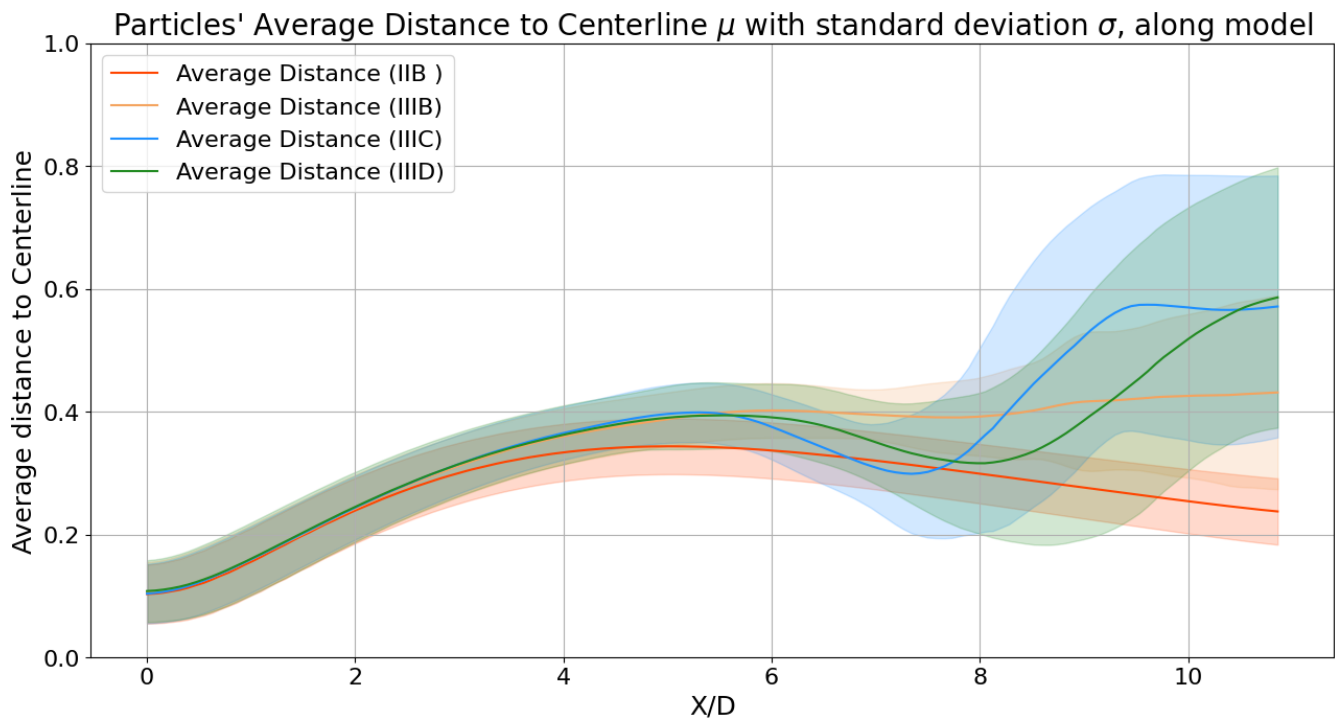


Figure 7.12: Combined overview average centerline distance for II-B, III-B, III-C and III-D.

**Synopsis** *This study demonstrates that turbulence can manifest in the hepatic artery under naturally occurring flow regimes due to a small onset of turbulence, as exemplified by the model's eccentric stenosis.*

*During the turbulent phase of the pulsating flow, particle mixing occurs, whereas in the laminar regime, no particle mixing is observed.*

*An increased intensity of the turbulent activity of the flow does not necessarily imply enhanced particle mixing behaviour.*

*The hypothesis that the most favourable time-interval regarding particle mixing is during the deceleration phase of the cardiac cycle seems to hold true.*

Note that it is highly advised to read the accompanying remarks in the discussion, see Section 8.1, before simply proceeding with the above-mentioned statements.

## Chapter 8

# Discussion, Conclusions and Recommendations

This final chapter aims to interpret the results found in the previous Chapter 7. The first section addresses degrees of uncertainty and limitations in the model and the research, as well as definite findings. With these obtained nuances and perspectives of the results, the proposed research questions stated in Chapter 1 are once again covered and answered in full detail in the second section. Finally, directions of further research are established, ones which could use this research among others as a groundwork to extensively examine the dynamics of particle mixing and distribution in the hepatic artery.

### 8.1 Discussion

Following the structure of the thesis, firstly, the validity of the model and its connection to the application are discussed. Secondly, the simulation set-up and its parameters are evaluated. Finally, the achieved results are discussed and interpreted.

**Model** The research aims to examine the particle mixing dynamics in the right hepatic artery under a number of time injection instances. As with every comparison to real-life applications, and especially considering the human body as a variable component, this comes inevitably at the expense of simplifications and concessions. Granted this observation, an effort is made to balance these losses in accuracy, precision, and realism to the available resources in time and effort. The model itself is one of the more significant simplifications of this research.

The use of a circular pipe for the right hepatic artery is justified given the similarities in shape and size of the vessel. It is the most basic geometry to which the artery can be condensed to while retaining a certain degree of realism. A patient's hepatic artery deviates in a number of aspects of the model. Its intricate shape, fitting it in the composition of the liver vasculature. Lumen walls are not smooth but rather intricate and rough surfaces, which also depend on the patient. Regarding the dynamics of the artery itself, the model approaches the artery as a rigid and stiff vessel, while in reality, the artery has a certain compliance and is able to position and shape itself in order to adapt to the varying inflow conditions. This motion has an effect on the flow contained inside the hepatic artery.

The eccentric stenosis acts as an onset of turbulence, which mimics the intricate flow conditions as blood enters the hepatic artery. However, this inflow of blood is non-steady and most likely possesses different turbulent characteristics compared to the prescribed inlet boundary condition in the model. Concerning the remaining BCs in the model, their applicability might deviate from reality. Now, given these discrepancies between the model and reality, let's analyse on their influence on the final results.

The use of a circular smooth pipe as a vessel is conventional when studying biophysical arterial flows in

literature. An alternative approach of analysing one patient's hepatic artery, obtained by medical imaging techniques would limit the research to a single patient-specific case and amounts to the loss of generality amongst other challenges. Analysis of multiple patient's specific arteries was simply out of the scope and not required for this research. The current approach using a circular pipe allows for a more general conclusion, one that can be tested against patient specific models.

The surface roughness is to some degree accounted for by the onset of turbulence. Major geometric deviations caused by an irregular lumen and surface coarseness are not captured by the model. Altogether, it is unclear to what extent this influences particle mixing.

Regarding the stiffness of the model, there is basically one costly solution to the aforementioned absence of elastic behaviour. The use of a Fluid Structure Interaction (FSI) model, allows for incorporating the dynamic behaviour of the artery. Consequently, a new mesh has to be generated after the displacement of the vessel's walls, attributing to a significant increase in computational time and model complexity. The most likely benefit from this approach is the more accurate data near walls, which is of lesser importance in this study. It could however provide information about how this movement of the artery influences the lumen flow itself, establishing a connection between arterial dynamics and introduction of non-laminar flow behaviour herein.

The inflow of blood at the inlet BC is coupled to the cardiac cycle, so even with reduced accuracy, it still adheres to the pulsatile nature of the turbulence, which is also the case in a patient. The constructed flowclasses serve as a lower and upper bound of Reynolds numbers observed entering the hepatic artery. However, uncertainty remains in the exact inflow conditions which are again, patient-specific.

One important aspect of the model which could have been accounted for is the length of the post-stenosis region. Especially during the deceleration phase of the cardiac cycle, the statistical graph indicates that the mixing behaviour has not yet terminated, but particles simply reach the outlet BC and exit the model before any more mixing takes place. A longer model would have provided this information, in addition to an answer to the question if the transition from turbulent to laminar flow influences the trajectories of the particles further downstream. However, it should also be noted that the hepatic artery is not infinitely long and hence has limited length to accommodate mixing before the first bifurcation.

**Simulation** For the simulations, a distinction is made between flow properties and temporal aspects. Confidence in the physical parameters of the flow, e.g. viscosity and density itself is high. The fluid is modelled as BMF, which imitates the non-Newtonian properties of blood. The shear thinning effects depend on the vasculature's dimensions, however, for the hepatic artery, the current parameters suffice to simulate blood flow.

Apart from this viscosity-related parameter, the composition of blood itself plays a crucial role. The current set-up of the simulation does not allow for intricate hemodynamics components.

Regarding the particles, similar confidence in physical parameters is present, given that the values are directly extracted from literature. Variation in individual size and mass is negligible. The release mechanisms of the particles in the catheter are quite niche. The uniform distribution and the simultaneous release of all particles with identical velocity is an idealized scenario. The exact influence of the particle release method is not investigated. As mentioned previously, the catheter itself is subject to elaborate analysis regarding the type, angle, position, etc. which is not covered in this research.

Introduced by the eccentric stenosis, the jet of fluid exiting the throat has a large influence on the particles' trajectories. The upward deflection is inherent to the simulation and is not present in the hepatic artery. Therefore, the phase between the particle release instant and the onset of turbulent mixing is purely necessary in terms of modelling but not present in real life.

The simplified cardiac cycle allows for great comparison and provides distinction between the phases. With increasing flowclass, a decreasing throughput time of particles has been observed, with the highest flowclass only attributing to a twentieth of a second. Due to the current particle release set-up, the flow at the release instants is not representable for the particle mixing itself. More particle release moments would

have aided in establishing trends between the simulations. However, any particle release moment after half a cardiac cycle would not have resulted in an outcome with any mixing behaviour due to the absence of turbulent characteristics. The choice to use a single second as a restart, rather than a number of cycles is found to be justified. During the second phase of the cardiac cycle, much, if not the majority of the turbulent activity is washed away because of the laminar regime. The cycle is expected to be reasonably sufficient to analyse as a standalone system. Nonetheless, for the analysis of the simulations, a full cycle should be captured for the sake of completeness in future research.

Zooming in on the technical aspects of the simulations itself, several noteworthy comments can be made. The sampling of the data regarding CFV is now done at every tenth time-step and for the visual cross-sectional overview, every eighth of one second. In retrospect, the number of datapoints for the CFV is acceptable, but more VTK files would have provided some visual cues regarding the onset and offset of turbulent activity.

As mentioned previously, the CFV is conventionally sampled at the centerline. Given that due to the set-up of the model, the centerline does not cover the onset of turbulent activity, an opportunity is missed to fully capture the flow characteristics of the turbulence. An additional line of probes coinciding with the trajectory of, or close to, the jet would have allowed for this alternative approach, which would have been able to conclusively link the flow with the particles.

Subsequently, the use of three particle release instants has been valid for distinguishing the simulations. Nevertheless, three data points are insufficient to construct a general trend and thus a definitive answer to sub-question three. Partially attributing here, are the discrepancies between the high- and low-density particle simulations.

**Results** In order to assess the results of the simulations in this thesis, a number of quantitative as well as qualitative metrics have been employed. The use of simple statistical measures in order to quantify the mixing behaviour is valid, and a more thorough analysis is not required given the goal of the research.

Assessment of the mixing behaviour of particles has mainly been done in 2 dimensions. The distribution over a certain cross-section is utilized as a base, with no regard for the 3D configuration of the particles. This is found to be irrelevant to this research but should be investigated in consultation with experts on the clinical aspect of radioembolization.

It should be stressed that the high-density particle simulations are merely a pure fluid mechanical problem. The difference in density is substantial, which translates into a dissimilar Stokes number and thus altered trajectories. Interpretation of these results with respect to radioembolization is unjustified.

This thesis aims to connect flow in a model to the application of radioembolization, and the question arises of how accurate this comparison is, given the aforementioned marginal notes. Caution should be exercised by extrapolating the results from the fluid mechanical analysis to the treatment of radioembolization. In a similar fashion, the simulation results can not simply be translated into recommendations for practices in the clinic.

Finally, regarding the process itself, several remarks can be made, which have to be addressed. During the earlier stages of developing the model, a significant amount of CPU hours have been burned in an inefficient manner. The occasional trial-and-error approach on Snellius does not agree with the scientific method and could have been prevented by utilizing the available CPU time more carefully. In the earlier stages of the research, several issues with the model, software or the use of the supercomputer have been encountered and eventually resolved. This strengthened the understanding of the research on one hand, but attributed to unplanned downtime and increased computational costs on the other.

## 8.2 Conclusions

In order to recapitulate the thesis and answer the main research question posed in the introduction of the research, the sub-questions are addressed one by one.

### **Can flow leave laminar regime in the hepatic artery?**

The constructed computational model, represented as an eccentric stenosed pipe has been utilized as the foundation for the simulations. Flow conditions derived from the literature have been imposed on the model to represent distinct potential flow regimes within the hepatic artery. These range from  $Re = 160$  to 700, based on the maximum flow velocity across the primary vessel diameter. For the lower  $Re$ , streamlines are parallel and flow remains laminar. Flow has been observed to depart from the laminar regime in the flowcase with the highest induced flow velocity. Turbulence onset occurs just prior to the peak of the simplified cardiac cycle and dissipates during the deceleration phase. The turbulence intensity is considerable, leading to vortical motion downstream of the stenosis.

### **Does this non-laminar regime result in better mixing?**

The introduction of the particle release allows for the analysis of the subsequent flow-induced particle trajectories. In both laminar flowcases, no particle mixing is observed and particles remain in trajectories coinciding with streamlines. The introduction of turbulent flow characteristics in the highest flowcase significantly affects the particles, which act partially as passive tracers, due to their Stokes number. The onset of turbulent activity downstream of the stenosis seems to coincide with the initiation of particle dispersion. Particles disperse throughout the entire cross-sectional area in all radial directions.

### **How does the injection timing influence the mixing, if at all?**

Three distinct particle release instances during the cardiac cycle were selected to investigate the temporal influence of injection. Significant differences have been observed, indicating that the release instance is an influential parameter. For the first particle release moment (B), mixing behaviour is the least significant. Particle dispersion initiates late in the simulation, with the onset occurring far downstream. The final particle distribution is symmetric but eccentric. For the second particle release moment (C), the mixing is extensive, with the earliest onset and an overall symmetric and evenly distributed pattern. For the final particle release moment (D), the onset of mixing occurs moderately downstream, with the most profound mixing during the deceleration phase of the simplified cardiac cycle. The mixing behaviour has not ceased by the end of the model. This instance shows the best overall mixing according to the employed statistical metrics, with a symmetrical and evenly spaced final distribution. The influence of particle release is hereby demonstrated. However the number of simulations is insufficient to conclusively determine the certain optimal injection phase of the cardiac cycle.

### **How can the possibility of turbulence in the lumen of the hepatic artery explain mixing of microspheres with the blood and consequent efficacy of the procedure?**

During this thesis, an attempt has been made in order to visualize the particle distributions and henceforth find underlying mixing mechanics. It is clear that the flow departs from the laminar regime within physiological Reynolds number. Consequently, the observed onset of turbulence facilitates particle mixing. This is among other factors time-dependent, given a simplified cardiac cycle. The deceleration phase of this cycle seems to favour optimal mixing conditions. In the future, lumen flow should be scrutinized to confirm the possibility of turbulence and mixing.

### 8.3 Recommendations

With the conclusion section completed, which highlighted definitive results as well as unknowns, the latter is elaborated upon in this section. A distinction is made between four fields all contributing to this research. These include: Fluid mechanics, Numerics, Computing and Physiology.

**Fluid Mechanics** Numerous qualitative research directions can be explored regarding the fluid mechanical aspects of the research. The analysis can benefit from an increased amount of Reynolds numbers, further detailing the flowclasses. This would enable to find the critical  $Re$  at which behaviour departing from laminar flow is introduced in this particular system. Another inherent parameter is the particle injection speed/manner, which should be investigated in more detail. Previous research has shown the importance of the particle injection velocity, with discrepancies between 2D and 3D flow configurations. When stepping out of the scope, this topic borders research directions like catheter- type/position/angle.

**Numerics** Summarizing, LBM is found to be very suitable for capturing the important flow dynamics in this research. Especially regarding the capture of base turbulence in the model, which allows for a confident analysis of the particles' kinematics and their trajectories. The use of conventional CFD methods might either choose to ignore the turbulent characteristics for given  $Re$  flows or has to introduce a turbulent scheme. Altogether, the main takeaway here is that for future research, when analysing biophysical flows with low to moderate  $Re$ -values, non-laminar behaviour can manifest and the presence of it cannot simply be ignored.

**Computing** High-performance computing has been the backbone of the study, allowing for very high temporal and spatial resolutions for the highest flowclasses. If given more computational resources, a longer domain post-stenosis is a simple yet effective addition. This could conclusively address the evolution of the particle trajectories after the turbulence has died out. If the need arises to study the deceleration phase of the cycle more carefully, an increased amount of injection time-instances is advised in the first half of the cardiac cycle.

**Physiology** As mentioned in Section 8.1, several factors related to the model and the simulation itself should be investigated in more detail. These include the fluid-structure interaction, which can be implemented with an FSI. Additionally, regarding the pulse signal itself, which acts as a simplified cardiac cycle, more realistic pulses will mimic the rhythmic and pulsatile nature of the system more accurately. Moreover, the working fluid is increasingly important with the introduction of particles. Physical factors such as the non-Newtonian behaviour and the true composition of blood are aspects which should be studied.

The use of the lattice Boltzmann solver Musubi has been a very suitable tool for this research. A direct translation between the results of this thesis and the clinical implications for physicians can simply not be made with the current simulations. However, a small step has been made to the understanding of the complex fluid mechanical aspects of radioembolization.

# Bibliography

- [1] USA Oncology Centers. Radioembolization (Y-90). [Online]. Available: <https://www.usaoncologycenters.com/liver-cancer/treatments/radioembolization-y-90/>
- [2] Terumo Interventional Systems. 12 Personalized Treatment of Liver Cancer Using Microscopic Radioactive Beads. [Online]. Available: <https://www.terumo.com/technology/stories/12>
- [3] American Cancer Society. Schematic Liver Vasculature. [Online]. Available: <https://www.cancer.org/cancer/types/liver-cancer/treating/embolization-therapy.html>
- [4] R. E. Klabunde. Cardiovascular Physiology Concepts. [Online]. Available: <https://cvphysiology.com/heart-disease/hd002>
- [5] APES.OSDN.IO, “Adaptable poly-engineering simulator (apes),” Online, 2023, available: <https://github.com/apes-suite>.
- [6] WhiteTimberwold, “Schematic drawing of an octree, a data structure of computerscience,” Online, 2010, available: <https://commons.wikimedia.org/wiki/File:Octree2.png>.
- [7] Terumo Interventional Systems. ProGreat Microcatheter System. [Online]. Available: <https://www.terumo-europe.com/en-emea/products/progreat%E2%84%A2-micro-catheter-system?TermStoreId=70aa3b4e-82ed-47d3-b1dc-9d7951d9228f&TermSetId=2fa1bbfb-d558-4262-9605-3c31f742e996&TermId=e6682e18-e528-471b-8d10-1f8cfe85cca8>
- [8] H.-S. Dou, *Stability and Transition of Boundary Layer Flow*. Singapore: Springer Singapore, 2022, pp. 159–206.
- [9] A. Saini, A. Wallace, S. Alzubaidi, M. G. Knuttinen, S. Naidu, R. Sheth, H. Albadawi, and R. Oklu, “History and evolution of yttrium-90 radioembolization for hepatocellular carcinoma,” *Journal of Clinical Medicine*, vol. 8, no. 1, 2019.
- [10] R. J. Lewandowski and R. Salem, “Yttrium-90 radioembolization of hepatocellular carcinoma and metastatic disease to the liver,” *Seminars in Interventional Radiology*, vol. 23, no. 1, p. 64 – 72, 2006.
- [11] M. L. Smits, J. F. Nijsen, M. A. van den Bosch, M. G. Lam, M. A. Vente, W. P. Mali, A. D. van Het Schip, and B. A. Zonnenberg, “Holmium-166 radioembolisation in patients with unresectable, chemorefractory liver metastases (hepar trial): A phase 1, dose-escalation study,” *The Lancet Oncology*, vol. 13, no. 10, p. 1025 – 1034, 2012.
- [12] C. G. Radosa, J. C. Radosa, S. Grosche-Schlee, K. Zöphel, V. Plodeck, J. P. Kühn, J. Kotzerke, and R.-T. Hoffmann, “Holmium-166 radioembolization in hepatocellular carcinoma: Feasibility and safety of a new treatment option in clinical practice,” *CardioVascular and Interventional Radiology*, vol. 42, no. 3, p. 405 – 412, 2019.

- [13] C. van Roekel, N. I. Harlianto, A. J. Braat, J. F. Prince, A. F. van den Hoven, R. C. Bruijnen, M. G. Lam, and M. L. Smits, “Evaluation of the safety and feasibility of same-day holmium-166 -radioembolization simulation and treatment of hepatic metastases,” *Journal of Vascular and Interventional Radiology*, vol. 31, no. 10, p. 1593 – 1599, 2020.
- [14] M. Stella, A. J. A. T. Braat, R. van Rooij, H. W. A. M. de Jong, and M. G. E. H. Lam, “Holmium-166 radioembolization: Current status and future prospective,” *CardioVascular and Interventional Radiology*, vol. 45, no. 11, p. 1634 – 1645, 2022.
- [15] E. G. Giannini, F. Farinati, F. Ciccarese, A. Pecorelli, G. L. Rapaccini, M. Di Marco, L. Benvegnù, E. Caturelli, M. Zoli, F. Borzio, M. Chiaramonte, and F. Trevisani, “Prognosis of untreated hepatocellular carcinoma,” *Hepatology*, vol. 61, no. 1, p. 184 – 190, 2015.
- [16] R. Hickey, R. J. Lewandowski, T. Prudhomme, E. Ehrenwald, B. Baigorri, J. Critchfield, J. Kallini, A. Gabr, B. Gorodetski, J.-F. Geschwind, A. Abbott, R. Shridhar, S. B. White, W. S. Rilling, B. Boyer, S. Kauffman, S. Kwan, S. A. Padia, V. L. Gates, M. Mulcahy, S. Kircher, H. Nimeiri, A. B. Benson, and R. Salem, “90y radioembolization of colorectal hepatic metastases using glass microspheres: Safety and survival outcomes from a 531-patient multicenter study,” *Journal of Nuclear Medicine*, vol. 57, no. 5, p. 665 – 671, 2016.
- [17] C. van Roekel, R. Bastiaannet, M. L. J. Smits, R. C. G. Bruijnen, A. J. Braat, H. W. de Jong, S. G. Elias, and M. Lam, “Dose–effect relationships of 166ho radioembolization in colorectal cancer,” *The Journal of Nuclear Medicine*, vol. 62, pp. 272 – 279, 2020.
- [18] J. Samuelsson, O. Tammisola, and M. Juniper, “Breaking axi-symmetry in stenotic flow lowers the critical transition reynolds number,” *Physics of Fluids*, vol. 27, no. 10, 2015.
- [19] K. Jain, “The effect of varying degrees of stenosis on transition to turbulence in oscillatory flows,” *Biomechanics and Modeling in Mechanobiology*, vol. 21, no. 3, p. 1029 – 1041, 2022.
- [20] M. Lafortune and H. Patriquin, “The hepatic artery: Studies using doppler sonography,” *Ultrasound Quarterly*, vol. 15, no. 1, p. 9 – 26, 1999.
- [21] R. da Silva, R. Raphe, H. Felício, M. Rocha, W. Duca, P. Arroyo, G. Palini, A. Vasquez, D. Miquelin, L. Reis, A. Silva, and R. da Silva, “Prevalence, treatment, and outcomes of the hepatic artery stenosis after liver transplantation,” *Transplantation Proceedings*, vol. 40, no. 3, pp. 805–807, 2008.
- [22] O. Amili, J. Golzarian, and F. Coletti, “In vitro study of particle transport in successively bifurcating vessels,” *Annals of Biomedical Engineering*, vol. 47, no. 11, p. 2271 – 2283, 2019.
- [23] J. Aramburu, R. Antón, N. Bernal, A. Rivas, J. C. Ramos, B. Sangro, and J. I. Bilbao, “Physiological outflow boundary conditions methodology for small arteries with multiple outlets: A patient-specific hepatic artery haemodynamics case study,” *Proceedings of the Institution of Mechanical Engineers, Part H: Journal of Engineering in Medicine*, vol. 229, no. 4, p. 291 – 306, 2015.
- [24] M. W. Reeks, “Transport, mixing and agglomeration of particles in turbulent flows,” *Flow, Turbulence and Combustion*, vol. 92, no. 1-2, p. 3 – 25, 2014.
- [25] W. Liu and C.-Y. Wu, “Analysis of inertial migration of neutrally buoyant particle suspensions in a planar poiseuille flow with a coupled lattice boltzmann method-discrete element method,” *Physics of Fluids*, vol. 31, no. 6, 2019.
- [26] J.-P. Matas, J. F. Morris, and Guazzelli, “Inertial migration of rigid spherical particles in poiseuille flow,” *Journal of Fluid Mechanics*, vol. 515, p. 171 – 195, 2004.

- [27] B. Khalili, M. Rahnama, S. Jafari, F. Gharibi, and E. J. Javaran, "Lattice boltzmann simulation of solid particles motion in a three dimensional flow using smoothed profile method," *Journal of Applied Fluid Mechanics*, vol. 10, no. 4, p. 1091 – 1103, 2017.
- [28] T. Snoeijink, T. Vlogman, J. Roosen, E. Groot Jebbink, K. Jain, and J. Nijsen, "Transarterial radioembolization: a systematic review on gaining control over the parameters that influence microsphere distribution," *Drug Delivery*, vol. 30, no. 1, 2023.
- [29] V. der Hoek, "Computational modelling of flow in the liver vasculature using the lattice boltzmann method to study microsphere distribution," *University of Twente*, 2021.
- [30] T. G. Vlogman and K. Jain, "Efficient coupled lattice boltzmann and discrete element method simulations of small particles in complex geometries (in revision)," *Computers and Mathematics with Applications*, vol. 00, no. 0, p. 0000000, 2024.
- [31] T. G. Vlogman, R. Hagmeijer, and K. Jain, "A systematic comparison of fully resolved and unresolved particulate flow simulations using the lattice boltzmann and discrete element methods (under review)," *Physical Review E*, vol. 00, no. 0, p. 0000000, 2024.
- [32] A.A.Mohammad, "Lattice boltzmann method: Fundamentals and engineering applications with computer codes, 2nd edition," p. 1 – 51, 2011.
- [33] A. Paussa and D. Esseni, "An exact solution of the linearized boltzmann transport equation and its application to mobility calculations in graphene bilayers," *Journal of Applied Physics*, vol. 113, no. 9, 2013.
- [34] G. M. Latyshev, A.V. Spitkovski I.M., "Analytical solution of the model boltzmann equation with the collision operator of compound type." *Oper. Theory:Adv. Appl.*, vol. 51, p(189-199), 1991.
- [35] P. L. Bhatnagar, E. P. Gross, and M. Krook, "A model for collision processes in gases. i. small amplitude processes in charged and neutral one-component systems," *Phys. Rev.*, vol. 94, pp. 511–525, May 1954.
- [36] C. Cercignani, "Are there more than five linearly-independent collision invariants for the boltzmann equation?" *Journal of Statistical Physics*, vol. 58, no. 5-6, p. 817 – 823, 1990.
- [37] M. D. Schuster, N. Memarsadeghi, and M. Schuster, "Lattice gas cellular automata fluid dynamics: The model of frisch, hasslacher, and pomeau," *Computing in Science and Engineering*, vol. 25, no. 2, p. 64 – 68, 2023.
- [38] M. Bauer, G. Silva, and U. Rude, "Truncation errors of the d3q19 lattice model for the lattice boltzmann method," *Journal of Computational Physics*, vol. 405, 2020.
- [39] X. He and L.-S. Luo, "Lattice boltzmann model for the incompressible navier-stokes equation," *Journal of Statistical Physics*, vol. 88, no. 3-4, p. 927 – 944, 1997.
- [40] Y. Bao and J. Meskas, "Lattice boltzmann method for fluid simulations," p. 2, 04 2014.
- [41] Z.-L. Guo, C.-G. Zheng, and B.-C. Shi, "Non-equilibrium extrapolation method for velocity and pressure boundary conditions in the lattice boltzmann method," *Chinese Physics (Overseas Edition)*, vol. 11, no. 4, p. 366 – 374, 2002.
- [42] Q. Zou and X. He, "On pressure and velocity boundary conditions for the lattice Boltzmann BGK model," *Physics of Fluids*, vol. 9, no. 6, pp. 1591–1598, 06 1997.

- [43] T. G. Cowling, “Sydney chapman, 1888-1970,” *Biogr. Mem. Fellows R. Soc.*, vol. 17, pp. 53–89, Nov. 1971.
- [44] D. Enskog, *Kinetische Theorie der Vorgänge in mässig verdünnten Gasen*. Almqvist & Wiksells boktryckeri-a.-b., 1917, no. v. 1.
- [45] J. Li, “Appendix: Chapman-enskog expansion in the lattice boltzmann method,” 12 2015.
- [46] D. d’Humières and I. Ginzburg, “Viscosity independent numerical errors for lattice boltzmann models: From recurrence equations to “magic” collision numbers,” *Computers Mathematics with Applications*, vol. 58, no. 5, pp. 823–840, 2009, mesoscopic Methods in Engineering and Science.
- [47] P. Lallemand and L.-S. Luo, “Theory of the lattice boltzmann method: Dispersion, dissipation, isotropy, galilean invariance, and stability,” *Physical review. E, Statistical physics, plasmas, fluids, and related interdisciplinary topics*, vol. 61, pp. 6546–62, 07 2000.
- [48] P. Gondret, M. Lance, and L. Petit, “Bouncing motion of spherical particles in fluids,” *Physics of Fluids*, vol. 14, no. 2, p. 643 – 652, 2002.
- [49] K. Jain, “Transition to turbulence in an oscillatory flow through stenosis,” *Biomechanics and Modeling in Mechanobiology*, vol. 19, no. 1, p. 113 – 131, 2020.
- [50] S. S. Varghese, S. H. Frankel, and P. F. Fischer, “Direct numerical simulation of stenotic flows. part 1. steady flow,” *Journal of Fluid Mechanics*, vol. 582, p. 253 – 280, 2007.
- [51] L. Rosenhead, *Laminar Boundary Layers: An Account of the Development, Structure, and Stability of Laminar Boundary Layers in Incompressible Fluids, Together with a Description of the Associated Experimental Techniques*, ser. Fluid motion memoirs. Clarendon Press, 1963.
- [52] P. Hendriks, D. Rietbergen, A. van Erkel, M. Coenraad, M. Arntz, R. Bennink, A. Braat, S. Crobach, O. Delden, P. Dibbets-Schneider, T. Hulle, H. J. Klumpen, R. Meer, J. Nijsen, C. Rijswijk, J. Roosen, B. Ruijter, F. Smit, M. Stam, and M. Burgmans, “Adjuvant holmium-166 radioembolization after radiofrequency ablation in early-stage hepatocellular carcinoma patients: a dose-finding study (hora est hcc trial),” *European Journal of Nuclear Medicine and Molecular Imaging*, vol. 51, pp. 1–13, 02 2024.
- [53] H. K. Versteeg and W. Malalasekera, *An introduction to computational fluid dynamics - the finite volume method*. Addison-Wesley-Longman, 1995.
- [54] P. Baj, P. J. K. Bruce, and O. R. H. Buxton, “The triple decomposition of a fluctuating velocity field in a multiscale flow,” *Physics of Fluids*, vol. 27, no. 7, p. 075104, 07 2015.
- [55] P. Welch, “The use of fast fourier transform for the estimation of power spectra: A method based on time averaging over short, modified periodograms,” *IEEE Transactions on Audio and Electroacoustics*, vol. 15, no. 2, pp. 70–73, 1967.